TECHNISCHE UNIVERSITÄT MÜNCHEN

Fakultät für Elektrotechnik und Informationstechnik
Lehrstuhl für Biologische Bildgebung

Real-time intra-operative and endoscopic molecular fluorescence imaging

Jürgen Glatz

Vollständiger Abdruck der von der Fakultät für Elektrotechnik und Informationstechnik der Technischen Universität München zur Erlangung des akademischen Grades eines

Doktor-Ingenieurs

genehmigten Dissertation.

Vorsitzender:	Univ.-Prof. Dr.-Ing. Werner Hemmert
Prüfer der Dissertation:	
	1. Univ.-Prof. Dr. Vasilis Ntziachristos
	2. Jun.-Prof. Dr. rer. nat. Martin Kleinsteuber
	3. apl. Prof. Dr. rer. nat. Sibylle Ziegler

Die Dissertation wurde am 03.11.2014 bei der Technischen Universität München eingereicht und durch die Fakultät für Elektrotechnik und Informationstechnik am 07.05.2015 angenommen.

Real-time intra-operative and endoscopic molecular fluorescence imaging

Jürgen Glatz

Department of Electrical Engineering and Information Technology

Technische Universität München

A thesis submitted for the degree of

Doktor Ingenieur

October 27, 2014

Abstract

The discrimination of healthy tissue from malignant tumors remains a challenging issue in medicine, with implications for both diagnosis and treatment. Optical imaging has been identified as a promising modality that can be used in surgical and endoscopic settings to supplement the visual evaluation by the physician. Beside their low cost and easy integration, optical methods can be based on a variety of intrinsic and extrinsic contrast mechanisms. One of the most powerful approaches is the administration of targeted fluorescent agents, which selectively bind to specific molecules or cellular structures. Such contrast agents allow for molecular imaging, which can identify malignant alterations on a cellular level, before they are perceptible by the human eye and with higher sensitivity and specificity.

In this thesis, molecular fluorescence imaging in the near-infrared (NIR) spectral range was translated from pre-clinical animal experiments to patient studies in open surgery and endoscopy. An intra-operative imaging system was designed and constructed to enable concurrent acquisition of color and fluorescence images and their processing at video-rates in order to display a composite image to the physician. The system was then adapted for the use in endoscopy and laparoscopy, enabling fluorescence imaging in colonoscopy and gastroenterology. Furthermore, novel algorithms were developed and evaluated to correct diffusion effects on fluorescence imaging and obtain the tissue's wavelength-independent optical properties from an optimized set of narrow wavebands. Finally, a new contrast agent was devised, combining a monoclonal antibody, which specifically targets a tumor marker, with a NIR fluorescent dye. This agent was tested and validated in mouse experiments and eventually employed in clinical feasibility studies. During breast cancer surgery, intra-operative imaging of the targeted agent enabled surgical guidance and ensured complete resection by visualizing leftover margins to the surgeon. In surveillance colonoscopy, the adapted system was used

to provide a red-flag detection strategy, wherein suspicious areas were highlighted, helping the endoscopist in finding even small tumor foci and sub-surface lesions. Thus, optical fluorescence imaging, based on a custom designed system and a targeted agent, was successfully translated to initial clinical applications, promising improved medical outcomes in the future.

Contents

Chapter 1

Introduction

1.1 Intra-operative imaging

Cancer is one of the most significant health problems of our days, accounting for 25 % of deaths in the United States [1] and affecting a total of 14.1 million people worldwide [2]. The most prevalent therapy approaches are cytotoxic chemotherapy [3, 4], hormone therapy [5], radiotherapy [6], molecularly targeted therapy [7] and surgical resection [8].
Surgical intervention plays an important role and is often the treatment of choice, for example in breast cancer, which remains the second leading cause of death im women [2]. The adoption of frequent and widespread mammography screening in the past decades has resulted in diagnosis at an earlier stage, where surgical treatment is regarded as the most promising option. Two distinct approaches have been established: mastectomy, i.e. the complete removal of one or both breasts, and breast-conserving therapy, wherein a partial lumpectomy is combined with radiotherapy [9]. The latter is associated with several advantages for the patient, notably reduced infection risk and more appealing cosmetic results [10], with survival rates not inferior to those of complete mastectomy [11].
Indeed the most crucial factor for the surgical outcome is the completeness of the resection, which is ensured by removing the tumor along with a rim of healthy tissue, and testing the borders of the excised specimen for remaining tumor cells. Studies have shown that such positive margins are indicative of an increased risk for local tumor recurrence [12, 13], which deteriorates the prognosis and requires additional treatment. Positive margin rates of 20–40 % have been reported [14, 15], a fact that clearly indicates the clinical need for optimized

surgical procedures.
The existing limitations arise from the challenge of identifying and demarcating malignant alterations with effectual sensitivity and specificity. The only means available to the surgeon are the visual assessment of tissue discolorations and tactile sample evaluation, which are sufficient to identify progressed disease but problematic with respect to early-stage cancer, small focuses of tumor and sub-surface clusters. This dilemma is specific to the intra-operative scenario, given that powerful imaging modalities such as positron emission tomography (PET), magnetic resonance imaging (MRI) or X-ray computed tomography (CT), among others, in conjunction with radiological tracers, are available for the pre-operative diagnosis, staging and planning. The same methods can be used for post-operative evaluation, supplemented by pathological analysis of the excised tissue, using e.g. histological staining such as hematoxylin and eosin (H&E) or molecular imaging by immunohistochemistry (IHC).
In contrast, the methods available for intra-operative examination are less multitudinous. One standard procedure is wire-guided localization, the insertion of a wire under ultrasound or X-ray guidance into the tumor mass before the surgery [16]. Molecular assessment can be realized by frozen section analysis, where microscopic imaging of excised tissue is performed during or immediately after the intervention [17]. In addition, intra-operative imaging based on low-field MRI or X-ray imaging using C-arms employs bulky and expensive devices, with added disadvantages such as working with magnetic field compatible equipment or exposure to ionizing radiation. Altogether, the need for intra-operative imaging devices that can help to achieve improved surgical results by providing accurate tumor localization has not yet been met [14, 18].

1.2 Optical imaging in endoscopy[1]

A similar clincal need for improved optical imaging exists also in endoscopy. Colorectal cancer (CRC) remains the second leading cause of cancer-related deaths in the western world and is one of the most prevalent cancer types both in men and women [20]. Surveillance colonoscopy is the current standard for the prevention and relapse screening of CRC, however it relies on macroscopic features such as color or texture fluctuations observed under illumination with white light, which makes the detection of small precursor lesions particularly

[1] This discussion was published in Ref. [19]

difficult. Consequently, the key aspects of early lesion detection and the identification of the tumor characteristics to determine the optimal treatment for the individual patients remain unmet. Molecular characterization of the detected lesions, the basis for the selection of new targeted treatments in oncology [21], is performed using tissue biopsies, which however cannot reveal the heterogeneity of the lesions and lymph node metastases [22, 23]. Contrasting the wide clinical acceptance of white-light colonoscopy, its lack of sensitivity to sub-surface activity and its incapability to elucidate particular physiological and molecular disease features of the detected premalignant lesions result in substantial lesion miss-rates that can be as high as 55% in patients with an inherited predisposition to colon cancer, such as Lynch syndrome [24].

Given this inadequate diagnostic yield, high-resolution endoscopy and filter-based systems have arisen and are commercially available from several manufacturers. These advanced endoscopic methods encompass chromoendoscopy [25], narrow band imaging (NBI) [26], and autofluorescence imaging (AFI) [27]. Chromoendoscopy consists in the topical application of stains or dyes on the colonic mucosa to highlight micro-anatomical changes that would be imperceptible under white-light illumination. Yet its widespread use has been prevented by limitations such as elevated time consumption, the lack of standardized classification systems and reproducibility [28]. NBI highlights hemoglobin absorption by restricting illumination to the blue and green areas of the spectrum, thus making diseased tissue appear darker than surrounding healthy mucosa. AFI detects endogenous fluorescent substances such as NADH, FAD and porphyrins [28], without the administration of exogenous fluorescent agents. Both NBI and AFI have proven reasonable sensitivity in the delineation of adenomas from surrounding non-dysplastic tissue, therefore assisting in lesion removal, but have not improved adenoma detection [29]. Although further studies are still required to validate their utility as stand-alone diagnostic methodologies [26], they can be valuable tools when used as part of a multimodal imaging scheme [28]. However, all three methods exploit the optical contrast intrinsic to the tissue and do not confront the lack of information about the expression of recognized disease biomarkers, which is of paramount importance to guide lesion differentiation and targeted treatment selection.

Consequently, there is still an unmet clinical need for an endoscopic imaging modality that can highlight flat precursor lesions, visualize below the surface, and give insight into the biological characteristics of the CRC lesions. Wide field targeted imaging with near-infrared (NIR) fluorescence [30] appears to be a promising approach for a number of reasons. Firstly,

wide-field imaging is preferable to virtual or optical biopsy, as achieved for example by confocal endomicroscopy [31], which still relies first on white-light colonoscopy for the identification of suspicious areas and it is not suited for screening large surfaces [28]. Therefore, the real clinical need, which lies in the identification at first sight and over a large area of the bowel wall of those tissue locations that require a closer look, is not solved. Secondly, the employment of NIR fluorescent agents with targeting specificity to cancer moieties simultaneously allows for the visualization of specific tissue biomarkers.

Technological challenges mainly arise from the fact that current medical endoscopes are predominantly videoscopes, which utilize a small charge-coupled device (CCD) chip embedded at the distal tip of the scope that has insufficient sensitivity for acquiring NIR fluorescence images in real-time, especially at increased depth, small adenomas and low concentrations. Liu et al. have proposed an in vivo fluorescence imaging system based on a paediatric urethroscope to confront this issue [32]. Although it provides outstanding imaging resolution and satisfies real-time constraints, it would be more appropriate for percutaneous or intraoperative use since rigid rod lenses cannot be incorporated with the flexible endoscopes that are routinely used in gastrointestinal endoscopy. Accordingly, flexible alternatives have also been suggested. Commercial autofluorescence endoscopes incorporate two separate CCDs at their tip, and a filter that only enables tissue autofluorescence in the 500-630 nm range is placed in front of the CCD that acquires the fluorescence signal. Sequential color and autofluorescence imaging is achieved by alternating white and blue light via a rotating filter in front of the light source [27]. Similarly, the modular video endoscope reported in [33] provides white-light, cross-polarized and fluorescence imaging capabilities via an endoscope cap allocating interchangeable filter modules. Because of the minimal tissue autofluorescence in the NIR and the small quantities of the exogenous contrast agents that are administered to ease the pathway towards clinical translation, this design cannot be redefined for operating in this higher waveband in a straight forward manner. Within the same framework, a scanning approach has been implemented by Lee et al. [34, 35]. It exhibits an ultra-compact coaxial-design with an outer diameter of 1.6 mm, which allows it to be guided through the working channel of routine endoscopes [34]. A single optical fiber is vibrated laterally using a custom tubular piezoelectric actuator to scan the image plane in an outwardly growing spiral pattern at frame rates of 30 and 15 Hz for 500 or 1000 line images, respectively. Additionally, both confocal and non-confocal collection methods are supported [34]. In the non-confocal geometry the backscattered light is collected by a ring of high numerical aperture (NA) multimode fibers that surround the

fiber scanner, whose location, size and number determine the collection efficiency. The latest development of this scanning endoscope incorporates 12 step-index plastic optical fibers with a NA of 0.63 and outer diameter of 250 μm [35], yet the reported sensitivity was insufficient to image fluorophore concentrations below 1 μM.

1.3 Optical contrast mechanisms

Optical imaging has emerged as a promising modality to address the aforementioned challenges in both surgical and endoscopic imaging [18, 36]. It offers several notable advantages, that make it an ideal solution for the use in medical interventions. Firstly, the required hardware typically comprises just cameras and some other optical components, making the whole imaging system cheap, transportable and easy to integrate without impeding the clinical workflow. Secondly, optical imaging directly relates to the physician's vision, which makes it an intuitive addition that can offer feedback in real-time. Finally, optical imaging is based on a variety of contrast mechanisms, either intrinsic and externally administrated, enabling its application to a wide range of clinical tasks.

1.3.1 Endogenous contrast

The intrinsic optical features of biological samples are commonly evaluated in all medical disciplines, when physicians visually examine their patients. The contrast stems from the differences in the interaction of tissue compounds with light, which mainly comprises two distinct physical events, namely absorption and scattering [37]. Both of them are wavelength dependent, meaning they will occur with a characteristic frequency in different regions of the light spectrum.

Hemoglobin, the protein in the red blood cells that transports oxygen, has the notable property of changing its absorption spectrum when saturated with oxygen molecules. This contrast can even be registered with the bare eyes, it is a main reason for veins appearing blue [38] and also indicates hypoxia by the bluish discoloration known as cyanosis [39]. The pulse oximeter, a device to determine the precise blood oxygen level by measuring the absorption of hemoglobin, has been developed as early as 1935 [40, 41] and is still used today. Recently, more intricate systems have been developed, realizing for instance laparoscopic multispectral imaging to measure the renal oxygenation during nephrectomy [42]. Chromophores such as melanin

are other potential sources of absorption contrast and can be utilized for the identification of melanoma [43].
Variances in the scattering properties also encode valuable information, that can be measured by fiber optical probes [44]. Wilke et al. proposed an imaging box for the assessment of surgically excised tissue specimen that utilizes a classification scheme based on the optical properties to test for positive margins, reporting a sensitivity of 79 % and a specificity of 67 % [45]. However, a major limitation arose from their fiber-based setup, which required close proximity to the sample and thus could only be used outside the sterile field. An interesting improvement is spatial frequency domain imaging (SFDI), whereby the tissue is illuminated by spatially modulated patterns of different frequencies to map the optical properties [46]. In a pilot study, SFDI was used to measure oxygenation [47], thus showcasing non-contact intra-operative probing of tissue optical properties, which makes SFDI the most promising approach to employ endogenous contrast in future clinical applications.

1.3.2 Autofluorescence

Autofluorescence imaging (AFI) can be regarded as a special case of the endogenous contrast mechanisms described above and has been proposed as a method for tissue diagnosis already in 1924 [48]. Thereby not the chromophore absorption is of interest, but instead the subsequent re-emission of higher wavelength photons is measured. Various autofluorescent tissue components, e.g. nicotinamide adenine dinucleotide (NADH), collagen and lipopigments, along with their characteristic absorption and emission spectra have been identified [49]. An important advantage of AFI is that it enables non-contact imging of a wide field of view, without requiring the administration of potentially harmful contrast agents.
Lee et al. studied variances in autofluorescence levels as an indicator of dysplasia and malignancy in lung biopsies [50], reporting 85 % sensitivity and 80 % specificity, while von Breitenbuch et al. demonstrated the feasibility of AFI in imaging peritoneal carcinosis [51]. Autofluorescence contrast can also be used in minimally invasive procedures such as laparoscopy for the detection of endometriosis [52] and in endoscopy [53]. Therein, it has been employed as part of a multimodal imaging approach [27] and for surveillance endoscopy [54]. However, van den Broek et al. reported, that adenoma miss rates could not be significantly reduced [55].

Nevertheless, autofluorescence can offer higher specificity than endogenous contrast, because therein many tissue chromophores contribute to absorption and scattering, and both parameters vary over wavelength, which makes the quantification of exact contributions difficult. In contrast, the autofluorescence emission of a chromophore, when measured in a narrow spectral band, seems to be more characteristic, and thus a reliable way to detect the presence or absence of the respective source. However, a remaining limitation is that the autofluorescent components themselves are often not very strong indicators of malignancy. Various benign alterations, as well as metabolic changes and fluorochrome bleaching can effect the detected signal and compromise specificity of disease identification.

1.3.3 Contrast agents

A logical attempt to improve upon the intrinsic contrast and autofluorescence emission of biological tissue is the administration of exogenous fluorescent contrast agents. The green-fluorescent organic dye fluorescein [56] and its derivate fluorescein isothiocyanate (FITC) have long been used in various clinical applications. These compounds act as blood pool agents, that can highlight the vasculature and accumulate in tumors due to their increased vessel permeability [57]. Since its approval by the United States food and drug administration (FDA) in 1976 fluorescein has been employed, among others, for thoratoscopy [58], glioma surgery [59, 60] and margin detection of paget disease [61].
A similar clinically approved drug is indocyanine green (ICG), which, in contrast to fluorescein, fluoreces in the near-infrared (NIR) spectral region around 800 nm. This longer wavelength comes with three important advantages. Hemoglobin is the main absorbing component in tissue, but its absorption coefficient in the NIR is significantly lower than in the visible (400–700 nm), consequently allowing for a higher penetration depth and signal intensity. Furthermore, the excitation and emission wavelengths of ICG are distinct from the visible spectrum and their filtering does not interfere with the regular color vision, that is still required by physicians for orientation. Lastly, autofluorescence levels are reduced in the NIR range, producing less parasitic signal and thus an increased target-to-background ratio. The described advantages effectuated the use of ICG in a wide range of clinical fields. Like fluorescein, it has been used in angiography [62] and as a blood flow marker [63]. Applications in oncology comprise the injection of ICG for sentinel lymph node mapping during surgery of breast cancer [64, 65],

lung cancer [66] or melanoma [67], among others. Following up on the success in lymph node localization, ICG has also been employed for tumor imaging [68]. Ishizawa et al. showcased the visualization of hepatocellular carcinomas in the liver [69], while others have reported the detection of colorectal liver metastases [70] and tumors of the central nervous system [71, 72].

Another agent that is already applied clinically is 5-aminolevulinic acid (5–ALA), an intermediate in the hemoglobin synthesis, that, when administered topically or orally, induces the synthesis of protoporphyrin IX (PPIX), which is fluorescent around 700 nm. While PPIX is not ligand-specific, it was shown to accumulate selectively in neoplastic and malignant tissues due to their decreased ferrochelatase activity and possibly other factors [73]. Consequently, 5–ALA was studied for the visualization of e.g. colorectal cancer [74], bladder cancer [75] and lung cancer [76]. Yet its most successful application so far was a randomized multi-center trial that found a significantly improved progression free survival rate after glioma resection under PPIX fluorescence guidance, heralding its widespread use in brain surgery [77].

The most crucial property of an externally administered contrast agent is its specificity to the malignancy of interest. Consequently, research interest has focused on agents with molecular specificity that are able to highlight tumor based on its altered metabolism and marker expression, a known hallmark of cancer [78]. Pre-clinical research has intensively investigated molecular tracers [30, 79], showcasing that they can detect a broad range of targets with high sensitivity, specificity and reproducibility. However, the clinical translations of molecular fluorescence is progressing slowly and no targeted molecule has so far been approved by the regulatory authorities. The available feasibility studies are encouraging, though. In 1992, Folli et al. labeled an anti-tumor-associated antigen antibody with fluorescein and measured elevated fluorescence signals both in resected biopsy samples and intra-operatively in colorectal cancer patients [80]. Recently, folate-conjugated fluorescein was used by van Dam et. al in ten ovarian cancer patients to target folate receptor-α [81], which was previously identified as a potential target in epithelial ovarian carcinomas [82]. Significantly more lesions could be detected under fluorescence guidance, however broader clinical studies and regulatory approval are still outstanding.

The lack of clinically approved contrast agents with molecular specificity can be explained by translational hurdles. Before receiving regulatory approval, a long series of studies, beginning with pre-clinical toxicity tests in animals and ending with a large phase III clinical trial need to be carried out, where the required time and costs increase significantly after each step.

Consequently, alternative paths were explored, which could lead to a more rapid translation of new optical agents, while at the same time reducing the translational risk [83, 84]. The proposed approach is based on disease-specific drugs that have already passed the regulatory process and are approved by the authorities for clinical use. One such drug is bevacizumab (Avastin®, Hoffmann-La Roche, Basel, Switzerland), a humanized monoclonal antibody that targets vascular endothelial growth factor (VEGF), a factor that is overexpressed in many tumors. The antibody is then combined with the NIR fluorescent dye IRDye 800CW (LI-COR Biosciences, Lincoln, US-NE), that has been confirmed as non-toxic in prior experiments [85]. The resulting contrast agent can be applied clinically in very low doses, so called microdoses, that lie below 1 % of the drug's pharmacologically active dose. Given the promise to establish new optical agents with low associated risk and hurdles, the outlined approach was pursued in this thesis.

1.4 Quantitative imaging challenges

As with all imaging methods, optical fluorescence and reflection images faces various challenges originating from the physics of their contrast mechanisms. The phenomena discussed herein concern the signal quantification in both color and fluorescence imaging, aiming to produce accurate measurements of physiological parameters.

1.4.1 Diffusion in fluorescence imaging

Optical images, whether they are acquired in trans-illumination or epi-illumination geometry, are strongly affected by light-tissue interaction. The mean free path (MFP) is defined as the average distance a photon propagates within a sample before being absorbed or scattered. In turbid media, and specifically in the NIR spectral region, light scattering is the dominant process and thus severely limits the optical penetration depth and decreases the attainable resolution [86]. Conventional microscopy typically uses slices thinner than 20 μm, well below the average MFP in biological tissue [87], to minimize scattering effects and obtain sharp images. The degradation of images from deep tissue represents a crucial limitation to the in vivo study of biological processes.

Consequently, significant attention has been directed towards quantifying the true fluorescence concentration by correcting for the influence of optical properties on the measured

intensity. Various ratiometric methods that normalize the fluorescence emission by multispectral reflectance measurements have been proposed [88–90]. Such reflection-based approaches were shown to be beneficial for correcting differences in irradiance and absorption, however, a crucial limitation of ratiometric methods is that they are performed on a pixel-by-pixel basis, i.e. they do not model the interaction of neighboring regions and typically are applied and evaluated on homogeneous phantoms. Furthermore, ratiometric approaches are deteriorated by the presence of scattering inhomogeneities [91] and theoretical models of light propagation suggest that reflectance measurements alone are insufficient to resolve the optical parameters of tissue [92].

By contrast, the possibility to use additional measurements was investigated. Examples include polarization images to select only photons that are affected by scattering or absorption [93], structured illumination projection / SFDI as a means to estimate the optical properties [94] and schemes to focus light through scattering media [95, 96]. Bertolotti et al. [97] published a method for the imaging of a fluorescent object under a scattering layer, where the laser beam's angle of incidence is measured and an iterative algorithm based on speckle correlations is used to reconstruct the hidden object. However, their approach assumes a scattering layer that is both homogeneous and isotropic, utilizes a collimated laser beam that produces a limited excitation area and requires additional instrumentation to measure the beam angle, all of which represent a challenge for the translation to in vivo clinical practice. Furthermore, schemes based on wavefront shaping are challenging to perform in real-time for inhomogeneous samples.

The influence of tissue optical properties on the fluorescence signal affects not only the detected intensity, hindering fluorophor quantification by introducing a dependence on both absorption and scattering, but it also alters the detected shape. Scattered light loses directionality, which not only limits resolution and penetration depths but also introduces distortions in the observed spatial fluorophore distribution [86, 98]. This effect is of particular importance for the accurate delineation of tumor margins in surgical imaging and is commonly not addressed by correction algorithms that operate on a pixel per pixel basis. Instead, a novel approach based on two-dimensional modeling of scattering effects is presented in this thesis.

1.4.2 Optimization of multispectral wavebands

As discussed in Section 1.3.1, tissue discolorations are an important source of physiological information and a commonly used tool for the diagnosis and localization of various medical conditions. However, the human eye is limited in both the light wavelength range it can perceive and the spectral resolution. Consequently, spectral imaging techniques and spectroscopy have been introduced in biomedical applications to extract more detailed information on the sample composition from subtle wavelength reflection alterations [99]. Distinct spectral signatures can be used to identify differences in the objects biochemical composition, and thus alterations in tissue optical properties have been identified as a potential early indicator for malignant tissue alterations. Clinical applications have been found in melanoma diagnosis [100], burn wound assessment [101] and retinal imaging [102].
Spectral imaging methods can be classified by their wavelength resolution into multispectral, hyperspectral and even ultraspectral imaging. However, the measurement at many narrow bands typically requires either expensive and bulky hardware or a prolonged acquisition time. Multispectral solutions, preferably with the capability to image in real-time and thus provide immediate feedback, have been favored for clinical applications [103]. A promising approach to limit the acquisition complexity while, at the same time, enhancing the specificity for certain features of interest is the optimization of the measured spectral regions. One such example is NBI endoscopy, which aims to improve the diagnostic yield of surveillance endoscopy by measuring distinct blue and green spectral bands, that improve the visualization of blood vessels [26]. Similarly, optimized wavelength ranges have been suggested for chromophore detection in spatial frequency domain imaging [104], blood oximetry in the retina [102] and malignancy detection in the uterine cervix [105]. However, a generalized methodology to determine optimal wavelengths for the measurement of tissue properties has not yet been determined.

1.5 Aims and scope of this thesis

This work pursues three major goals in an attempt to bring intra-operative NIR molecular imaging into the clinics. The first of these was the development of an intra-operative imaging system that can measure and process the targeted fluorescence in real time during clinical interventions. Importantly, the system needed to be applicable with minimal adaptations to

both open surgery and endoscopy, meeting the necessary requirements regarding safety, sterility, ease of use and transportability. The developed imaging platform is presented in Chapter 2, with Section 2.1 describing the intra-operative setup as well as the associated software interface and image processing steps, while Section 2.1 details the system adaptation for the use in laparoscopy and endoscopy.

The second goal, the development of processing algorithms and implementations that resolve some of the challenges of quantitative intra-operative fluorescence imaging, is covered in Chapter 3. Firstly, the real-time constraint imposed by the necessity for immediate feedback during medical interventions is addressed by a graphics processing unit (GPU) based parallel computing architecture for the imaging system software as presented in Section 3.1. Subsequently, a novel correction approach for the influence of diffusion on fluorescence images is developed and evaluated in Section 3.2. Finally, the Chapter concludes with the optimization of the spectral bands for the determination of tissue properties using an analytical model of reflectance image formation in Section 3.3.

The final and most significant goal was the clinical translation of the imaging system, in conjunction with a targeted molecular agent, to the intra-operative imaging of patients in surgery and endoscopy in Chapter 4. Initially, pre-clinical validation of the involved components was carried out, commencing with the experiments presented in Section 4.1.1. Therein, the imaging system was employed for the laparoscopic imaging of induced colorectal cancer in mice, showcasing that real-time molecular detection of CRC is feasible. Utilizing a similar disease model, Section 4.1.2 took the development one step further, firstly by investigating the fiber and fiberscope based setups for endoscopic screening and secondly by utilizing the agent bevacizumab-800CW. As outlined in Section 1.3.3, such drug-based compounds currently are among the most promising agents for rapid clinical translation of molecular imaging.

Given the encouraging pre-clinical results, patient studies were undertaken. Section 4.2.1 presents a feasibility study of fluorescence-guided gastroenterology using a NIR blood pool agent. Together with clinical collaborators, two ongoing studies of the bevacizumab-800CW agent for molecular cancer imaging were launched. The first study is discussed in Section 4.2.2 and concerns intra-operative imaging during breast cancer surgery for improved margin detection and contrast agent validation. The second one aims to realize fluorescence endoscopy for the identification of colorectal cancer and is presented in Section 4.2.3.

Finally, the obtained results are summarized in Chapter 5 and possibilities for future work are outlined.

Bibliography

[1] R. Siegel, J. Ma, Z. Zou, and A. Jemal, "Cancer statistics 2014", *CA: A Cancer Journal for Clinicians*, vol. 64, no. 1, pp. 9–29, 2014.

[2] International Agency for Research on Cancer, *GLOBOCAN 2012: estimated cancer incidence, mortality and prevalence worldwide in 2012*, 2012.

[3] B. A. Chabner and T. G. Roberts, "Chemotherapy and the war on cancer", *Nature Reviews Cancer*, vol. 5, no. 1, pp. 65–72, 2005.

[4] R. Airley, *Cancer chemotherapy: basic science to the clinic*. Hoboken, US-NJ: Wiley-Blackwell, 2009.

[5] S. Hellman, S. A. Rosenberg, and V. T. DeVita, Eds., *Cancer: principles & practice of oncology*. Philadelphia, US-PA: Lippincott Williams & Wilkins, 2005.

[6] P. Mayles, A. Nahum, and J.-C. Rosenwald, *Handbook of radiotherapy physics: theory and practice*. Boca Raton, US-FL: CRC Press, 2007.

[7] M. R. Green, "Targeting targeted therapy", *New England Journal of Medicine*, vol. 350, no. 21, pp. 2191–2193, 2004.

[8] M. Chaudry and M. Winslet, *Surgical Oncology*, ser. Oshsurg Series. Oxford, UK: Oxford University Press, 2009.

[9] G. F. Schwartz, U. Veronesi, K. B. Clough, J. M. Dixon, I. S. Fentiman, S. H. Heywang-Köbrunner, R. Holland, K. S. Hughes, R. Margolese, I. A. Olivotto, J. P. Palazzo, and L. J. Solin, "Consensus conference on breast conservation", in *Seminars in Breast Disease*, WB Saunders, vol. 10, 2007, pp. 178–185.

[10] L. Jacobs, "Positive margins: the challenge continues for breast surgeons", *Annals of Surgical Oncology*, vol. 15, no. 5, pp. 1271–1272, 2008.

[11] B. Fisher, S. Anderson, J. Bryant, R. G. Margolese, M. Deutsch, E. R. Fisher, J.-H. Jeong, and N. Wolmark, "Twenty-year follow-up of a randomized trial comparing total mastectomy, lumpectomy, and lumpectomy plus irradiation for the treatment of invasive breast cancer", *New England Journal of Medicine*, vol. 347, no. 16, pp. 1233–1241, 2002.

[12] B. Kreike, A. A. Hart, T. van De Velde, J. Borger, H. Peterse, E. Rutgers, H. Bartelink, and M. J. van De Vijver, "Continuing risk of ipsilateral breast relapse after breast-conserving therapy at long-term follow-up", *International Journal of Radiation Oncology Biology Physics*, vol. 71, no. 4, pp. 1014–1021, 2008.

[13] A. Mannell, "Breast-conserving therapy in breast cancer patients-a 12-year experience", *South African Journal of Surgery*, vol. 43, no. 2, pp. 28–32, 2005.

[14] R. G. Pleijhuis, M. Graafland, J. de Vries, J. Bart, J. S. de Jong, and G. M. van Dam, "Obtaining adequate surgical margins in breast-conserving therapy for patients with early-stage breast cancer: current modalities and future directions", *Annals of Surgical Oncology*, vol. 16, no. 10, pp. 2717–2730, 2009.

[15] C. C. Park, M. Mitsumori, A. Nixon, A. Recht, J. Connolly, R. Gelman, B. Silver, S. Hetelekidis, A. Abner, J. R. Harris, *et al.*, "Outcome at 8 years after breast-conserving surgery and radiation therapy for invasive breast cancer: influence of margin status and systemic therapy on local recurrence", *Journal of Clinical Oncology*, vol. 18, no. 8, pp. 1668–1675, 2000.

[16] L. Liberman, J. Kaplan, K. J. Van Zee, E. A. Morris, L. R. LaTrenta, A. F. Abramson, and D. D. Dershaw, "Bracketing wires for preoperative breast needle localization", *American Journal of Roentgenology*, vol. 177, no. 3, pp. 565–572, 2001.

[17] S. Weber, F. Storm, J. Stitt, and D. M. Mahvi, "The role of frozen section analysis of margins during breast conservation surgery.", *The Cancer Journal from Scientific American*, vol. 3, no. 5, pp. 273–277, 1996.

[18] P. B. Garcia-Allende, J. Glatz, M. Koch, and V. Ntziachristos, "Enriching the interventional vision of cancer with fluorescence and optoacoustic imaging", *Journal of Nuclear Medicine*, vol. 54, no. 5, pp. 664–667, 2013.

[19] P. B. Garcia-Allende, J. Glatz, M. Koch, J. J. Tjalma, E. Hartmans, A. G. Terwisscha van Scheltinga, P. Symvoulidis, G. M. van Dam, W. B. Nagengast, and V. Ntziachristos, "Towards clinically translatable nir fluorescence molecular guidance for colonoscopy", *Biomedical Optics Express*, vol. 5, no. 1, pp. 78–92, 2014.

[20] L. Herszényi and Z. Tulassay, "Epidemiology of gastrointestinal and liver tumors", *European Review for Medical and Pharmacological Sciences*, vol. 14, pp. 249–258, 2010.

[21] S. Misale, R. Yaeger, S. Hobor, E. Scala, M. Janakiraman, D. Liska, E. Valtorta, R. Schiavo, M. Buscarino, G. Siravegna, *et al.*, "Emergence of kras mutations and acquired resistance to anti-egfr therapy in colorectal cancer", *Nature*, vol. 486, no. 7404, pp. 532–536, 2012.

[22] T. E. Goranova, M. Ohue, Y. Shimoharu, and K. Kato, "Dynamics of cancer cell subpopulations in primary and metastatic colorectal tumors", *Clinical & Experimental Metastasis*, vol. 28, no. 5, pp. 427–435, 2011.

[23] S. E. Baldus, K.-L. Schaefer, R. Engers, D. Hartleb, N. H. Stoecklein, and H. E. Gabbert, "Prevalence and heterogeneity of kras, braf, and pik3ca mutations in primary colorectal adenocarcinomas and their corresponding metastases", *Clinical Cancer Research*, vol. 16, no. 3, pp. 790–799, 2010.

[24] E. M. Stoffel, D. K. Turgeon, D. H. Stockwell, L. Zhao, D. P. Normolle, M. K. Tuck, R. S. Bresalier, N. E. Marcon, J. A. Baron, M. T. Ruffin, *et al.*, "Missed adenomas during colonoscopic surveillance in individuals with lynch syndrome (hereditary nonpolyposis colorectal cancer)", *Cancer Prevention Research*, vol. 1, no. 6, pp. 470–475, 2008.

[25] L. M. Wong Kee Song, D. G. Adler, B. Chand, J. D. Conway, J. Croffie, J. A. DiSario, D. S. Mishkin, R. J. Shah, L. Somogyi, W. M. Tierney, *et al.*, "Chromoendoscopy", *Gastrointestinal Endoscopy*, vol. 66, no. 4, pp. 639–649, 2007.

[26] L. M. Wong Kee Song, D. G. Adler, J. D. Conway, D. L. Diehl, F. A. Farraye, S. V. Kantsevoy, R. Kwon, P. Mamula, B. Rodriguez, R. J. Shah, *et al.*, "Narrow band imaging and multiband imaging", *Gastrointestinal Endoscopy*, vol. 67, no. 4, pp. 581–589, 2008.

[27] L. M. Wong Kee Song, S. Banerjee, D. Desilets, D. L. Diehl, F. A. Farraye, V. Kaul, S. R. Kethu, R. S. Kwon, P. Mamula, M. C. Pedrosa, *et al.*, "Autofluorescence imaging", *Gastrointestinal Endoscopy*, vol. 73, no. 4, pp. 647–650, 2011.

[28] R. Banerjee and D. N. Reddy, "Advances in endoscopic imaging: advantages and limitations", *Journal of Digestive Endoscopy*, vol. 3, no. 5, p. 7, 2012.

[29] T. Ahmed, J. Monti, and B. Lashner, "Random versus targeted biopsies for colorectal cancer surveillance in inflammatory bowel disease", *Gastroenterology & Hepatology*, vol. 6, no. 7, p. 438, 2010.

[30] S. A. Hilderbrand and R. Weissleder, "Near-infrared fluorescence: application to *in vivo* molecular imaging", *Current Opinion in Chemical Biology*, vol. 14, no. 1, pp. 71–79, 2010.

[31] P.-L. Hsiung, J. Hardy, S. Friedland, R. Soetikno, C. B. Du, A. P. Wu, P. Sahbaie, J. M. Crawford, A. W. Lowe, C. H. Contag, *et al.*, "Detection of colonic dysplasia *in vivo* using a targeted heptapeptide and confocal microendoscopy", *Nature Medicine*, vol. 14, no. 4, pp. 454–458, 2008.

[32] Z. Liu, S. J. Miller, B. P. Joshi, and T. D. Wang, "In vivo targeting of colonic dysplasia on fluorescence endoscopy with near-infrared octapeptide", *Gut*, 2012.

[33] N. Thekkek, M. C. Pierce, M. H. Lee, A. D. Polydorides, R. M. Flores, S. Anandasabapathy, and R. R. Richards-Kortum, "Modular video endoscopy for in vivo cross-polarized and vital-dye fluorescence imaging of barrett's-associated neoplasia", *Journal of Biomedical Optics*, vol. 18, no. 2, p. 026 007, 2013.

[34] C. M. Lee, C. J. Engelbrecht, T. D. Soper, F. Helmchen, and E. J. Seibel, "Scanning fiber endoscopy with highly flexible, 1 mm catheterscopes for wide-field, full-color imaging", *Journal of Biophotonics*, vol. 3, no. 5-6, pp. 385–407, 2010.

[35] S. J. Miller, C. M. Lee, B. P. Joshi, A. Gaustad, E. J. Seibel, and T. D. Wang, "Targeted detection of murine colonic dysplasia in vivo with flexible multispectral scanning fiber endoscopy", *Journal of Biomedical Optics*, vol. 17, no. 2, pp. 0 211 031–02 110 311, 2012.

[36] G. Lu and B. Fei, "Medical hyperspectral imaging: a review", *Journal of Biomedical Optics*, vol. 19, no. 1, pp. 010 901–010 901, 2014.

[37] M. S. Patterson, B. C. Wilson, and D. R. Wyman, "The propagation of optical radiation in tissue I. Models of radiation transport and their application", *Lasers in Medical Science*, vol. 6, no. 2, pp. 155–168, 1991.

[38] A. Kienle, L. Lilge, I. A. Vitkin, M. S. Patterson, B. C. Wilson, R. Hibst, and R. Steiner, "Why do veins appear blue? A new look at an old question", *Applied Optics*, vol. 35, no. 7, p. 1151, 1996.

[39] T. Ahrens, K. Rutherford, and K. A. R. Basham, *Essentials of oxygenation: implication for clinical practice*. Jones & Bartlett Learning, 1993.

[40] K. Matthes, "Untersuchungen über die sauerstoffsättigung des menschlichen arterienblutes", *Naunyn-Schmiedebergs Archiv für experimentelle Pathologie und Pharmakologie*, vol. 179, no. 6, pp. 698–711, 1935.

[41] G. A. Millikan, "The oximeter, an instrument for measuring continuously the oxygen saturation of arterial blood in man", *Review of Scientific Instruments*, vol. 13, no. 10, pp. 434–444, 2004.

[42] Z.-W. Liu, S. Faddegon, E. O. Olweny, S. L. Best, N. Jackson, G. V. Raj, K. J. Zuzak, and J. A. Cadeddu, "Renal oxygenation during partial nephrectomy: a comparison between artery-only occlusion versus artery and vein occlusion", *Journal of Endourology*, vol. 27, no. 4, pp. 470–474, 2013.

[43] B. Farina, C. Bartoli, A. Bono, A. Colombo, M. Lualdi, G. Tragni, and R. Marchesini, "Multispectral imaging approach in the diagnosis of cutaneous melanoma: potentiality and limits", *Physics in Medicine and Biology*, vol. 45, no. 5, p. 1243, 2000.

[44] F. van Leeuwen–van Zaane, U. A. Gamm, P. B. A. A. van Driel, T. J. A. Snoeks, H. S. de Bruijn, A. van der Ploeg–van den Heuvel, I. M. Mol, C. W. G. M. Löwik, H. J. C. M. Sterenborg, A. Amelink, *et al.*, "In vivo quantification of the scattering properties of tissue using multi-diameter single fiber reflectance spectroscopy", *Biomedical Optics Express*, vol. 4, no. 5, pp. 696–708, 2013.

[45] L. G. Wilke, J. Brown, T. M. Bydlon, S. A. Kennedy, L. M. Richards, M. K. Junker, J. Gallagher, W. T. Barry, J. Geradts, and N. Ramanujam, "Rapid noninvasive optical imaging of tissue composition in breast tumor margins", *The American Journal of Surgery*, vol. 198, no. 4, pp. 566–574, 2009.

[46] D. J. Cuccia, F. Bevilacqua, A. J. Durkin, F. R. Ayers, and B. J. Tromberg, "Quantitation and mapping of tissue optical properties using modulated imaging", *Journal of Biomedical Optics*, vol. 14, no. 2, p. 024 012, 2009.

[47] J. T. Nguyen, S. J. Lin, A. M. Tobias, S. Gioux, A. Mazhar, D. J. Cuccia, Y. Ashitate, A. Stockdale, R. Oketokoun, N. J. Durr, *et al.*, "A novel pilot study using spatial frequency domain imaging to assess oxygenation of perforator flaps during reconstructive breast surgery", *Annals of Plastic Surgery*, vol. 71, no. 3, pp. 308–315, 2013.

[48] A. Policard, "Etude sur les aspects offerts par des tumeurs experimentales examinees a la lumiere de wood", *CR Soc Biol*, vol. 91, pp. 1423–1424, 1924.

[49] T. Vo-Dinh and B. Cullum, "Fluorescence spectroscopy for biomedical diagnostics", in *Biomedical photonics handbook*. Boca Raton, US-FL: CRC Press, 2003, pp. 1–50.

[50] P. Lee, R. M. van den Berg, S. Lam, A. F. Gazdar, K. Grunberg, A. McWilliams, J. LeRiche, P. E. Postmus, and T. G. Sutedja, "Color fluorescence ratio for detection of bronchial dysplasia and carcinoma in situ", *Clinical Cancer Research*, vol. 15, no. 14, pp. 4700–4705, 2009.

[51] P. von Breitenbuch, T. Jeiter, S. Schreml, G. Glockzin, A. Agha, P. Piso, and H. J. Schlitt, "Autofluorescent imaging in patients with peritoneal carcinomatosis", *Surgical Innovation*, vol. 21, no. 2, pp. 187–193, 2013.

[52] O. Buchweitz, A. Staebler, J. Tio, and L. Kiesel, "Detection of peritoneal endometriotic lesions by autofluorescence laparoscopy", *American journal of obstetrics and gynecology*, vol. 195, no. 4, pp. 949–954, 2006.

[53] G. W. Falk, "Autofluorescence endoscopy", *Gastrointestinal Endoscopy Clinics of North America*, vol. 19, no. 2, pp. 209–220, 2009.

[54] M. C. Jacobson, R. deVere White, and S. G. Demos, "In vivo testing of a prototype system providing simultaneous white light and near infrared autofluorescence image acquisition for detection of bladder cancer", *Journal of Biomedical Optics*, vol. 17, no. 3, p. 0 360 111, 2012.

[55] F. J. van den Broek, P. Fockens, S. Van Eeden, M. A. Kara, J. C. Hardwick, J. B. Reitsma, and E. Dekker, "Clinical evaluation of endoscopic trimodal imaging for the detection and differentiation of colonic polyps", *Clinical Gastroenterology and Hepatology*, vol. 7, no. 3, pp. 288–295, 2009.

[56] G. E. Moore, "Fluorescein as an agent in the differentiation of normal and malignant tissues", *Science*, vol. 106, no. 2745, pp. 130–131, 1947.

[57] H. Maeda, J. Wu, T. Sawa, Y. Matsumura, and K. Hori, "Tumor vascular permeability and the epr effect in macromolecular therapeutics: a review", *Journal of controlled release*, vol. 65, no. 1, pp. 271–284, 2000.

[58] M. Noppen, T. Dekeukeleire, S. Hanon, G. Stratakos, K. Amjadi, P. Madsen, M. Meysman, J. D'Haese, and W. Vincken, "Fluorescein-enhanced autofluorescence thoracoscopy in patients with primary spontaneous pneumothorax and normal subjects", *American journal of respiratory and critical care medicine*, vol. 174, no. 1, pp. 26–30, 2006.

[59] K. Koc, I. Anik, B. Cabuk, and S. Ceylan, "Fluorescein sodium-guided surgery in glioblastoma multiforme: a prospective evaluation", *British journal of neurosurgery*, vol. 22, no. 1, pp. 99–103, 2008.

[60] F. Acerbi, M. Broggi, M. Eoli, E. Anghileri, L. Cuppini, B. Pollo, M. Schiariti, S. Visintini, C. Orsi, A. Franzini, *et al.*, "Fluorescein-guided surgery for grade iv gliomas with a dedicated filter on the surgical microscope: preliminary results in 12 cases", *Acta neurochirurgica*, vol. 155, no. 7, pp. 1277–1286, 2013.

[61] J. E. Misas, C. J. Cold, and F. W. Hall, "Vulvar paget disease: fluorescein-aided visualization of margins", *Obstetrics & Gynecology*, vol. 77, no. 1, pp. 156–159, 1991.

[62] L. Yannuzzi, J. Slakter, J. Sorenson, D. Guyer, and D. Orlock, "Digital indocyanine green videoangiography and choroidal neovascularization", *Retina*, vol. 12, no. 3, pp. 191–223, 1992.

[63] D. Miller, W. Gleason, and H. McIntosh, "A comparison of the cardiac output determination by the direct fick method and the dye-dilution method using indocyanine green dye and a cuvette densitometer.", *The Journal of laboratory and clinical medicine*, vol. 59, p. 345, 1962.

[64] E. M. Sevick-Muraca, R. Sharma, J. C. Rasmussen, M. V. Marshall, J. A. Wendt, H. Q. Pham, E. Bonefas, J. P. Houston, L. Sampath, K. E. Adams, *et al.*, "Imaging of lymph flow in breast cancer patients after microdose administration of a near-infrared fluorophore: feasibility study", *Radiology*, vol. 246, no. 3, p. 734, 2008.

[65] F. P. Verbeek, S. L. Troyan, J. S. D. Mieog, G.-J. Liefers, L. A. Moffitt, M. Rosenberg, J. Hirshfield-Bartek, S. Gioux, C. J. van de Velde, A. L. Vahrmeijer, *et al.*, "Near-infrared fluorescence sentinel lymph node mapping in breast cancer: a multicenter experience", *Breast cancer research and treatment*, vol. 143, no. 2, pp. 333–342, 2014.

[66] S.-i. Yamashita, K. Tokuishi, M. Miyawaki, K. Anami, T. Moroga, S. Takeno, M. Chujo, S. Yamamoto, and K. Kawahara, "Sentinel node navigation surgery by thoracoscopic fluorescence imaging system and molecular examination in non-small cell lung cancer", *Annals of surgical oncology*, vol. 19, no. 3, pp. 728–733, 2012.

[67] D. M. Gilmore, O. V. Khullar, S. Gioux, A. Stockdale, J. V. Frangioni, Y. L. Colson, and S. E. Russell, "Effective low-dose escalation of indocyanine green for near-infrared fluorescent sentinel lymph node mapping in melanoma", *Annals of surgical oncology*, vol. 20, no. 7, pp. 2357–2363, 2013.

[68] A. L. Vahrmeijer, M. Hutteman, J. R. van der Vorst, C. J. van de Velde, and J. V. Frangioni, "Image-guided cancer surgery using near-infrared fluorescence", *Nature Reviews Clinical Oncology*, vol. 10, no. 9, pp. 507–518, 2013.

[69] T. Ishizawa, N. Fukushima, J. Shibahara, K. Masuda, S. Tamura, T. Aoki, K. Hasegawa, Y. Beck, M. Fukayama, and N. Kokudo, "Real-time identification of liver cancers by using indocyanine green fluorescent imaging", *Cancer*, vol. 115, no. 11, pp. 2491–2504, 2009.

[70] J. R. van der Vorst, B. E. Schaafsma, M. Hutteman, F. P. Verbeek, G.-J. Liefers, H. H. Hartgrink, V. T. Smit, C. W. Löwik, C. J. van de Velde, J. V. Frangioni, *et al.*, "Near-infrared fluorescence-guided resection of colorectal liver metastases", *Cancer*, vol. 119, no. 18, pp. 3411–3418, 2013.

[71] S. W. Hwang, A. M. Malek, R. Schapiro, and J. K. Wu, "Intraoperative use of indocyanine green fluorescence videography for resection of a spinal cord hemangioblastoma", *Neurosurgery*, vol. 67, no. 3, ons300–ons303, 2010.

[72] P. Ferroli, F. Acerbi, E. Albanese, G. Tringali, M. Broggi, A. Franzini, and G. Broggi, "Application of intraoperative indocyanine green angiography for cns tumors: results on the first 100 cases", in *Intraoperative Imaging*, Springer, 2011, pp. 251–257.

[73] L. Rasetti, G. Rubino, and W. Drago, "Ferrochelatase, ala-dehydrase and ala-synthetase activity in human tumour tissue.", *Panminerva medica*, vol. 9, no. 4, p. 132, 1967.

[74] K. Harada, Y. Harada, M. Beika, N. Koizumi, K. Inoue, Y. Murayama, Y. Kuriu, M. Nakanishi, T. Minamikawa, Y. Yamaoka, *et al.*, "Detection of lymph node metastases in human colorectal cancer by using 5-aminolevulinic acid-induced protoporphyrin ix

fluorescence with spectral unmixing", *International journal of molecular sciences*, vol. 14, no. 11, pp. 23 140–23 152, 2013.

[75] Z. Jun, H. Hui, H. Dalin, L. Runming, W. Dapeng, L. Qingzhi, and L. Xudong, "Value of 5-aminolevulinic acid-induced fluorescence cystoscopy in the diagnosis and treatment of bladder cancer (report of 56 cases)", *Journal of Modern Urology*, vol. 3, p. 016, 2006.

[76] R. Baumgartner, R. Huber, H. Schulz, H. Stepp, K. Rick, F. Gamarra, A. Leberig, and C. Roth, "Inhalation of 5-aminolevulinic acid: a new technique for fluorescence detection of early stage lung cancer", *Journal of Photochemistry and Photobiology B: Biology*, vol. 36, no. 2, pp. 169–174, 1996.

[77] W. Stummer, U. Pichlmeier, T. Meinel, O. D. Wiestler, F. Zanella, and H.-J. Reulen, "Fluorescence-guided surgery with 5-aminolevulinic acid for resection of malignant glioma: a randomised controlled multicentre phase iii trial", *The Lancet Oncology*, vol. 7, no. 5, pp. 392–401, 2006.

[78] D. Hanahan and R. A. Weinberg, "The hallmarks of cancer", *cell*, vol. 100, no. 1, pp. 57–70, 2000.

[79] R. Weissleder and V. Ntziachristos, "Shedding light onto live molecular targets", *Nature medicine*, vol. 9, no. 1, pp. 123–128, 2003.

[80] S. Folli, G. Wagnieres, A. Pelegrin, J. Calmes, D. Braichotte, F. Buchegger, Y. Chalandon, N. Hardman, C. Heusser, and J. Givel, "Immunophotodiagnosis of colon carcinomas in patients injected with fluoresceinated chimeric antibodies against carcinoembryonic antigen", *Proceedings of the National Academy of Sciences*, vol. 89, no. 17, pp. 7973–7977, 1992.

[81] G. M. van Dam, G. Themelis, L. M. A. Crane, N. J. Harlaar, R. G. Pleijhuis, W. Kelder, A. Sarantopoulos, J. S. de Jong, H. J. G. Arts, A. G. J. van der Zee, B. Joost, P. S. Low, and V. Ntziachristos, "Intraoperative tumor-specific fluorescence imaging in ovarian cancer by folate receptor-α targeting: first in-human results", *Nature Medicine*, vol. 17, no. 10, pp. 1315–1319, 2011.

[82] K. R. Kalli, A. L. Oberg, G. L. Keeney, T. J. Christianson, P. S. Low, K. L. Knutson, and L. C. Hartmann, "Folate receptor alpha as a tumor target in epithelial ovarian cancer", *Gynecologic oncology*, vol. 108, no. 3, pp. 619–626, 2008.

[83] W. Scheuer, G. van Dam, M. Dobosz, M. Schwaiger, and V. Ntziachristos, "Drug-based optical agents: infiltrating clinics at lower risk", *Science Translational Medicine*, vol. 4, no. 134, 134ps11–134ps11, 2012.

[84] E. M. Sevick-Muraca, W. J. Akers, B. P. Joshi, G. D. Luker, C. S. Cutler, L. J. Marnett, C. H. Contag, T. D. Wang, and A. Azhdarinia, "Advancing the translation of optical imaging agents for clinical imaging", *Biomedical optics express*, vol. 4, no. 1, p. 160, 2013.

[85] M. V. Marshall, D. Draney, E. M. Sevick-Muraca, and D. M. Olive, "Single-dose intravenous toxicity study of IRDye 800CW in Sprague-Dawley rats", *Molecular Imaging and Biology*, vol. 12, no. 6, pp. 583–594, 2010.

[86] V. Ntziachristos, "Going deeper than microscopy: the optical imaging frontier in biology", *Nature Methods*, vol. 7, no. 8, pp. 603–614, 2010.

[87] A. Amelink and H. J. Sterenborg, "Measurement of the local optical properties of turbid media by differential path-length spectroscopy", *Applied Optics*, vol. 43, no. 15, pp. 3048–3054, 2004.

[88] G. Themelis, J. Yoo, K. Soh, R. Schulz, and V. Ntziachristos, "Real-time intraoperative fluorescence imaging system using light-absorption correction", *Journal of Biomedical Optics*, vol. 14, no. 6, p. 064 012, 2009.

[89] P. A. Valdés, F. Leblond, A. Kim, B. T. Harris, B. C. Wilson, X. Fan, T. D. Tosteson, A. Hartov, S. Ji, K. Erkmen, *et al.*, "Quantitative fluorescence in intracranial tumor: implications for ala-induced ppix as an intraoperative biomarker", *Journal of Neurosurgery*, vol. 115, no. 1, p. 11, 2011.

[90] A. Bogaards, H. J. C. M. Sterenborg, and B. C. Wilson, "In vivo quantification of fluorescent molecular markers in real-time: a review to evaluate the performance of five existing methods", *Photodiagnosis and Photodynamic Therapy*, vol. 4, no. 3, pp. 170–178, 2007.

[91] T. Pyka, R. Schulz, A. Ale, and V. Ntziachristos, "Revisiting the normalized born approximation: effects of scattering", *Optics letters*, vol. 36, no. 22, pp. 4329–4331, 2011.

[92] G. Zonios and A. Dimou, "Modeling diffuse reflectance from semi-infinite turbid media: application to the study of skin optical properties", *Optics express*, vol. 14, no. 19, pp. 8661–8674, 2006.

[93] N. Biswal, S. Gupta, N. Ghosh, and A. Pradhan, "Recovery of turbidity free fluorescence from measured fluorescence: an experimental approach", *Optics express*, vol. 11, no. 24, pp. 3320–3331, 2003.

[94] S. D. Konecky, C. M. Owen, T. Rice, P. A. Valdés, K. Kolste, B. C. Wilson, F. Leblond, D. W. Roberts, K. D. Paulsen, and B. J. Tromberg, "Spatial frequency domain tomography of protoporphyrin ix fluorescence in preclinical glioma models", *Journal of biomedical optics*, vol. 17, no. 5, pp. 0 560 081–0 560 087, 2012.

[95] S. Popoff, G. Lerosey, M. Fink, A. C. Boccara, and S. Gigan, "Image transmission through an opaque material", *Nature Communications*, vol. 1, p. 81, 2010.

[96] I. M. Vellekoop and A. Mosk, "Focusing coherent light through opaque strongly scattering media", *Optics letters*, vol. 32, no. 16, pp. 2309–2311, 2007.

[97] J. Bertolotti, E. G. van Putten, C. Blum, A. Lagendijk, W. L. Vos, and A. P. Mosk, "Non-invasive imaging through opaque scattering layers", *Nature*, vol. 491, no. 7423, pp. 232–234, 2012.

[98] B. Beauvoit, S. M. Evans, T. W. Jenkins, E. E. Miller, and B. Chance, "Correlation between the light scattering and the mitochondrial content of normal tissues and transplantable rodent tumors", *Analytical Biochemistry*, vol. 226, no. 1, pp. 167–174, 1995.

[99] Q. Li, X. He, Y. Wang, H. Liu, D. Xu, and F. Guo, "Review of spectral imaging technology in biomedical engineering: achievements and challenges", *Journal of biomedical optics*, vol. 18, no. 10, pp. 100 901–100 901, 2013.

[100] S. Tomatis, M. Carrara, A. Bono, C. Bartoli, M. Lualdi, G. Tragni, A. Colombo, and R. Marchesini, "Automated melanoma detection with a novel multispectral imaging system: results of a prospective study", *Physics in medicine and biology*, vol. 50, no. 8, p. 1675, 2005.

[101] M. A. Afromowitz, J. B. Callis, D. M. Heimbach, L. A. DeSoto, and M. K. Norton, "Multispectral imaging of burn wounds: a new clinical instrument for evaluating burn depth", *Biomedical Engineering, IEEE Transactions on*, vol. 35, no. 10, pp. 842–850, 1988.

[102] D. Mordant, I. Al-Abboud, G. Muyo, A. Gorman, A. Sallam, P. Ritchie, A. Harvey, and A. McNaught, "Spectral imaging of the retina", *Eye*, vol. 25, no. 3, pp. 309–320, 2011.

[103] T. Vo-Dinh, B. Cullum, and P. Kasili, "Development of a multi-spectral imaging system for medical applications", *Journal of Physics D: Applied Physics*, vol. 36, no. 14, p. 1663, 2003.

[104] A. Mazhar, S. Dell, D. J. Cuccia, S. Gioux, A. J. Durkin, J. V. Frangioni, and B. J. Tromberg, "Wavelength optimization for rapid chromophore mapping using spatial frequency domain imaging", *Journal of biomedical optics*, vol. 15, no. 6, pp. 061 716–061 716, 2010.

[105] I. M. Orfanoudaki, G. C. Themelis, S. K. Sifakis, D. H. Fragouli, J. G. Panayiotides, E. M. Vazgiouraki, and E. E. Koumantakis, "A clinical study of optical biopsy of the uterine cervix using a multispectral imaging system", *Gynecologic oncology*, vol. 96, no. 1, pp. 119–131, 2005.

Chapter 2

Imaging system development

2.1 Intra-operative imaging system

One of the major technological challenges for the intra-operative imaging of color and NIR fluorescence is the development of an adequate camera system. The setup developed herein is based on previously published imaging system setups [1, 2] that were successfully employed in a number of studies [3–5]. However, the previous incarnation was subject to various limitations concerning real-time processing, mechanical handling and integrated hardware control, which were addressed in the current, second generation setup.

2.1.1 System design

An imaging system that is to be used in a clinical operating room (OR) needs to fulfill several requirements. One important advantage of optical imaging over other non-invasive radiological methods is its compact and lightweight equipment. This needs to be translated into the camera system design to offer a setup that is easily transportable and can be integrated into surgical procedures with minimal interference. The camera should also be stable, easy to clean and to sterilize for usage during surgery, where an abacterial environment is of utmost importance.

Fluorescence molecular imaging for intra-operative guidance requires the detection of fluorochromes even at low concentrations or below the surface, which can only be achieved with a high sensitivity camera that offers low readout noise and high quantum efficiency. However, a fluorescence image alone often is of limited use as it provides little anatomical and struc-

tural information about the environment. This can make orientation difficult for the surgeon, especially if a small field of view (FOV) is being imaged. For this reason it is important to simultaneously capture color images of the FOV on a second camera as well. Consequently, one crucial processing step is the generation of a composite image that can be displayed to the user and contains both the color information as well as the fluorescence signal, superimposed in pseudo-color.

Surgical imaging aims to offer instant feedback about tissues and molecular properties to the physician. A prerequisite for natural interaction and easy orientation is imaging at video frame rates. Hence the cameras should acquire at low exposure times, which also avoids motion artifacts, and the computer system needs to be able to process the measured data at a sufficiently high speed in real-time. The user should interact with the system via a graphical user interface (GUI) that displays the images and allows the camera parameters to be controlled. Given the above requirements, the following design goals were formulated for the setup:

- Compact and lightweight design
- Easy to clean and sterilize, preferably enclosing sensitive components
- High sensitivity fluorescence detection
- Concurrent color and fluorescence imaging
- Acquisition at video frame rates
- Composite overlay image of molecular and structural information
- Processing in real-time on a single computer system
- A user interface to control all relevant camera parameters
- Easily adaptable for use in endoscopy or laparoscopy

The basic system design and setup for epi-fluorescence imaging in an intra-operative environment is discussed in Section 2.1.2 while the custom developed imaging software is presented in Section 2.1.3. The integrated image processing steps are described in Sections 2.1.4 and 2.1.5. Clinical scopes that were considered for endoscopic or laparoscopic fluorescence imaging are characterized in Section 2.2.1. Finally, the adaptation and characterization of the setup is described for laparoscopy in Section 2.2.2, cholangiopancreatoscopy in Section 2.2.3 and colonoscopy in Section 2.2.4.

2.1.2 Setup for epi-fluorescence imaging

The imaging system setup for concurrent acquisition of color and near-infrared fluorescence measurements is shown in Figure 2.1. The field of view was illuminated by a 250 W halogen lamp (KL-2500 LCD, Schott AG, Mainz, Germany) to facilitate reflectance color measurements. In order to avoid crosstalk to the fluorescence channel, the white light was filtered by a shortpass filter (E700SP, Chroma Technology, Rockingham, US-VT) to remove the NIR wavelength band. An aspheric condensor lens (ACL2520, Thorlabs, Newton, US-NJ) was used to focus the light onto the FOV. Fluorescence excitation was provided by a 300 mW laser diode, emitting a continuous wave (CW) at 750 nm (BWF2-750-0, B&W Tek, Newark, US-DE). A beam collimator (F260SMA-B, Thorlabs) and a ground glass diffusor (DG10-220, Thorlabs) were used to achieve uniform laser power distribution. White light reflectance and epi-fluorescence images were collected and focused by a lens objective (CVO GAZ11569M, Stemmer Imaging GmbH, Puchheim, Germany). A custom made USB-connected lens control unit based on the Arduino Uno microcontroller board allowed for the programmatic regulation of zoom, focus and iris settings. The image wavelengths were separated by a dichroic mirror (700DCXXR, AHF analysentechnik AG, Tübingen, Germany) and projected onto two CCDs by relay lenses (MAP10100100-A1, Thorlabs, Newton, US-NJ). A shortpass (ET700SP-2P, Chroma) was placed in the color channel to filter the NIR excitation light. A NIR emission filter (ET810/90, Chroma) in the fluorescence channel was used to detect fluorochrome signals in the 765-855 nm spectral band. Color images were acquired by a 12-bit CCD camera (pixelfly qe, PCO AG, Kelheim, Germany), while the fluorescence image was recorded by an iXon 3 electron multiplying charge-coupled device (EMCCD) (DU-897, Andor Technology, Belfast, Northern Ireland).

Figure 2.2 shows the transmission over wavelength of the filters and dichroic employed in the setup, visualizing the obtained passbands. The fluorescence channel collects light mainly from the NIR wavelengths, while the visible range is guided to the color channel. Thus a concurrent acquisition of the distinct spectral bands was achieved.

Two photographs of the developed intra-operative imaging system are displayed in Figure 2.3. Figure 2.3A shows the cameras and optics attached to an aluminum frame (Böhm+Wiedemann, Eching, Germany) that is mounted on a surgical microscope arm (Carl Zeiss, Jena, Germany) and enclosed by a protective housing (KL Technik GmbH, Krailling, Germany). The mounted system is covered in sterile surgical drapes for use in the operating room, as shown in Figure

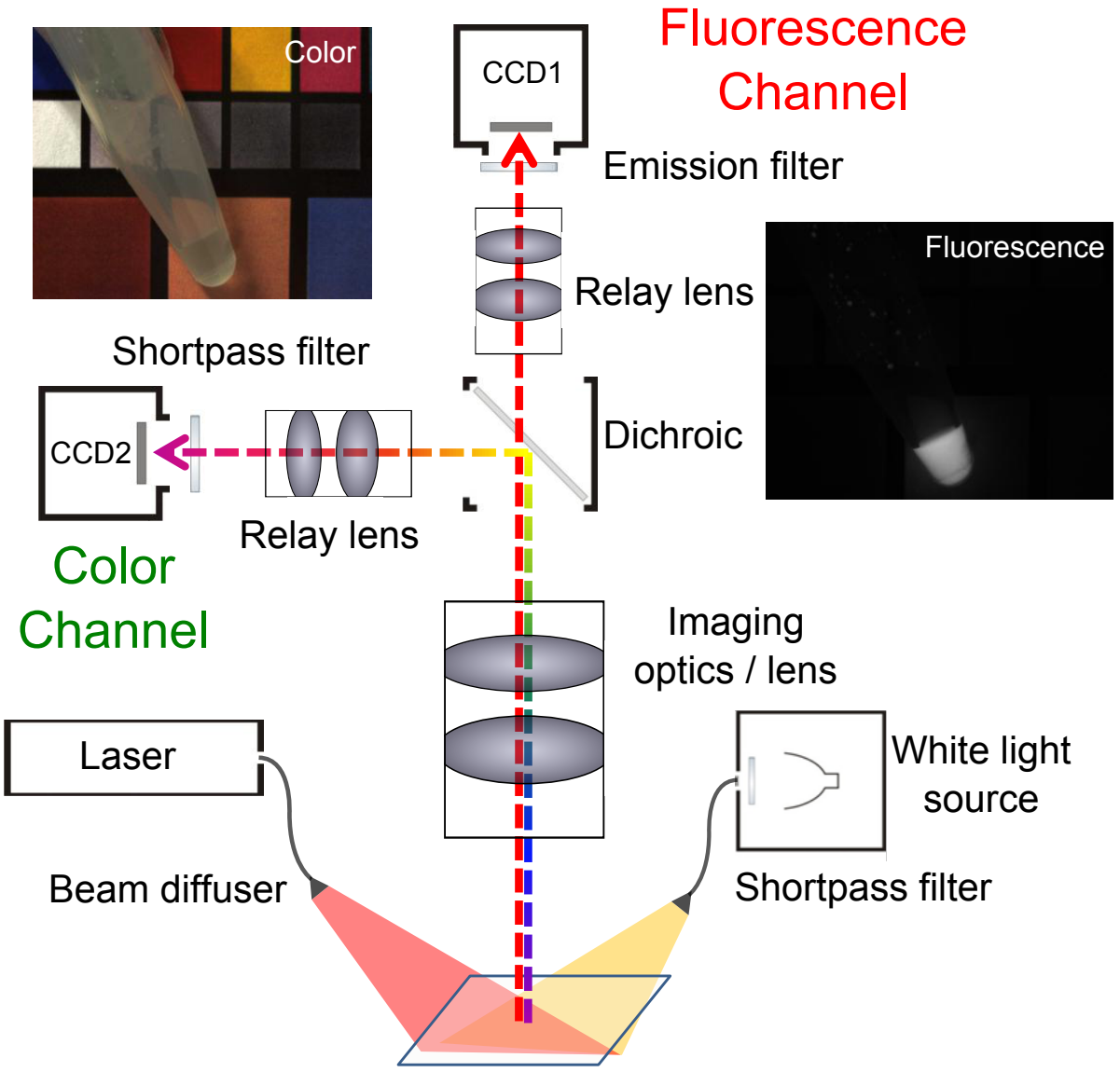

Figure 2.1: Schematic of the two channel imaging system for concurrent color and NIR fluorescence acquisition.

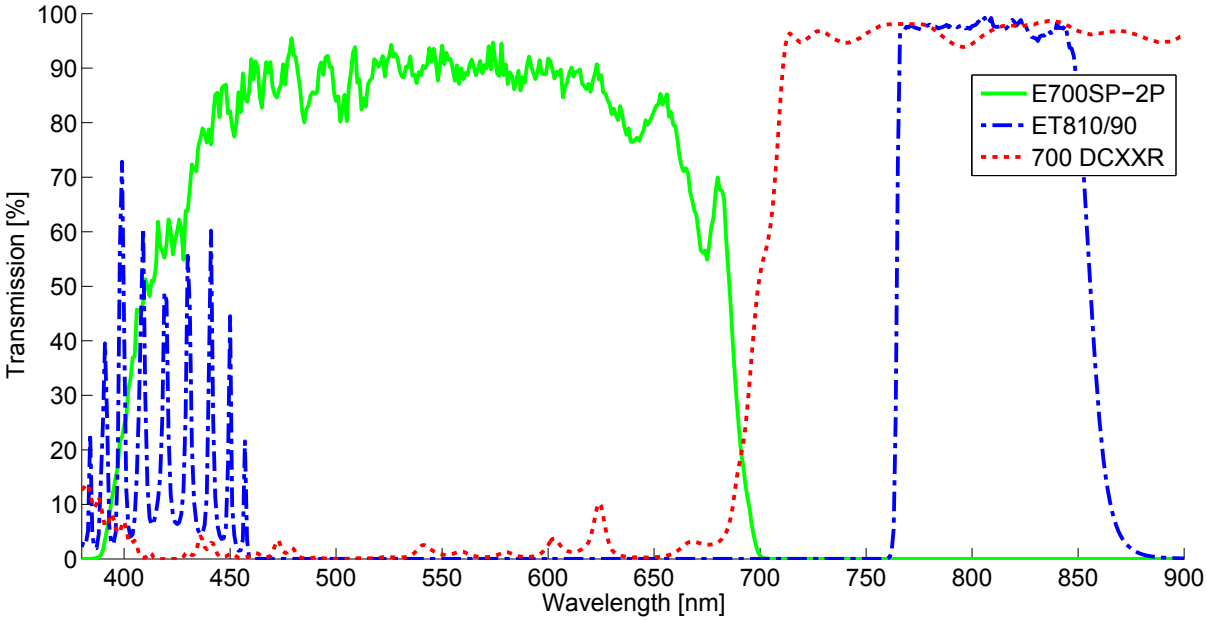

Figure 2.2: Transmission spectra of the utilized fluorescence emission bandpass (ET810/90), dichroic mirror (700 DCXXR), and shortpass filters (E700SP-2P).

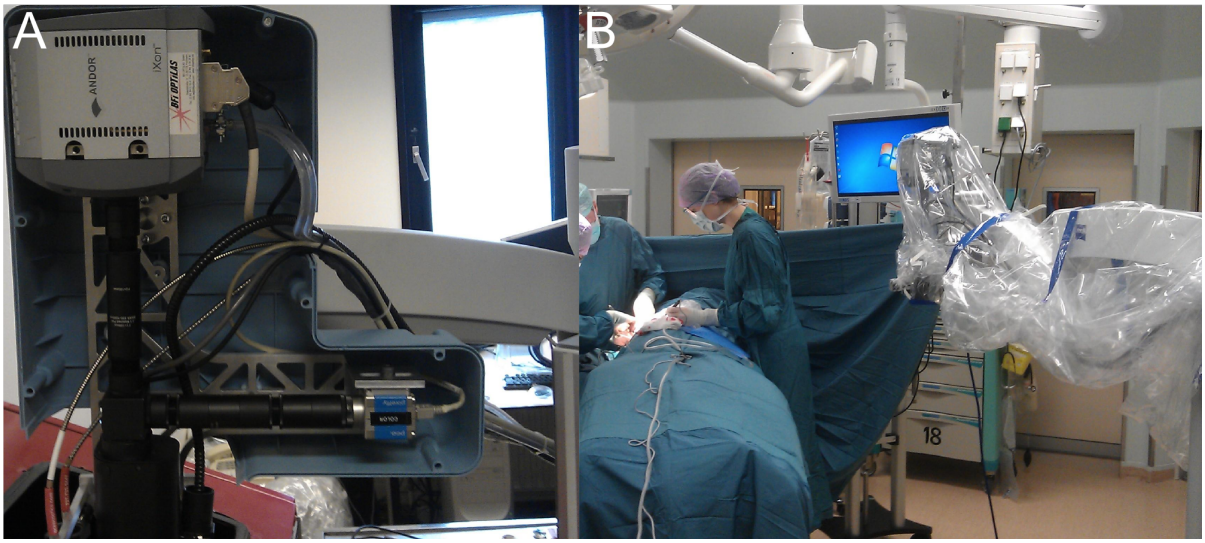

Figure 2.3: A) Intra-operative imaging system mounted on a surgical arm and enclosed by protective housing. B) System covered by sterile drapes during surgical use.

2.3B.

2.1.3 Imaging software

Fast data transfer is a necessity for video-rate imaging. Thus, both cameras were connected to peripheral component interconnect (PCI) acquisition cards that enabled direct memory access (DMA) into the computer's RAM. Imaging at video frame rates resulted in a significant data volume, where color and fluorescence image pairs of up to 1.3 MPixel resolution and up to 14 bits are measured at 12 frames per second (fps). A solid-state-drive (SSD) (256 GB, SATA-III 6 Gb/s, Liteon, Taiwan) was chosen due to its fast access speed and lack of latency caused by mechanical components to save the raw image data [6]. The images are then transferred to the memory of the computer's graphics processing unit (GPU) (Quadro 5000, Nvidia Corporation, Santa Clara, US-CA) for postprocessing. The implemented pipeline for image transfer and processing is shown in Figure 2.4.

A custom designed software was developed in C/C++ to integrate data transfer from and to the hardware components, postprocessing and visualization, as well as the interface for user interaction. Significant speedups have been reported for architectures using the GPU as a coprocessor [7] and, since many image processing operations can easily be parallelized, a GPU based computation architecture was realized. The fluorescence images are resized to the color channel resolution and registered by applying a projective transformation that is calculated from user-selected control points in an initial calibration step. The necessary image processing operations on the GPU were realized using the NPP library and custom developed CUDA implementations, as described in Section 3.1. The user interface displays the co-registered color and fluorescence channel images as well as the composite overlay. Furthermore the interface offers easy control of all relevant system parameters and the possibility to capture both individual images and H.264/MPEG-4 recordings of the color and fluorescence channels and their overlay.

The software interface is shown in Figure 2.5, consisting of the image displays (A), image statistics as histograms (B), user control elements (C) and status feedback controls (D). Both automatic adjustment and manual control of the camera acquisition parameters, such as gain, exposure time and binning are available through the interface.

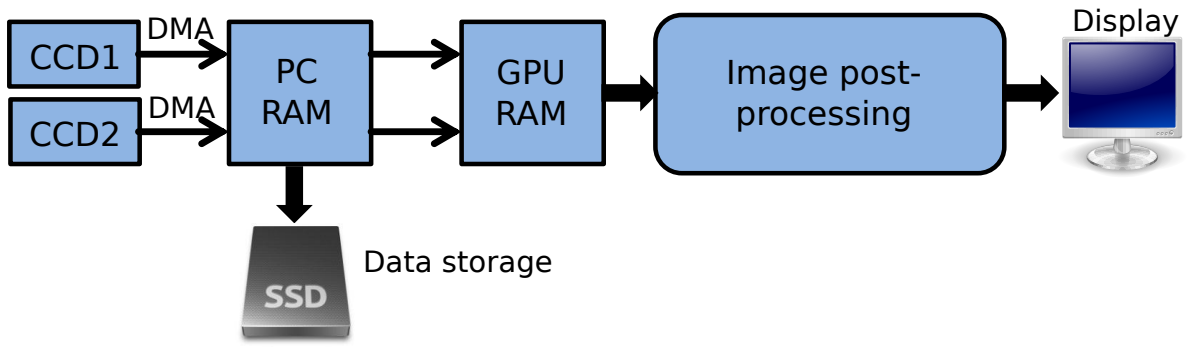

Figure 2.4: Schematic of the software pipeline. Camera data are acquired via DMA and transferred to the GPU, where post-processing is performed and the overlay is generated. Finally, the images are displayed in 8-bit resolution on the monitor.

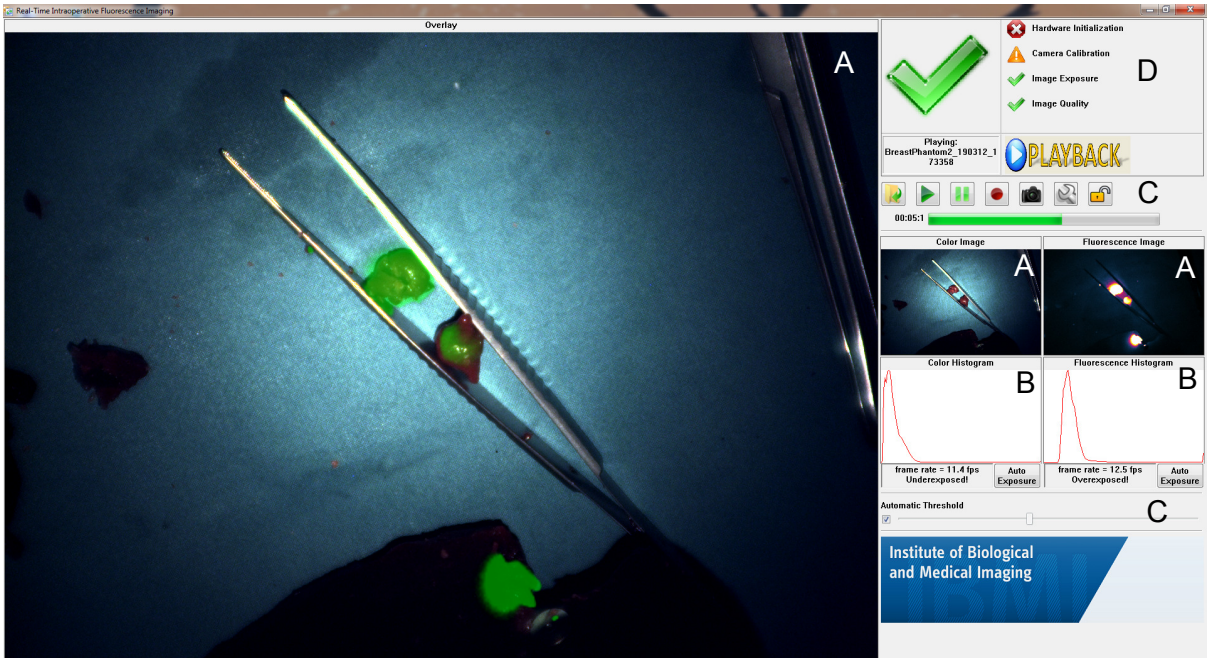

Figure 2.5: Custom designed software interface, consisting of image displays (A), histograms (B), controls (C) and status feedback (D).

2.1.4 Image post-processing

A major task of the system's software is the image post-processing, whereby the acquired raw data is prepared for real-time presentation to the physician. The image processing pipeline is displayed in Figure 2.6. The color image was acquired using a color filter array (CFA) on top of the charge-coupled device (CCD). The interpolation of the missing color values on the GPU, termed demosaicking, is described in more detail in Section 3.1.4. Additionally, white balancing was applied to correct for the spectral properties of the camera sensor and the illumination.

$$\begin{bmatrix} \mathbf{R}_{wb} \\ \mathbf{G}_{wb} \\ \mathbf{B}_{wb} \end{bmatrix} = \begin{bmatrix} c_R & c_G & c_B \end{bmatrix} \begin{bmatrix} \mathbf{R} \\ \mathbf{G} \\ \mathbf{B} \end{bmatrix} \tag{2.1}$$

Thereby c_R, c_G and c_B are constants obtained in a previous calibration step, typically from a white reflectance standard image. The fluorescence image was resized to the color channel resolution using bilinear interpolation and then co-registered by a perspective transform. The transformation matrix $\mathbf{T}_p$ was obtained from a calibration measurement where either the corners of a checkerboard target were automatically detected [8] or corresponding control point pairs were selected manually [9].

$$\mathbf{T}_p = \begin{bmatrix} t_{00} & t_{01} & t_{02} \\ t_{10} & t_{11} & t_{12} \\ t_{20} & t_{21} & t_{22} \end{bmatrix} \tag{2.2}$$

The destination coordinates (u, v) were then computed from the original coordinates (x, y) as follows:

$$u = \frac{t_{00}x + t_{01}y + t_{02}}{t_{20}x + t_{21}y + t_{22}} \tag{2.3}$$

$$v = \frac{t_{10}x + t_{11}y + t_{12}}{t_{20}x + t_{21}y + t_{22}} \tag{2.4}$$

After co-registration the composite overlay is generated from the color and fluorescence images.

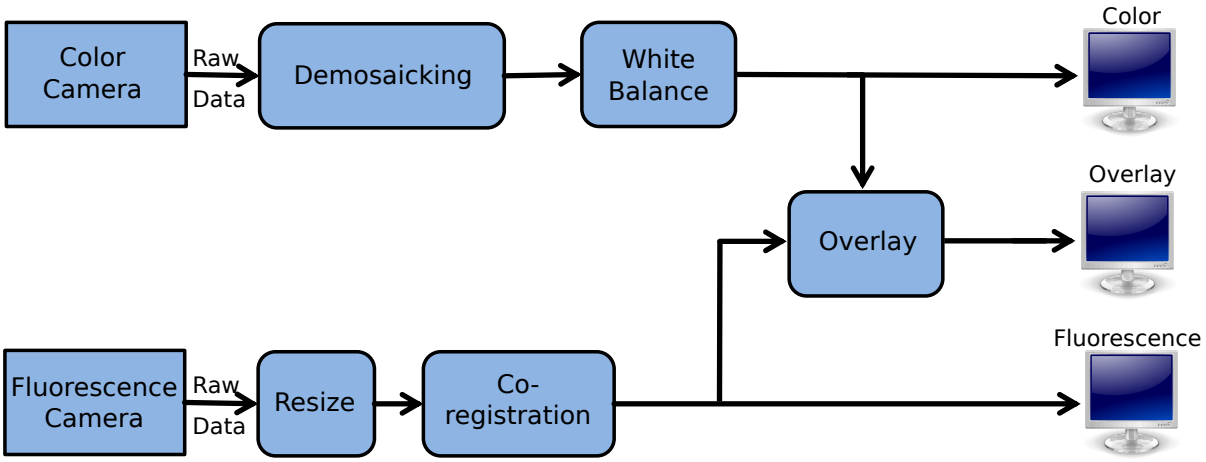

Figure 2.6: Schematic of the image processing pipeline. Color images undergo demosaicking and white balancing, while the fluorescence image is resized and co-registered to the color coordinate system. Finally both images are combined to yield the composite overlay.

2.1.5 Color and fluorescence image overlay[1]

Intra-operative imaging systems such as the ones presented in Refs. [11] or [12] usually capture the fluorescence emission waveband as well as an additional color image. In order to provide the surgeon with easy and intuitive orientation that matches his field of view, the detected fluorescence signal is superimposed on the color image.

Typically, a pseudocolor image is generated by superimposing the fluorescence image over the color image in lime green using alpha blending [13]. A transparent overlay can be used to maintain the structural information present in the color image while adding the molecular information of the fluorescence distribution.

Biological data visualization requires standardization and robustness to be intuitively interpretable and easily transferable. However, a transparent green overlay is not robust, since it is based on the presence of a predominantly redish tissue background. Thus, in the cases where this assumption is violated, it will produce low contrast and an inappropriate visualization. Instead, alternative schemes were developed to select the superimposed color in an adaptive way that does not make a priori assumptions on the sample's color appearance. Furthermore, a novel visualization method for video-rate surgical fluorescence imaging that modulates transparency and color over the time is also proposed.

[1] Text and images of this section have been published in Ref. [10]

2.1.5.1 Overlay Methods

Image Processing Before the two acquisition channels can be merged into a composite image, the processing steps outlined in Section 2.1.4 are performed. In order to restrict the superimposed fluorescence signal to physiologically relevant information, denoising and thresholding can be applied to remove autofluorescence, filter cross-talk and other parasitic signals [14]. An appropriate threshold can be determined either manually, or by an automatic thresholding or segmentation algorithm [15, 16]. Herein, Otsu's method [17] was used to determine the threshold T, for which the preprocessed fluorescence image $\mathbf{F}'$ is then calculated from the measured intensity image $\mathbf{F}$ as

$$\mathbf{F}' = \max\left(0, \mathbf{F} - T\right) \tag{2.5}$$

The composite image was evaluated by computing the color contrast ΔE_{00} between the superimposed fluorescence region and the surrounding area in the overlay using the CIEDE2000 formula [18]. Thereby, a high value indicates that the fluorescent region is colored in a way that can easily be distinguished from the nearby regions.

Alpha Blending Alpha blending combines the two images by weighting individual pixels with the transparency value α [13]. Blending the fluorescence image $\mathbf{F}'$ and the color image $\underline{\mathbf{C}}$ with RGB channels $\begin{bmatrix} \mathbf{C}_R & \mathbf{C}_G & \mathbf{C}_B \end{bmatrix}^T$ is given as

$$\begin{bmatrix} \mathbf{P}_R \\ \mathbf{P}_G \\ \mathbf{P}_B \end{bmatrix} = (1-\alpha) \begin{bmatrix} \mathbf{C}_R \\ \mathbf{C}_G \\ \mathbf{C}_B \end{bmatrix} + \alpha \mathbf{F}' \begin{bmatrix} O_R \\ O_G \\ O_B \end{bmatrix} \tag{2.6}$$

$$\underline{\mathbf{P}} = (1-\alpha)\,\underline{\mathbf{C}} + \alpha \mathbf{F}' \underline{O} \tag{2.7}$$

Thereby $\underline{\mathbf{P}}$ is the composite image, $\alpha \in [0;1]$ is the transparency, and $\underline{O}$ is the pseudocolor of the overlay. Lime green, i.e. $\underline{O} = \begin{bmatrix} 0 & 1 & 0 \end{bmatrix}^T$, was chosen as the default color for the superimposition on biological tissue. Additionally, a pixel-wise variable map for the transparency was applied to obtain smoother transitions between areas above and below the fluorescence

threshold. For a maximum transparency α_{max}, this can be written as

$$\boldsymbol{\alpha} = \alpha_{max} \frac{\mathbf{F}'}{\max\left(\mathbf{F}'\right)} \tag{2.8}$$

HSV-based Color Selection An adaptive approach to select a pseudocolor $\underline{O}$ that yields a strong contrast is based on picking a color that is underrepresented in the region of interest (ROI). The color image was transformed into HSV representation [19], a cylindrical-coordinate transformation where color is represented by its hue, saturation and value/brightness, and the average hue H_{avg} was calculated in the ROI where the fluorescence lies above the threshold. The hue of the overlay color was chosen to lie on the opposite side of the HSV cone, while both the saturation and value were set to 1.

$$\underline{O}_{HSV} = \begin{bmatrix} \mathrm{mod}\left(H_{avg} + 180°, 360°\right) \\ 1 \\ 1 \end{bmatrix} \tag{2.9}$$

The obtained color was transformed back into the RGB space and utilized for alpha blending as described above.

PCA-based Color Selection Alternatively, robust overlay was done by principal component analysis (PCA) [20] of the color image, where the data are projected onto a set of linearly uncorrelated base vectors. Thereby, the ROI was vectorized and PCA was performed to yield the principal component loadings $\underline{\mathbf{U}}$. The transformation of the color image into the coordinate system spanned by the principal component eigenvectors is given by

$$\underline{\mathbf{C}}_{PCA} = \underline{\mathbf{U}}^T \underline{\mathbf{C}} \tag{2.10}$$

As the principal components are ordered by their statistical contribution to the original image, the pre-processed fluorescence image was superimposed on the third, least significant component in order to achieve the highest contrast to the main image features.

$$\underline{\mathbf{P}}_{PCA} = \left(1 - \boldsymbol{\alpha}\right) \underline{\mathbf{U}}^T \underline{\mathbf{C}} + \boldsymbol{\alpha} \mathbf{F}' \begin{bmatrix} 0 \\ 0 \\ 1 \end{bmatrix} \tag{2.11}$$

The composite image was then transformed back into the original RGB color space.

$$\underline{\mathbf{P}} = \underline{\mathbf{U}} \left((1 - \boldsymbol{\alpha}) \, \underline{\mathbf{U}}^T \underline{\mathbf{C}} + \boldsymbol{\alpha} \mathbf{F}' \begin{bmatrix} 0 \\ 0 \\ 1 \end{bmatrix} \right) \tag{2.12}$$

Since the eigenvector matrix $\underline{\mathbf{U}}$ is orthonormal, this equation simplifies to

$$\underline{\mathbf{P}} = (1 - \boldsymbol{\alpha}) \, \underline{\mathbf{C}} + \boldsymbol{\alpha} \mathbf{F}' \underline{\mathbf{U}} \begin{bmatrix} 0 \\ 0 \\ 1 \end{bmatrix} \tag{2.13}$$

Thus, blending the fluorescence over the least significant principal component is equivalent to selecting the eigenvector with the smallest eigenvalue as the overlay "color" for alpha blending in RGB space.

Animated Overlay The methods discussed so far aim to integrate the fluorescence information into the spectral components of the color image, generating the contrast by selecting a color that is underrepresented in the image. Alternatively, especially in the case of continuously acquired clinical images, the signal can also be visualized along the temporal dimension. It was assumed that the image changes slowly compared to the acquisition frame rate, hence changes occurring with a higher temporal frequency are easily identifiable in the overlay. The temporal alpha blending can then be written as

$$\underline{\mathbf{P}}(t) = (1 - \boldsymbol{\alpha}(t)) \, \underline{\mathbf{C}} + \boldsymbol{\alpha}(t) \mathbf{F}' \underline{O}(t) \tag{2.14}$$

For example, a sinusoidal curve can be used to vary transparency with a frequency of 2 Hz and the overlay color hue with 1 Hz.

Biological Samples Color and epi-fluorescence images from a variety of biological studies[2], as shown in Figure 2.7, were chosen to test and validate the proposed algorithms. Image set

[2]I would like to thank Mrs. Zhen Bi and Professor Dr. J. P. Schnitzler for the leaf samples, Professor Dr. G. G. Westmeyer for the zebrafish sample, Dr. Strizker and Professor Dr. Szalay for the melanin and GFP expressing tumor samples, Dr. Vladimir Ermolayev for the 4T1 mouse, Dr. Wouter Nagengast for proving the intraperitoneal tumor mice and the cetuximab-CW800 contrast agent and Professor Dr. Gooitzen van Dam and Professor Dr. E. G. Elisabeth de Vries for the bevacizumab-CW800 agent.

A stems from a study of leaves transpiration and vasculature network, where the leaf absorbed Alexa Fluor 750 (Molecular Probes, Eugene, US-OR) through its petiolule. The images of sets B and C were acquired using a prototype cryoslicer-based imaging system [21]. Set B shows an axial section of a mouse bearing a tumor targeted by a virus that expressed green fluorescent protein (GFP) and melanin [22]. In image set C, two zebrafish with pan-neuronal expression of GFP embedded in the same block are depicted. In set D, we imaged a near-infrared probe (cetuximab-CW800) targeting intraperitoneal tumors (HT29luc2) through the intact skin of a nude mouse [23]. In dataset E, we simulated an intra-operative scenario using a subcutaneous 4T1 tumor targeted with bevacizumab-CW800 [24].

2.1.5.2 Results

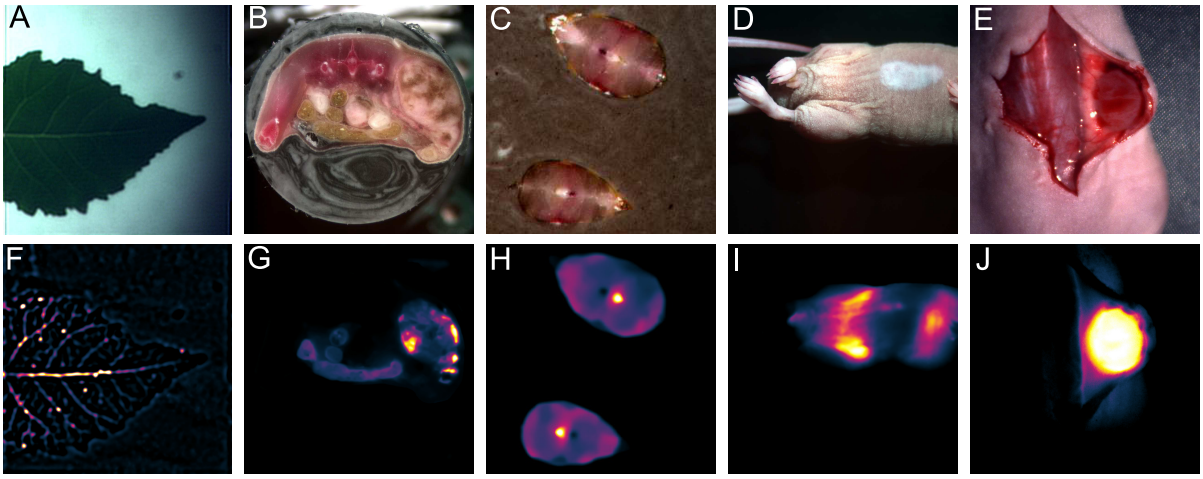

Figure 2.7: Color images of the leaf, melanin and GFP expressing mouse, GFP expressing zebrafish, transcutaneous imaging of an intraperitoneal tumor in a mouse and intra-operative imaging of a subcutaneous tumor (A–E) as well as corresponding fluorescence images (F–J).

Color images acquired from the five biological samples are displayed in Figs. 2.7A–E, while the corresponding fluorescence channel is shown in Figs. 2.7F–J. The mouse images contain parasitic signals from intestinal autofluorescence (Fig. 2.7G), skin autofluorescence (Figs. 2.7I and J), and contrast agent accumulation in the liver (Fig. 2.7I). The images were co-registered and automatic segmentation of the fluorescence signal was performed using Otsu's method. The ROI was defined for each image as the area containing fluorescence signal above the threshold.

Overlay images were calculated for all the datasets using the pseudogreen alpha blending, color picking in HSV space, and the PCA-based alpha blending. Figures 2.8A–E show the overlay in lime green, which performs best in the case of a predominantly red background (Fig. 2.8E). The color selection in HSV space is plotted in Figs. 2.8F–J. The algorithm picks various shades of cyan for the animal tissue and an orange color for overlay on the leaf. Color selection using PCA is shown in Figs. 2.8K–O and yields a wider range of colors for the different datasets.

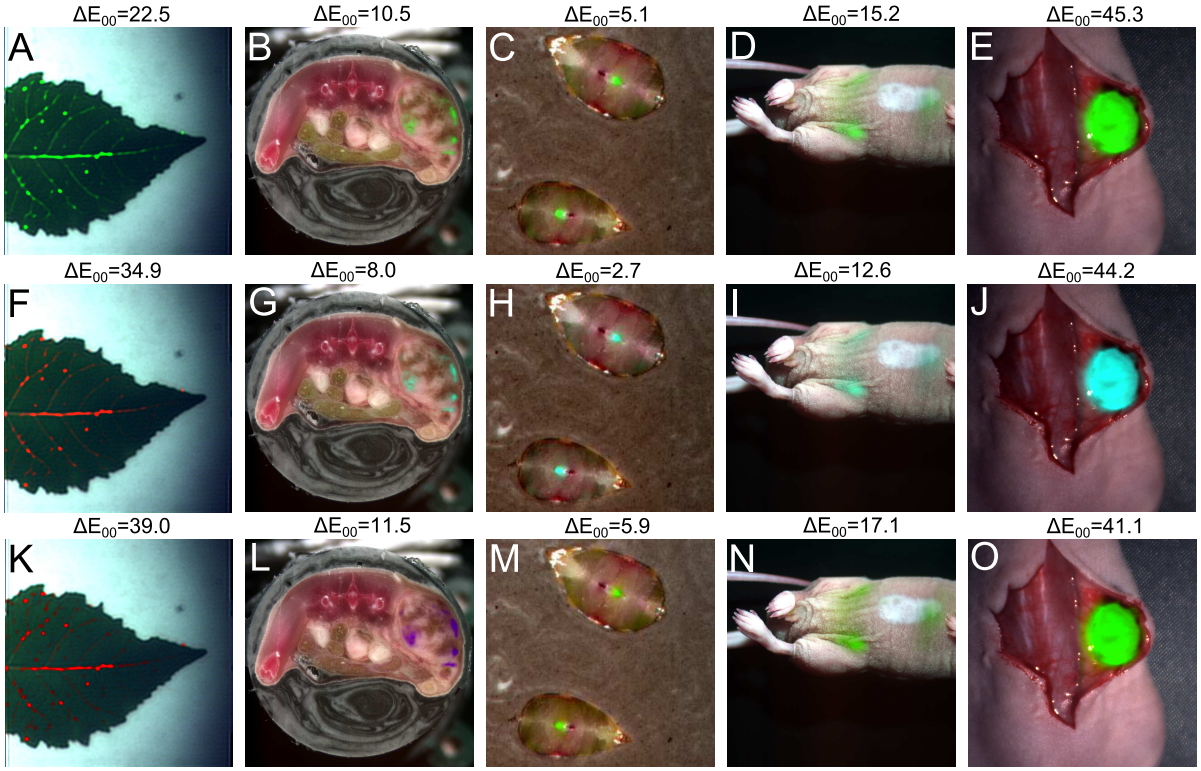

Figure 2.8: Overlay images generated from the color and fluorescence data shown in Figure 2.7 and corresponding color contrast values. (A–E) Pseudogreen alpha blending. (F–J) Robust overlay color selection in HSV space. (K–O) Robust overlay color selection from principal component analysis.

The average value of ΔE_{00} over the five datasets was computed to be 19.7 for the lime green, 20.5 for the HSV method, and 23.0 for the PCA method, respectively. The two adaptive methods provide a good average color contrast, yet it is notable that the HSV method yielded an unsatisfactory result for dataset C, while the PCA selection seems more consistent in selecting an appropriate overlay color.

2.1.5.3 Discussion

The ongoing translation of fluorescence molecular imaging into clinical and surgical practice calls for standardized and robust ways to represent multispectral data. Fluorescence emission wavebands contain molecular information on tissue that is invisible to the human eye, while additional color images provide anatomical information and easy orientation. In this section, methods for the fusion of multispectral fluorescence data into a composite RGB image were investigated.

Among those, the overlay in lime green is widely used for biological tissue, but it is based on a priori assumptions about the spectral characteristics of the imaged sample. Therefore, more robust alternatives were introduced, utilizing hue or PCA to adaptively select a color for the overlay, based on the tissue characteristics. Additionally, visualization along the temporal dimension of color and fluorescence data acquired in real-time was proposed.

The problem can be generalized to the representation of an n-dimensional dataset in the RGB color space. Herein, we assumed a single fluorescence measurement that is superimposed on a corresponding color image. Such a projection onto a lower dimensional space is inherently lossy; however, the results indicate that the adaptive methods can yield an improved average color contrast. Given the wide range of biological images considered, future work should study the performance of the presented methods on a bigger representative dataset or for individual fields of application. Furthermore, the performance evaluation could be conducted using questionnaires to physicians instead of the contrast formula employed herein.

As an extension to the presented cases, measurements might be taken with multiple fluorochromes or with just a single visible wavelength for orientation. Modified versions of the current algorithms for novel schemes need to be developed to provide even more flexibility under such a wide range of conditions. One possible approach could be the utilization of an overlay color that varies pixel-wise or within the image region to account for images with a greater color variation.

2.2 System adaptation for endoscopy and laparoscopy[3]

Molecular imaging for guidance in ovarian cancer surgery has been performed with a lens-based system [5], a predecessor to the once described in Section 2.1. Similarly, surgical guidance

[3]Text and images from this section have been published in Refs. [12], [25] and [23].

in colorectal cancer surgery would require the detection of color and fluorescence images and video during endoscopy. Acquisition of color reflectance and fluorescence information through a single imaging channel can be facilitated by using a filter wheel as demonstrated in [26], however such a setup measures the two channels sequentially, thus limiting the frame-rate and reducing the clinical utility of the approach. Instead, methods that can detect simultaneously color and fluorescent signals offer improved utility, for example endoscopes utilizing dichroic beam-splitters to separate NIR and color images [27]. However, the systems developed so far for endoscopic fluorescence imaging are either not adapted to clinical devices or cannot provide simultaneous color and high-sensitivity fluorescence measurements at video frame-rates. Clinical propagation of fluorescence molecular imaging will require the development of video-rate acquisition of color and fluorescence images, their processing and real-time display capability, which is essential for fast and easy surveillance during endoscopy. Video rate color and fluorescence imaging can give the physician important feedback during biopsies and surgical intervention.
However, a current limitation is that while most clinical endoscopes have been developed for color video in the visible, it is unclear if they are optimally suited for operation with fluorescence molecular probes developed for operation in the near-infrared. The use of NIR wavelengths for fluorescence molecular imaging provides important advantages as it allows the seamless separation of conventional color measurements and fluorescence measurements. Furthermore it offers operation under reduced tissue auto-fluorescence compared to the visible and allows for the detection of deep-seated signals, typically at depths of 5-10 mm. Thus, as a first step to the adaptation of the intra-operative imaging system to endoscopic use, the optical attenuation of various clinical scopes was characterized.

2.2.1 Characterization of clinical scopes

An important concern regarding the translation of the intra-operative imaging system for usage in endoscopy and laparoscopy was the suitability of commercial devices for imaging in the near infrared (NIR) spectral region. Clinical scopes are designed to yield high quality images in the visible range, hence in this section the transmission properties of scopes considered for fluorescence imaging in different fields was characterized.
A 750 nm CW laser (BWF2-750-0, B&W Tek, Newark, US-DE) with a maximum output

power of 300 mW was coupled via a multimode fiber (4.5 mm core diameter, Leoni FiberOptics, Neuhaus-Schierschnitz, Germany) into the scope. The transmitted power was measured after the multimodal fiber and after the endoscope with a laser power meter. From the ratio of these values the attenuation of NIR light was determined in order to confirm the device's capability to operate with fluorescent probes. The instruments examined were a rigid laparoscope (26901-00, Dufner Instruments, Tuttlingen, Germany), a flexible cholangioscope (13700 CKS, Karl Storz, Tuttlingen, Germany), a WS1705/1 laparoscope (Olympus, Tokyo, Japan), a GIF-XQ20 gastroscope (Olympus), the SpyGlass fiber optic probe (Boston Scientific, Natick, US-MA) and a BF-P30 bronchoscope (Olympus). The selection comprises clinical grade fiber scopes and laparoscopes, which are routinely employed in white-light endoscopy of the gastrointestinal tract, the biliary and pancreatic ducts and other minimally invasive procedures.

Endoscope Model	**NIR Attenuation** [dB]
Dufner 26901-00 laparoscope	6.2
Karl Storz 13700 CKS cholangioscope	9.0
Olympus WS1705/1 laparoscope	4.5
Olympus BF-P30 bronchoscope	8.4
Olympus GIF-XQ20	7.3
Boston Scientific SpyGlass	10.0

Table 2.1: Comparison of near infrared light attenuation in dB of different endoscopes. Measurements were taken for CW laser light with a wavelength of 750 nm.

Table 2.1 shows the attenuation in dB of various clinical laparoscopes and endoscopes. The different scopes attenuate the light by up to 10 dB, where the major losses are considered to happen due to inefficient coupling and not due to transmission losses within the scope. Given that most clinical scopes are optimized for operation in the visible, there is a characteristic lack of technical specifications for NIR operation. While the results indicate that a suitable performance can be achieved using clinical scopes, there is some room for improvement. Attenuation differences between devices were found, reaching up to an order of magnitude for one-way transmission. This indicates up to two-orders of magnitude signal loss for collecting NIR fluorescence images and video, a suboptimal performance. Instead, color and NIR-dedicated scopes should be developed and employed in the design of future clinical

systems.

2.2.2 Adaptation for laparoscopy

2.2.2.1 Setup

The imaging setup was designed to offer video-rate simultaneous color and NIR fluorescence acquisition during laparoscopic interventions and is shown in Figure 2.9. The system employed the 10 mm diameter laparoscope (26901-00, Dufner Instruments, Tuttlingen, Germany) with an aperture angle of 45 degrees and 310 mm length. White light illumination for color imaging was provided by a 250 W halogen lamp (KL-2500 LCD, Schott AG, Mainz, Germany) while the fluorescence excitation was provided by a 750 nm CW laser diode (BWF2-750-0, B&W Tek, Newark, US-DE) with a maximum power of 300 mW. A shortpass filter (E700SP-2P, Chroma, Rockingham, US-VT) was placed in front of the white light source to minimize cross-talk of excitation light into the NIR channel. Both sources were coupled into a multimode bifurcated fiber bundle (Leoni FiberOptics, Neuhaus-Schierschnitz, Germany) connected to the light guide of the laparoscope. The bundle was manufactured from 80 μm fibers to connect one white light source and up to three laser outputs to the scope. A focusing adaptor was used to connect the laparoscope to the imaging system described in Section 2.1.

2.2.2.2 System characterization

Optical characterization The system's spatial resolution was determined by a standard three-bar resolving test target (USAF-1951, NT53-714, Edmund Optics, Barrington, US-NJ). It consists of groups of three vertical and horizontal bars that make it possible to determine the contrast transfer function (CTF) from the contrast equation.

$$\mathrm{CTF}\,(f) = \frac{I_{max}(f) - I_{min}(f)}{I_{max}(f) + I_{min}(f)} \tag{2.15}$$

Thereby I_{max} and I_{min} are the maximum and minimum intensity values of neighboring bar groups and f denotes the spatial frequency of line pairs ($\frac{\mathrm{lines}}{\mathrm{mm}}$) for a group element. An element's spatial frequency is standardized to be $2^{-\frac{1}{6}}$ times the frequency of the adjacent higher element. Color images of the target were taken at the laparoscopic working distance of 2 cm.

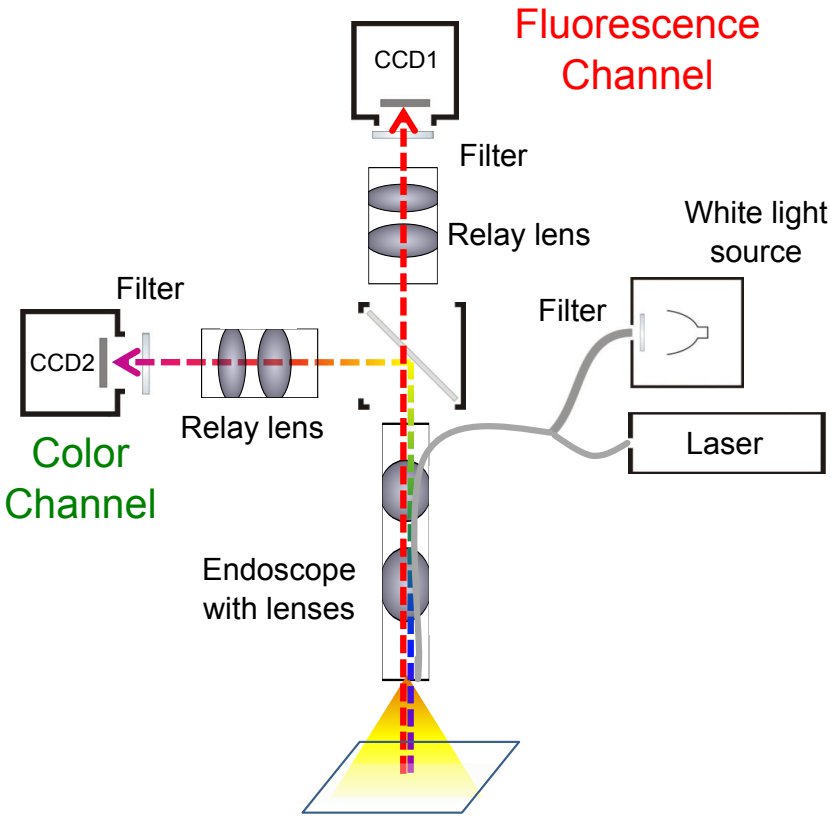

Figure 2.9: Schematic of the intra-operative imaging system developed for laparoscopy. White light and laser are connected via a multimodal fiber to the laparoscope and used to illuminate the field of view. A dichroic beamsplitter separates the reflectance image into a color and near-infrared (NIR) fluorescence component, which are relayed to two CCD sensors.

The spatial resolution for the laparoscopic imaging system, as determined from the USAF 1951 test target, is displayed in Figure 2.10. By measuring the maximum and minimum pixel values within a bar group the contrast transfer function for the groups corresponding spatial frequency f was calculated. This yields the transverse and lateral CTF for the color channel. The focusing of point objects through a circular aperture creates a diffraction pattern called the Airy disk. The Rayleigh criterion defines resolution as the distance between two objects, where one object's diffraction pattern minimum overlaps with the others' maximum. This corresponds to a contrast of 26.4 % between the maximum and minimum intensity values. The resolution was determined by approximating the CTF with a linear regression line and applying the Rayleigh criterion. The transverse resolution was determined to be 49 μm while the lateral resolution was calculated as 54 μm.

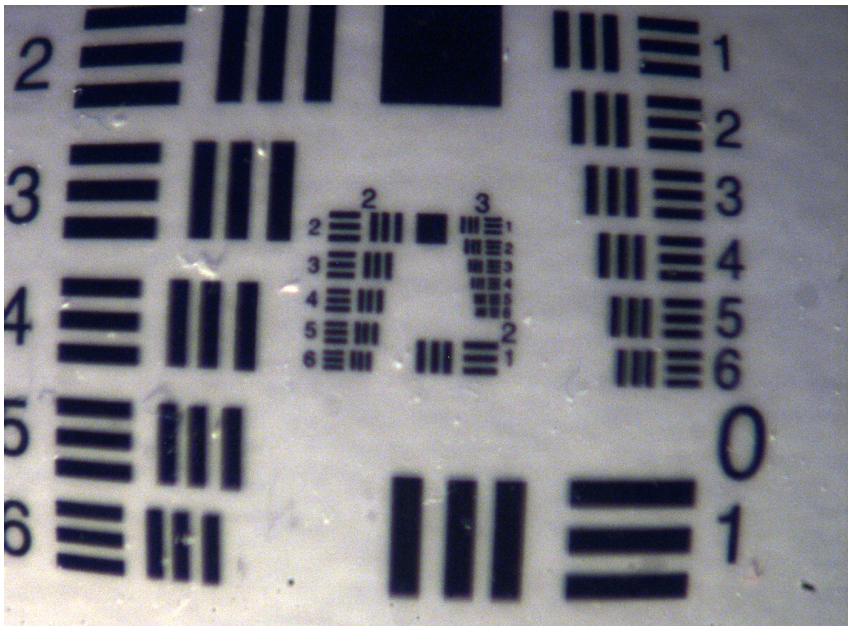

Figure 2.10: Color channel image of USAF 1951 standard resolution target taken with the laparoscopic imaging system under white light illumination.

Sensitivity measurements The minimal detectable fluorochrome concentration was determined by measuring a dilution series of Alexa 750 (Invitrogen, Eugene, US-OR) in phosphate buffered saline (PBS). Starting at 1.56 μM, a total of 17 dilutions were generated. The concentration was halved at each step, thus the final phantom contained 0.02 nM of Alexa

750. A tube with 500 μL of the respective concentration was placed at a distance of 2 cm from the laparoscope tip so that the entire tube is in the field of view. White light and laser illumination were delivered solely through the laparoscope in order to include the attenuation of the laparoscope optics and the multimodal fiber in the measurement. The exposure time was chosen individually for each image in such a way, that at least 60 % of the camera's dynamic range is used. All other acquisition parameters remained constant. After each measurement a control tube containing PBS was measured with the same parameters and in the same position. Image statistics were calculated on a region of interest (ROI) that was selected for each measurement to represent the inside of the tube. The selected ROI corresponded to an active volume of about 40 μL, which contained the amount of 62.5 pmol of fluorochrome for the first phantom and 0.95 fmol for the final one. Dark images were acquired for the respective exposure times and subtracted from the fluorescence and control images. Therein the image average ranged from 390.9 to 392.0 and the standard deviation from 2.25 to 2.35 pixel counts. In accordance with ASTM guidelines [28] the signal-to-noise ratio (SNR) in dB can be calculated as:

$$\mathrm{SNR_{dB}} = 20 \log \left(\frac{\mathrm{S}}{\mathrm{RMSN}} \right) \tag{2.16}$$

Thereby S is the mean signal intensity of the raw fluorescence image within the ROI, while the root-mean-square noise (RMSN) is calculated as the RMS of the control image's ROI. In this way the SNR is normalized for signal variations that are introduced by the PBS, reflections from the tube or inhomogeneous illumination. For a normal signal distribution a confidence level of 95 % is achieved if the signal is two times higher than the noise and a 99.7 % confidence for a signal that is three times higher. On the dB scale these values correspond to 6 dB and 9.5 dB, respectively.

A second experiment was conducted to characterize the imaging performance at video-rate conditions. Thereby three representative concentrations of 500 nM, 50 nM and 5 nM (20 pmol, 2 pmol and 0.2 pmol respectively in 40 μL) were imaged at fluorescence exposure times varying from 60 to 200 ms. The resulting image SNR was calculated as described above.

Seventeen images of the different fluorochrome concentrations as well as the corresponding control images were taken with exposure times ranging from 60 milliseconds to 9.5 seconds. The calculated SNR for the entire series is plotted in Figure 2.11A. As expected, the SNR decreases with the fluorochrome concentration, even though the exposure time for each image

was set to a value that used at least 60 % of the dynamic range in order to avoid underexposure. The measurements were approximated by a linear regression line from which the minimum concentrations that can be detected with 95 % and 99.7 % confidence were determined. For the 9.5 dB criterion the sensitivity limit was calculated as 0.8 nM (32 fmol in the 40 μL volume imaged) while an SNR of 6 dB is achieved for concentrations higher than 0.5 nM (20 fmol in 40 μL). These results correspond well to the visual evaluation of the fluorescence images.

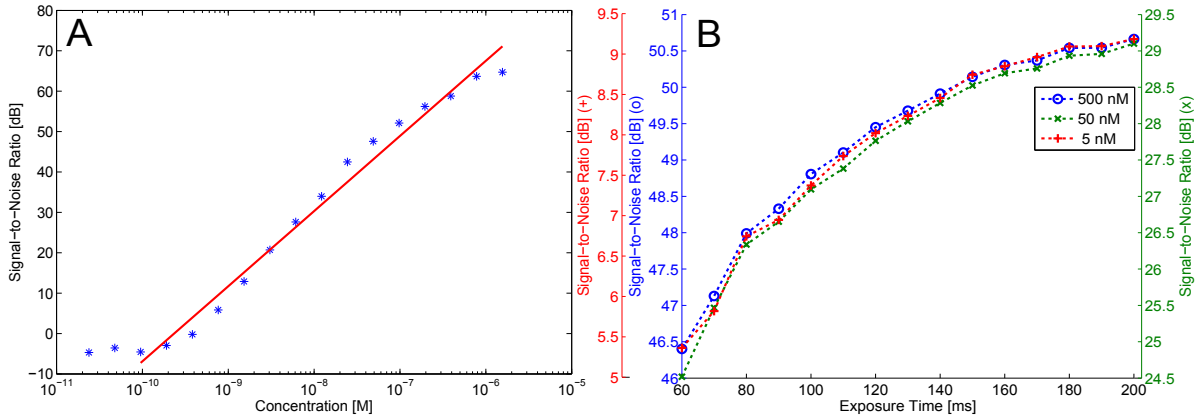

Figure 2.11: A) Graph showing the signal-to-noise ratio (SNR) in dB over AF750 concentration (blue) and calculated regression line (red). B) SNR over fluorescence camera exposure time for concentrations of 500 nM (blue), 50 nM (green), and 5 nM (red).

Figure 2.11B shows the SNR over fluorescence exposure time for concentrations of 500 nM, 50 nM and 5 nM. This is an important measurement to understand the frame rate that can be achieved with the laparoscope, assuming different required sensitivity levels. Over the measured integration times the three concentrations exhibit a similar behavior, with the image quality decreasing more rapidly at low acquisition times. For the two higher concentrations a satisfactory SNR of over 20 dB can be achieved even for exposure times below 100 ms (blue and green scale). The lowest concentration of 5 nM yields an SNR of 7.4 dB at 100 ms exposure (red scale). Hence, increased detection accuracy, e.g. the 9.5 dB criterion used above, can only be achieved when the video frame rate is decreased below 10 fps.

2.2.3 Adaptation for cholangiopancreatoscopy

2.2.3.1 Setup

Simultaneous color and NIR fluorescence imaging was realized by using the mother-daughter technique that is frequently used in cholangioscopy. Thereby, a miniature fiber cholangioscope (Karl Storz, Tuttlingen, Germany) is guided through the working channel of a duodenoscope into the bile or pancreatic duct. White-light and laser illumination is coupled in the cholangioscope through a multimodal fiber (SEDI-ATI Fibres Optiques, Courcouronnes, France), as shown in the schematic of the setup in Figure 2.12. The camera setup and image processing used are described in Section 2.1 while the scope's attenuation was characterized in Section 2.2.1.

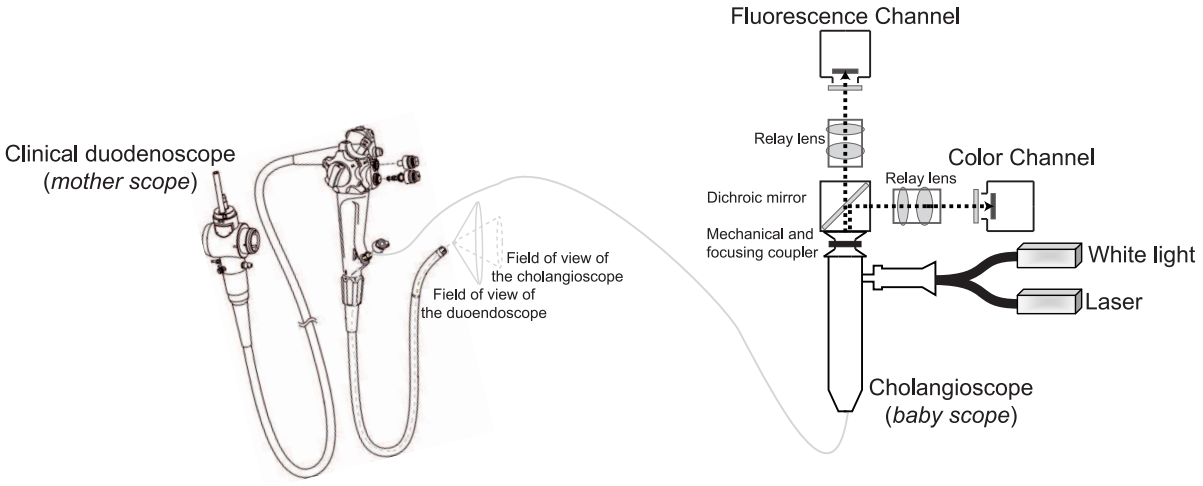

Figure 2.12: Experimental setup for the combined white-light and NIR fluorescence endoscopic imaging. The cholangioscope is guided through a duodenoscope and connected to the imaging system. Illumination is provided by a continuous wave (CW) laser and a white light source that are connected to the scope via a multimodal fiber.

2.2.3.2 System characterization

The resolution of the endoscopic system was examined using the visible wavelength channel and imaging a 1951 United States Air Force resolution target (USAF 1951, NT53-714, Edmund Optics, Barrington, US-NJ). The points of the contrast transfer function (CTF) where obtained employing the Michelson contrast formula [29] that is commonly used for patterns

of the USAF 1951 and defines the contrast as the quotient between the difference and the sum of the maximum and minimum gray values of adjacent line patterns. Photon detection sensitivity is an essential metric in establishing NIR fluorescence at video-rates and providing the physician with immediate feedback in the endoscopy suite during the exploratory procedure. This requirement imposes constraints on the length of the exposure time allowed and thus on the sensitivity that can be attained on a per frame basis. In order to determine the system's sensitivity under typical operating conditions a dilution series of 16 indocyanine green (ICG; Pulsion Medical Systems, Feldkirchen, Germany) phantoms was measured. Each phantom consisted of a varying concentration of ICG dissolved in phosphate buffered saline (PBS), with a total volume of 640 μL. Thereby the initial concentration of 25.2 μM was halved for every subsequent phantom, yielding 0.77 nM concentration for the final phantom. Additionally, a control phantom containing only PBS was measured. The tubes were imaged through the endoscopic system described above at the typical working distance of 1 cm, as it is expected for the clinical application. Video-rate imaging at a frame-rate of 10 fps was performed by setting the fluorescence camera's exposure time to 100 ms. The acquisition parameters remained constant over the measurement series for easy comparison of signal intensities between phantoms. A region of interest (ROI) representing an active volume of about 50 μL was selected for each measurement. The phantom concentrations correspond to an amount ranging from about 1.25 nmol (highest concentration phantom) to 37.5 fmol (lowest concentration phantom) in the active volume. The signal-to-noise ratio (SNR) for a fluorescence measurement was calculated as:

$$\mathrm{SNR_{dB}} = 20 \log \left(\frac{\mathrm{S}}{\mathrm{RMSN}} \right) \tag{2.17}$$

Thereby S is the mean signal intensity in the ROI, while RMSN is the root-mean-square noise of the control image. We defined the detection limit as the concentration where the signal is three times higher than the noise, which corresponds to an SNR of 9.5 dB.
Figure 2.13A) shows a detail from the USAF 1951 resolution target imaged in the system's color channel. The contrast transfer function was determined from the target's horizontal and vertical bar groups and fitted with a linear regression curve. Applying the Rayleigh criterion of 26.4 % contrast it was calculated that features with a dimension of 47.28 μm can be resolved. In Figure 2.13B) the signal-to-noise ratio calculated for the 16 phantoms of the dilution series is shown (dotted line with triangles). As expected, the image quality decreases approximately

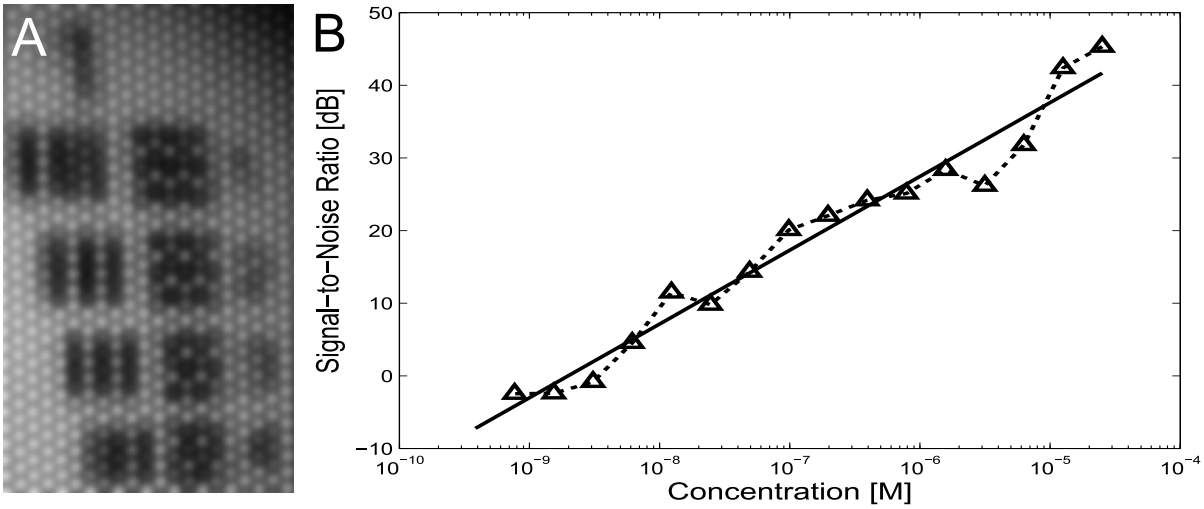

Figure 2.13: A) Detail of the USAF 1951 resolution target image. Applying the Rayleigh criterion, a lateral resolution of 47.28 μm was determined. B) Signal-to-noise ratio over ICG concentration measured from the dilution series at 100 ms exposure time.

linearly with the concentration, reaching the floor of 0 dB in the sub-nanomolar range. The linear regression curve is plotted (solid line), and from it the detection limit of 9.5 dB was calculated to lie at a concentration of 17.3 nM, which equals an amount of 365 fmol in the active volume of 50 μL.

2.2.4 Adaptation for colonoscopy

2.2.4.1 Setup

Wide-field fiber endoscope Initially a fiberscope (GIF-XQ20, Olympus, Center Valley, US-PA) was considered to replace the common objective that was previously shared by the color and fluorescence camera in the imaging system as described in Section 2.1. The fiberscope optically transmits the images through a coherent fiber-optic bundle and is connected via a mechanical and focusing adapter to the camera system. A multi-branched fiber-optic bundle (SEDI-ATI Fibres Optiques, Courcouronnes, France) simultaneously couples white-light illumination (KI-2500 LCD, Schott AG, Mainz, Germany) and fluorescence excitation (BWF2-750-0, B&W Tek, Newark, US-DE) into the illumination port of the endoscope. The multi-branched end of the bundle consists of 4 branches, one terminating in a mechanical ferrule adapted to our white-light source and 3 with SMA connectors. Independent illumination and imaging

channels are particularly suitable since background signal from the autofluorescence of the imaging bundle is prevented [30]. Additional filters are allocated in the light path to assure that the fluorescence and white-reflectance measurements are restricted to the wavebands of interest.

Miniature flexible endoscope The replacement of the videoendoscopes that are routinely used in the clinics nowadays by the previous fiberscope to realize the acquisition of fluorescence images at video-rate induces a significant resolution loss in the color videos, i.e. it impedes normal clinical workflow. In light of this, an alternative implementation mainly consisting of a semi-disposable, coherent imaging bundle that is long and thin enough to be inserted through the accessory channels of routine videocolonoscope is proposed, as suggested by Funovics et al. for shorter working lengths [27]. To satisfy the requirements regarding the number of pixel elements, the field of view, working length and distal diameter, a miniaturized fiberscope (Spy-Glass Direct Visualization Probe, Boston Scientific, Marlborough, US-MA) was considered. The Spyglass is used routinely in cholangiopancreatoscopy, the endoscopic exploration of the biliary and pancreatic ducts utilizing a miniature endoscope [31]. This so called cholangioscope is routed through the working channel of a therapeutic endoscope, which is sufficiently large to accommodate it, an approach dubbed mother-daughter technique. The probe consists of a 6,000 pixel image bundle surrounded by approximately 225 light transmission fibers that cover the coherent bundle as an outer sheath. It has a maximal diameter of 0.9 mm, a working length of 231 cm and includes a lens at the distal tip of the imaging bundle that allows image capture across a 70° field of view. Consequently, its wide field of view and reduced diameter facilitate its employment as the babyscope for fluorescence acquisition in a mother-daughter system where a conventional videocolonosope acts as the mother scope.
The transmission of NIR light of both scopes was previously characterized in Section 2.2.1. With an attenuation of 7.3 dB and 10.0 dB, respectively, both scopes were found to be suitable for the use in near infrared fluorescence imaging applications. Table 2.2 summarizes the technical features of the miniature endoscope by comparison with the fiberscope employed in the suggested endoscopic imaging alternative.
In a like manner to custom developments used by others in fluorescence confocal microscopy [32] and microendoscopy [33, 34], a custom developed zoom system was designed for magnifying the image of the proximal end of the imaging bundle to fill the dimensions of the fluorescence camera sensor. This camera choice was based on the main interest in the easy

Manufacturer Model name	Olympus GIF-XQ20	Boston Scientific SpyGlass Probe
Distal diameter [mm]	9.8	0.77
Accessory channel [mm]	2.8	N/A
Depth of field [mm]	3–100	2–7
Working length [mm]	1025	3000
Angulation	(Up/down) 210/90 (Left/right) 100/100	120/120
Field of view (air)	120°	70°
Picture elements	20000	6000
NIR attenuation [dB]	7.3	10.0

Table 2.2: Technical specifications of the two clinical grade scopes employed in the wide-field, concurrent, video-rate color and NIR fluorescence imaging platform for flexible endoscopy.

and quick characterization of the molecular characteristics of the lesions over large fields of view using targeted fluorescent agents, while the color images would only be used to provide accurate localization and superimposition on the high resolution images from the conventional videoscope. This offers the additional advantage of ease of adaptation between intra-operative and gastrointestinal endoscopy environments, since any required modification of the earlier intra-operative version of the system is accomplished in front of the beamsplitter that separates the two image components. The zoom system is based on an infinity optical microscope design and it consists of a 40x / 0.75 numerical aperture (NA) infinity-corrected objective lens (Olympus) and an achromatic doublet with NIR anti-reflective coating to minimize the reflectivity at the fluorescence emission wavelength (AC254-100-B, Thorlabs, Newton, US-NJ). The appropriate focal length of the lens was selected to achieve a combined magnification of the objective and the lens that maximizes the area of the fiber image on the fluorescence CCD. Mechanical adapters, positioners and supports were used as needed to assure a comfortable and stable use in the endoscopy suite, while combined white-light and laser illumination is similarly provided through the multimodal light guide. For the deployment in the endoscopy suite an additional shortpass filter (e.g. ET700SP, Chroma Technology, Rockingham, US-VT) would need to be placed in the white-light source of the videoendoscope to minimize tissue reflectance at the wavelengths in the range of the emission waveband to enter the fluorescence detection path. Figure 2.14 schematizes and compares the proposed alternatives for wide-field, video-rate, concurrent white-light and NIR fluorescence imaging in flexible endoscopy.

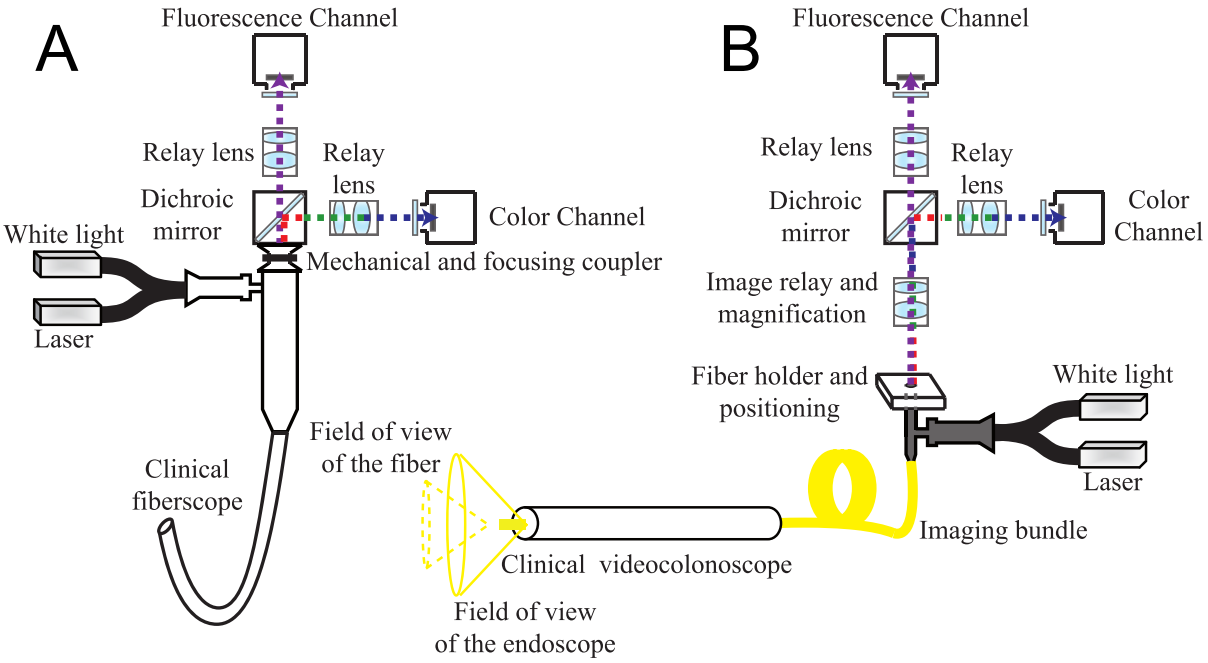

Figure 2.14: Schematic of the two imaging platforms proposed for NIR fluorescence guidance in surveillance colonoscopy. A) shows the adaption of the clinical grade gastrointestinal fiberscope, while the alternative based on the semi-disposable imaging fiber bundle that can be integrated with conventional videocolonoscopes is shown in B).

2.2.4.2 System characterization

Optical characterization The resolution of the endoscopic system was examined in the fluorescence channel to determine the minimum size of identifiable lesions. Because of the geometrical constraints of the endoscopic environment, i.e. epi-illumination and detection geometries, cross-sectional imaging is not possible. Subsequently, only the lateral resolution is characterized. To this aim the different pattern groups in a 1951 United States Air Force resolution target (USAF 1951, NT53-714, Edmund Optics, Barrington, US-NJ) were imaged. The points of the contrast transfer function (CTF) were obtained employing the Michelson contrast formula that is commonly used for patterns as the USAF 1951 and defines the contrast as the quotient between the difference and the sum of the maximum and minimum gray values of adjacent line patterns.

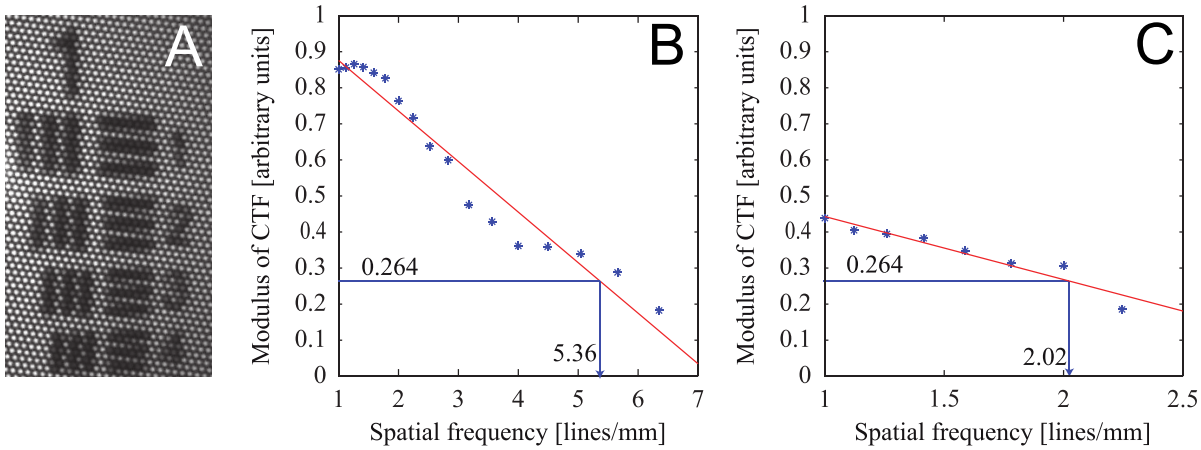

Figure 2.15: A) Detail of the USAF 1951 resolution target image. Contrast transfer functions obtained by determining the specific contrast produced by bar group patterns of various spatial frequencies taken by the endoscopic imaging platforms based on a clinical grade fiberscope (B) and on the miniature cholangioscope (C).

The CTF was determined from images of the USAF 1951 bar groups taken with the proposed endoscopic imaging platforms, as shown in Figure 2.15 (dots). The modulus of the CTF was linearly fitted (solid line), and the line pairs corresponding to a contrast of 26.4%, applying the Rayleigh criterion, were determined to be 5 and 2 $\frac{\text{lp}}{\text{mm}}$ for the clinical grade fiberscope and the miniature cholangioscope, respectively. By taking the half-width between two line pairs, it was determined that features with corresponding dimensions of 100 and 250 μm could be resolved, demonstrating sufficient resolution for small lesion identification. As expected from the number of picture elements, resolution is considerably higher for the fiberscope GIF-XQ20, but this gain in the resolution with respect to the miniature cholangioscope that can be inserted to the accessory channel is obtained at the expense of no high resolution image available for white-light illumination.

Sensitivity measurements In order to determine the system's sensitivity under typical operating conditions in the endoscopy suite and to demonstrate its capability to provide the physician with immediate feedback about the molecular characteristics of the lesions, a dilution series of IRDye 800CW (Li-Cor Biosciences, Lincoln, US-NE) phantoms was measured. Each subsequent phantom consisted of a halved concentration of the tracer labeling dissolved in phosphate buffered saline (PBS), with a total volume of 2 ml and initial concentrations of

0.20 μM and 1.70 μM, for the implementations based on the fiberscope and the reusable probe, respectively. The dilutions were contained in a black cylinder with a diameter of 2.54 cm and a depth of 1.27 cm, which translates to a sample thickness of 3.95 mm. Additionally, a control phantom of the same dimensions and containing only PBS was measured. The phantoms were imaged through the designed implementations at a working distance of 1 cm. Video-rate imaging at a frame-rate of 10 fps was performed by setting the fluorescence camera's exposure time to 100 ms. The acquisition parameters remained constant over the measurement series for easy comparison of signal intensities between phantoms. A region of interest (ROI) representing an active volume of about 8 μL was selected for each measurement. The phantom concentrations correspond to an amount ranging from 1.60 pmol to 3.32 fmol and 13.60 pmol and 26.56 fmol in the active volume for the fiberscope and the reusable probe, respectively. The SNR for a fluorescence measurement was calculated as:

$$\mathrm{SNR_{dB}} = 20 \log \left(\frac{\mathrm{S}}{\mathrm{RMSN}} \right) \tag{2.18}$$

Thereby S is the mean signal intensity in the ROI, while RMSN is the root-mean-square noise of the control image. We defined the detection limit as the concentration where the signal is three times higher than the noise, which corresponds to an SNR of 9.5 dB.

The signal-to-noise ratio was calculated for the dilution series of IRDye 800CW, as shown in Figure 2.16 for the two fiberendoscopes (dots). As expected the image quality decreases approximately linearly with the concentration. From the regression line (solid), the detection limit of 9.5 dB was calculated to lie at concentrations of 5.97 nM and 23.11 nM, which equal amounts of 47.79 fmol and 0.18 pmol in the active volume of about 8 μL, corresponding to the selected ROI with an optical thickness of approximately 3.95 mm. The fiberscope with larger diameter and better image resolution also achieves higher sensitivity. Reported detection limits that still satisfy video-rate imaging constraints are attained through the employment of an imaging fiber bundle to relay the fluorescence images to a highly sensitive sensor module, and are expected to surpass detection capabilities of videoscopes for fluorescence imaging in the NIR, given the current state of the art CCD chips on the tip of the flexible scopes. The determined detection limits mainly represent a characteristic of the imaging setup. However, bearing in mind the previously determined tumor uptakes [35], these sensitivities are expected to be sufficient for detecting small lesions. Moreover, no significant detriment is expected to occur when imaging in tissue, since fluorescence imaging is performed in the NIR range,

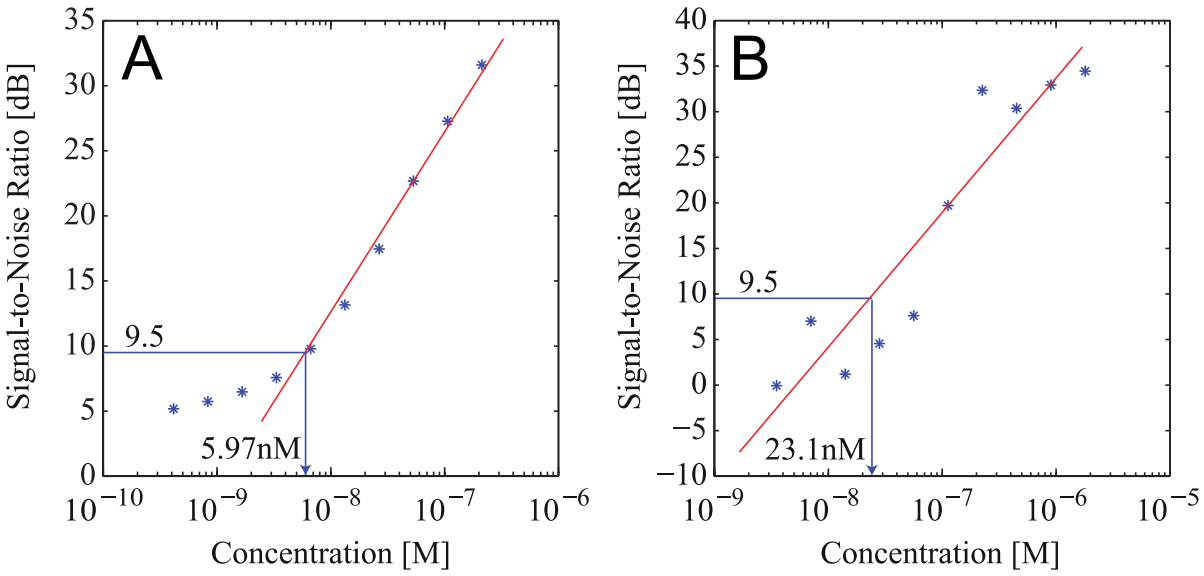

Figure 2.16: Signal-to-noise ratio over concentration measured from the CW800 dilution series by the endoscopic imaging platforms based on a clinical grade fiberscope (A) and on the miniature cholangioscope (B), both under video-rate constraints (100 ms exposure time).

where influence from tissue attenuation is minimized compared to the visible range. Yet, further improvement in the detection limit could be achieved coupling additional excitation to the presently unused SMA branches of the multimodal illumination bundle.

2.2.5 Discussion

Laparoscopy Section 2.2.2 presented the development of a system that facilitates video-rate color and near-infrared fluorescence-based molecular imaging through a human laparoscope. A dual-optical-path approach was combined with highly sensitive fluorescence detection and GPU-based processing to facilitate video-rate sensing and rendering of low fluorescence signals and computationally intensive image processing tasks. Due to the computational ability of the GPU, images acquired from different cameras and CCD chips could be synchronized, aligned, scaled and superimposed in real-time. The fluorescence distribution was then visualized in pseudo-color on a composite image. However different visualization schemes may be implemented, including synchronized visualization of raw color and fluorescence video. Another reason to employ the GPU as a co-processor was the possibility to implement sophisticated fluorescence correction schemes in the future that reduce the influence of tissue optical prop-

erties on the signal.
Alternative methods for combining and optimizing white-light illumination and fluorescence excitation into the illumination port of the laparoscope could be considered. These could be coupled into a single guide light using conventional optics, specifically aspheric lenses for collimation followed by posterior refocusing. Alternatively, and in order to maintain the robustness of the bifurcated fiber approach considered here, fiber-optic or light cones as well as tapers could be incorporated to maximize the efficiency in the light coupling between guides of different cross-sections.
Furthermore, the attained sensitivity was examined as a function of frame-rate and fluorochrome concentration under standard operation parameters. Despite the scope attenuation, concentrations in the sub-nanomolar range could be detected, owing to the use of cooled EMCCD camera detection with high NIR quantum efficiency to facilitate highly sensitive fluorescence measurements. Concentrations in the sub-nanomolar range however require slowing down the video frame rate at rates below 10 fps for high SNR detection. In an ideal case, increasing signal collection times would increase the SNR by the square root of the time allowed, however the results indicate that the improvement gradually decreases for higher exposure times, showing that other factors such as readout electronics, gain and quantization noise also play a role. System characterization further yielded 50 μm lateral and transverse resolution. Obviously, the resolution strongly depends on the imaging distance and the laparoscope's optical path, thus different values would result for different endoscopic devices.

Cholangiopancreatoscopy In Secion 2.2.3 a fiberoptic baby-scope was guided through the working channel of a duodenoscope (mother scope) and connected to a high sensitivity video-rate camera system. Characterization of the setup's spatial resolution yielded approximately 50 μm, which matches the resolution of the human eye and is generally sufficient to detect small foci of tumor and discriminate the margins. Using a cooled EMCCD camera, fluorophore amounts as small as 365 femptomoles of an organic fluorescent dye could be detected, an unprecedented metric in endoscopic fluorescence imaging. This highly sensitive performance further enabled operation at video frame-rates of over 10 fps. An additional constraint to the maximum attained sensitivity is imposed by the maximum laser illumination power that has to abide by the tissue exposure limits established by the International Commission of Non-Ionizing Radiation Protection [36]. It is important to highlight here that the reported sensitivity limit is subject to the light intensity and detection sensitivity constraints, which ultimately determine

the minimum amount detected and the maximum frame rate performance achieved in in vivo endoscopy for clinical applications.

Colonoscopy Two alternative approaches to realize fluorescence colonoscopy and confront the insufficient sensitivity in the NIR of routine videoendoscopes were proposed and characterized in Section 2.2.4. Both endoscopic imaging platforms consist in the adaptation of a gastrointestinal fiberscope and a miniature fiber-optic probe that is used in white-light endoscopy of the biliary and pancreatic ducts, respectively, for compatibility with the previously developed camera system for concurrent white-light and fluorescence acquisition. The employment of clinical grade fiberscopes to relay the fluorescence images to a more sensitive sensor module is advantageous for two reasons. First, sensitivity requirements for contrast agent visualization at microdosing administration are satisfied. Thereby, the incapability of current clinical wide-field endoscopic technologies to provide information about the expression of specific disease-associated biomarkers to guide targeted treatment selection is confronted. Based on the results from the resolution and sensitivity characterization studies, the approach would also provide a great asset for aiding in the detection of lesions that are currently easily missed in clinical endoscopy. These are protruding lesions of sizes in the order of several millimeters and flat lesions that, in spite of being sometimes as large as up to 1 cm, remain imperceptible because of the lack of contrast to the surrounding tissue. Both types of lesions are at least one order of magnitude above the size of the features that can be resolved with the proposed endoscopic imaging platforms and are expected to accumulate large amounts of the contrast agent. Secondly, their CE certification facilitates the approval for use in humans of the imaging platforms, thereby alleviating the risk for demonstrating the potential of targeted NIR fluorescence guidance. The adapted gastrointestinal fiberscope, because of its larger diameter, achieves better illumination, field of view, image resolution and sensitivity. These advantages are, however, attained at the expense of no high-definition images available for the white-light illumination either. The miniature cholangioscope was selected for the second imaging implementation because it is the only clinical grade fiberscope that is long and thin enough to be guided through the accessory channel of a conventional videocolonoscope. The detection limit determined in the characterization stage and the levels of detected fluorescence signals suggest sufficient sensitivity for in vivo imaging. Consequently, the approach might be adequate for providing a red-flag lesion detection strategy over a wide-field of view. Since at typical operating distances, the power densities corresponding to the maximum laser output

at the distal tip of the endoscopes are below the limits established by the International Commission of Non-Ionizing Radiation Protection [36], further improvement in the detection limit could be achieved, either by coupling additional light sources to the remaining branches of the bifurcated fiber or by improving the coupling efficiency of the mechanical connections.

Bibliography

[1] G. Themelis, J. Yoo, K. Soh, R. Schulz, and V. Ntziachristos, "Real-time intraoperative fluorescence imaging system using light-absorption correction", *Journal of Biomedical Optics*, vol. 14, no. 6, p. 064 012, 2009.

[2] A. Sarantopoulos, "Accurate quantification and detailed bio-distribution with planar multispectral fluorescence imaging", PhD Thesis, Technische Universität München, 2012.

[3] L. M. A. Crane, G. Themelis, R. G. Pleijhuis, N. J. Harlaar, A. Sarantopoulos, H. J. G. Arts, A. G. J. van der Zee, V. Ntziachristos, and G. M. van Dam, "Intraoperative multispectral fluorescence imaging for the detection of the sentinel lymph node in cervical cancer: a novel concept", *Molecular Imaging and Biology*, vol. 13, no. 5, pp. 1043–1049, 2011.

[4] L. M. A. Crane, G. Themelis, H. J. G. Arts, K. T. Buddingh, A. H. Brouwers, V. Ntziachristos, G. M. van Dam, and A. G. J. van der Zee, "Intraoperative near-infrared fluorescence imaging for sentinel lymph node detection in vulvar cancer: first clinical results", *Gynecologic Oncology*, vol. 120, no. 2, pp. 291–295, 2011.

[5] G. M. van Dam, G. Themelis, L. M. A. Crane, N. J. Harlaar, R. G. Pleijhuis, W. Kelder, A. Sarantopoulos, J. S. de Jong, H. J. G. Arts, A. G. J. van der Zee, B. Joost, P. S. Low, and V. Ntziachristos, "Intraoperative tumor-specific fluorescence imaging in ovarian cancer by folate receptor-α targeting: first in-human results", *Nature Medicine*, vol. 17, no. 10, pp. 1315–1319, 2011.

[6] F. Chen, D. A. Koufaty, and X. Zhang, "Understanding intrinsic characteristics and system implications of flash memory based solid state drives", in *Proceedings of the eleventh international joint conference on Measurement and modeling of computer systems*, ACM, 2009, pp. 181–192.

[7] J. Nickolls and W. Dally, "The GPU computing era", *Micro, IEEE*, vol. 30, no. 2, pp. 56–69, 2010.

[8] M. Trajković and M. Hedley, "Fast corner detection", *Image and vision computing*, vol. 16, no. 2, pp. 75–87, 1998.

[9] A. Goshtasby, "Piecewise linear mapping functions for image registration", *Pattern Recognition*, vol. 19, no. 6, pp. 459–466, 1986.

[10] J. Glatz, P. Symvoulidis, P. B. Garcia-Allende, and V. Ntziachristos, "Robust overlay schemes for the fusion of fluorescence and color channels in biological imaging", *Journal of Biomedical Optics*, vol. 19, no. 4, p. 040 501, 2014.

[11] J. S. D. Mieog, S. L. Troyan, M. Hutteman, K. J. Donohoe, J. R. van der Vorst, A. Stockdale, G.-J. Liefers, H. S. Choi, S. L. Gibbs-Strauss, H. Putter, *et al.*, "Toward optimization of imaging system and lymphatic tracer for near-infrared fluorescent sentinel lymph node mapping in breast cancer", *Annals of surgical oncology*, vol. 18, no. 9, pp. 2483–2491, 2011.

[12] J. Glatz, J. Varga, P. B. Garcia-Allende, M. Koch, F. R. Greten, and V. Ntziachristos, "Concurrent video-rate color and near-infrared fluorescence laparoscopy", *Journal of Biomedical Optics*, vol. 18, no. 10, p. 101 302, 2013.

[13] T. Porter and T. Duff, "Compositing digital images", in *ACM Siggraph Computer Graphics*, ACM, vol. 18, 1984, pp. 253–259.

[14] R. C. Gonzalez and R. E. Woods, *Digital Image Processing*, 3rd Edition. Upper Saddle River, NJ: Prentice Hall, 2007.

[15] M. Sezgin and B. Sankur, "Survey over image thresholding techniques and quantitative performance evaluation", *Journal of Electronic Imaging*, vol. 13, no. 1, pp. 146–168, 2004.

[16] J. Ghaye, M. A. Kamat, L. Corbino-Giunta, P. Silacci, G. Vergeres, G. Micheli, and S. Carrara, "Image thresholding techniques for localization of sub-resolution fluorescent biomarkers", *Cytometry Part A*, vol. 83, no. 11, pp. 1001–1016, 2013.

[17] N. Otsu, "A threshold selection method from gray-level histograms", *IEEE Transactions on Systems, Man and Cybernetics*, vol. 9, no. 1, pp. 62–66, 1979.

[18] M. R. Luo, G. Cui, and B. Rigg, "The development of the CIE 2000 colour-difference formula: CIEDE2000", *Color Research & Application*, vol. 26, no. 5, pp. 340–350, 2001.

[19] L. Shapiro and G. C. Stockman, *Computer Vision*. Upper Saddle River, New Jersey: Prentice Hall, 2001.

[20] I. T. Jolliffe, *Principal Component Analysis*, 2nd edition. New York: Springer, 2005.

[21] A. Sarantopoulos, G. Themelis, and V. Ntziachristos, "Imaging the bio-distribution of fluorescent probes using multispectral epi-illumination cryoslicing imaging", *Molecular Imaging and Biology*, vol. 13, no. 5, pp. 874–885, 2011.

[22] J. Stritzker, L. Kirscher, M. Scadeng, N. C. Deliolanis, S. Morscher, P. Symvoulidis, K. Schaefer, Q. Zhang, L. Buckel, M. Hess, *et al.*, "Vaccinia virus-mediated melanin production allows mr and optoacoustic deep tissue imaging and laser-induced thermotherapy of cancer", *Proceedings of the National Academy of Sciences*, vol. 110, no. 9, pp. 3316–3320, 2013.

[23] P. B. Garcia-Allende, J. Glatz, M. Koch, J. J. Tjalma, E. Hartmans, A. G. Terwisscha van Scheltinga, P. Symvoulidis, G. M. van Dam, W. B. Nagengast, and V. Ntziachristos, "Towards clinically translatable nir fluorescence molecular guidance for colonoscopy", *Biomedical Optics Express*, vol. 5, no. 1, pp. 78–92, 2014.

[24] M. Koch, J. Glatz, V. Ermolayev, E. G. de Vries, G. M. van Dam, K.-H. Englmeier, and V. Ntziachristos, "Video-rate optical flow corrected intraoperative functional fluorescence imaging", *Journal of Biomedical Optics*, vol. 19, no. 4, p. 046 012, 2014.

[25] J. Glatz, P. B. Garcia-Allende, V. Becker, M. Koch, A. Meining, and V. Ntziachristos, "Near-infrared fluorescence cholangiopancreatoscopy: initial clinical feasibility results", *Gastrointestinal Endoscopy*, vol. 79, pp. 664–668, 2014.

[26] Z. Liu, S. J. Miller, B. P. Joshi, and T. D. Wang, "In vivo targeting of colonic dysplasia on fluorescence endoscopy with near-infrared octapeptide", *Gut*, 2012.

[27] M. A. Funovics, R. Weissleder, and U. Mahmood, "Catheter-based in vivo imaging of enzyme activity and gene expression: feasibility study in mice", *Radiology*, vol. 231, no. 3, pp. 659–666, 2004.

[28] *Standard test method for limit of detection of fluorescence of quinine sulfate in solution*, E579-04, ASTM Standard, ASTM International, 2009.

[29] A. A. Michelson, *Studies in optics*. Dover Publications, 1995.

[30] J. A. Udovich, N. D. Kirkpatrick, A. Kano, A. Tanbakuchi, U. Utzinger, and A. F. Gmitro, "Spectral background and transmission characteristics of fiber optic imaging bundles", *Applied Optics*, vol. 47, no. 25, pp. 4560–4568, 2008.

[31] R. J. Shah, D. G. Adler, J. D. Conway, D. L. Diehl, F. A. Farraye, S. V. Kantsevoy, R. Kwon, P. Mamula, S. Rodriguez, L. M. Wong Kee Song, *et al.*, "Cholangiopancreatoscopy", *Gastrointestinal Endoscopy*, vol. 68, no. 3, pp. 411–421, 2008.

[32] A. R. Rouse, A. Kano, J. A. Udovich, S. M. Kroto, and A. F. Gmitro, "Design and demonstration of a miniature catheter for a confocal microendoscope", *Applied Optics*, vol. 43, no. 31, pp. 5763–5771, 2004.

[33] T. J. Muldoon, M. C. Pierce, D. L. Nida, M. D. Williams, A. Gillenwater, and R. Richards-Kortum, "Subcellular-resolution molecular imaging within living tissue by fiber microendoscopy", *Optics Express*, vol. 15, no. 25, p. 16 413, 2007.

[34] D. P. Noonan, D. S. Elson, G. P. Mylonas, A. Darzi, and G.-Z. Yang, "Laser-induced fluorescence and reflected white light imaging for robot-assisted mis", *Biomedical Engineering, IEEE Transactions on*, vol. 56, no. 3, pp. 889–892, 2009.

[35] A. G. T. van Scheltinga, G. M. van Dam, W. B. Nagengast, V. Ntziachristos, H. Hollema, J. L. Herek, C. P. Schröder, J. G. Kosterink, M. N. Lub-de Hoog, and E. G. de Vries, "Intraoperative near-infrared fluorescence tumor imaging with vascular endothelial growth factor and human epidermal growth factor receptor 2 targeting antibodies", *Journal of Nuclear Medicine*, vol. 52, no. 11, pp. 1778–1785, 2011.

[36] International Commission on Non-Ionizing Radiation Protection, "Revision of the guidelines on limits of exposure to laser radiation of wavelengths between 400 nm and 1.4 μm", *Health Physics*, vol. 79, no. 4, pp. 431–440, 2000.

Chapter 3

Image processing methods

3.1 General purpose computation on graphics processing unit

A key point of software development is that the software and its algorithms should be adapted to the underlying hardware. There have been quite significant changes regarding computer hardware in the last decade, moving from sequential to parallel architectures. While previously parallel computing has been only a niche technology for specialized high-performance demands and supercomputer clusters, it has become much more prominent due to two major developments in the last decade. The first one is the introduction of multi-core microprocessors while the other fascinating trend is the usage of the graphics card as a co-processor for general purpose computations.
This section will discuss the development of the different architectures and look back on the history of parallel computing.

3.1.1 From single-core to multi-core CPUs

Traditionally, microprocessors have been based on a single central processing unit (CPU). In accordance with Moore's law [1] their performance has grown for multiple decades, supplying ever increasing computing power to both private and scientific users. Software developers could rely on this development to continuously improve the performance of their software by providing a new generation of chips on which the program would simply execute much faster.

Obviously, each step forward gave rise to a set of new ideas and applications that demanded even faster hardware.
This trend, however, has significantly slowed down in recent years. For the continuous performance growth it was necessary to increase the clock-frequency and squeeze more transistors onto the chip area. Inevitably, problems with power consumption, heat dissipation and the manufacturing of nanometer scale parts arose. It turned out that technological limitations eventually slowed the continuous growth. For this reason development took a novel path towards chip models that now feature multiple processor cores instead of the classical single-core architecture [2]. Dual- and quad-core processors are well established in the desktop and notebook market and are even starting to penetrate the field of mobile phones [3]. This paradigm shift towards multi-core architectures for the central processing unit was dubbed the concurrency revolution by Sutter and Larus in 2005 [4].
Of course such a fundamental change in design must be supported by appropriate new programming concepts. The traditional way of executing a list of operations one after the other was well suited to single-core CPUs and benefited from every speed-up achieved by new technology. In order to make use of additional parallel cores the developers were required to come up with concepts where operations could be executed in parallel, thus keeping all of the computational units busy all the time [5].

3.1.2 From specialized to programmable GPUs

The graphics processing unit (GPU) was developed as a very specialized piece of hardware, dedicated to perform fast calculations required for 2D or 3D rendering. The main concept was to offload these computations from the CPU, thus freeing it for other tasks and allowing a higher performance due to parallelization on the GPU. The GPU executes a set of predefined instructions or stages on the input data provided by the host CPU. This set of rendering methods is referred to as the graphics pipeline [6].
The first task in the graphics pipeline is commonly performed by the CPU and consists of parameterizing the data into vertices - corner coordinates of geometric primitives such as triangles. As a next step, appropriate geometric operations are performed on the vertices, accounting for the 3D viewpoint, lighting conditions, camera transformations and the clipping of points that are outside of the visible area. Finally, in the rasterization step the actual color values are assigned to the rendered image by interpolating between the vertices or applying

textures from memory. The result of this process chain is then displayed on the monitor.
This fixed-function graphics pipeline has been both a strength and a weakness of early GPU models. It was possible to adapt both hard- and software to this pipeline, thus providing optimizations for each pipeline stage with a new generation of graphics cards. On the other hand this design made the GPUs not programmable, the developer was merely able to configure certain parameters in the pipeline and employ an application programming interface (API) to use GPU resources in his programs. Among the most commonly used APIs were Microsoft's DirectX™and OpenGL®, an open, platform-independent media library that is being developed by the Khronos Group. These APIs turned out to not be well suited for scientific computations. They were still restricted and inflexible compared to other programming approaches, which made their handling difficult for an inexperienced developer. A further disadvantage was the lack of double precision floating point support which is required in some specialized scientific applications.
With the unrelenting demand and drive of the video game industry this architecture soon turned out to be limiting and not flexible enough to satisfy more sophisticated needs. Some intermediate steps towards a programmable environment were taken by GPU manufacturers and new API versions, but a major milestone was the release of the compute unified device architecture (CUDA) framework by Nvidia in 2007 [7]. The further discussion will focus on CUDA as it is the technology employed in this work.
The introduction of CUDA constitutes a major rework of the Nvidia GPU architecture, adapting not only the software layer to the needs of programmability, but also the hardware [8]. Among the cornerstones of the new architecture are the ability of the user to directly access GPU memory and the abandonment of the fixed-function graphics pipeline in favour of a design featuring parallel programmable threads. Figure 3.1 shows the basic design of a CUDA GPU. The graphics card receives a set of instructions from the main CPU side (the host) and those are translated and distributed to the parallel thread units by the thread execution manager. A number of parallel threads then execute these instruction concurrently, where each block of threads uses its own dedicated data and texture cache. Furthermore, the device comes with a global dynamic random access memory (DRAM) that can be used by all threads for data exchange and storage.
While this step eased the task of video game developers and provided them with new options it also opened up a wide range of possibilities for completely different applications. The additional freedom and flexibility made it possible to use the GPU not only as a specialized device

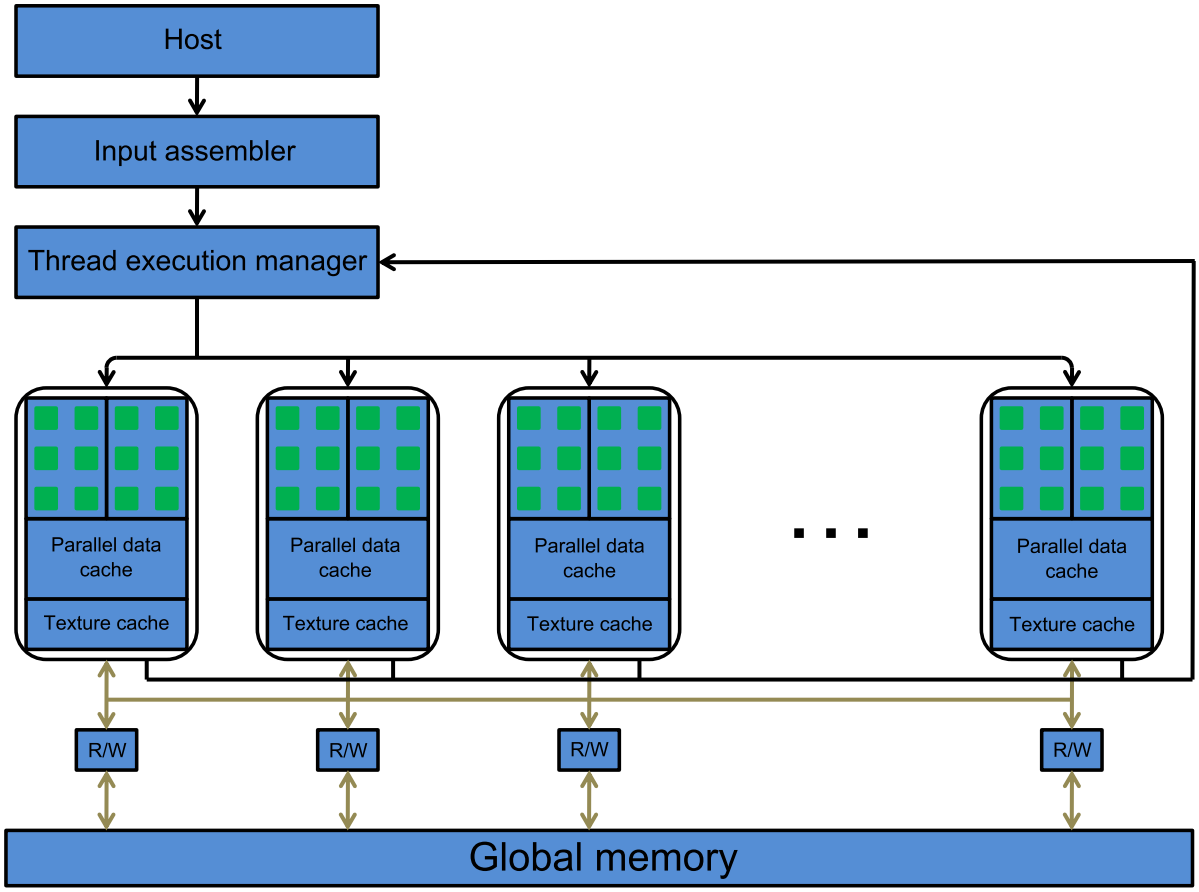

Figure 3.1: Architecture of a CUDA GPU.

for graphics operations but as a co-processor for general computations, a practise that was named general purpose computation on graphics processing unit (GPGPU) [9]. Other manufacturers have brought forward similar concepts, such as AMD with their FireStream cards, which are also intended to be used as floating point co-processors for scientific calculations. Both CUDA and FireStream however have the disadvantage of being hardware bound: any algorithm developed on them will require the presence of a suitable GPU by the respective manufacturer. A platform-independent framework to allow GPU computing is offered by the OpenCL® standard (Khronos Group), which has been adopted by both Nvidia and AMD.
These advances have transformed the GPU from a dedicated graphics processor to a co-processor that supports extensive calculations for a wide range of applications, a development that must be noted as an important turning point of processing technology. The introduction

of the GPU as a general purpose computation unit has opened a new design trajectory. One route is the traditional multi-core design of several CPU chips as outlined in Section 3.1.1 as a continuation of the single-core processors. But the massively parallel architecture of the GPU, with many slower but concurrent processing units, has successfully established itself as a promising alternative [10].
Currently hybrid-systems, such as the one presented in this work, where tasks are distributed between the CPU and the GPU are a frequently used setup. In it, computations that are inherently parallel, such as independent operations on all pixels of an image or all elements of a matrix, are performed on the GPU. The remaining tasks, that are better suited for sequential processing, are then distributed to the CPU. However, this model bears a certain overhead due to memory transfers between the devices.
In the future these two design trajectories might be fused into a single-device architecture that is a hybrid between multi-core and massively parallel processors. Those are referred to as many-core systems and are currently being developed for example by Intel's research program Tera-Scale [11, 12].

3.1.3 CUDA GPU architecture

In order to understand the advantages and disadvantages of these two design trajectories one needs to look at their underlying hardware architecture. Figure 3.2 compares the basic resource distribution of a CPU and a GPU chip [7].
It becomes clear why the GPU is such a powerful parallel computing device: it simply devotes more chip space and thus more transistors to the execution of arithmetic and logical operations. A contemporary GPU like Nvidia's GeForce GTX 560 Ti possesses a total of 384 CUDA cores clocked at a frequency of 1.6 GHz. Even though a modern CPU such as the Intel Core i7-990X runs at two times the frequency and has six cores it is clear, that the parallel architecture of a GPU achieves a significantly higher number of floating point operations per second (FLOPS). On the other hand this means that less resources are available for memory management and control functions. As a consequence the memory structure is quite different: while the GPU is also equipped with a global DRAM memory it has a much smaller cached memory. Furthermore the cached memory blocks are usually localized, meaning that they are only accessible to a subset of the cores. Since reading and writing operations are performed much faster on the localized cache memory (shared memory) it makes sense for a developer

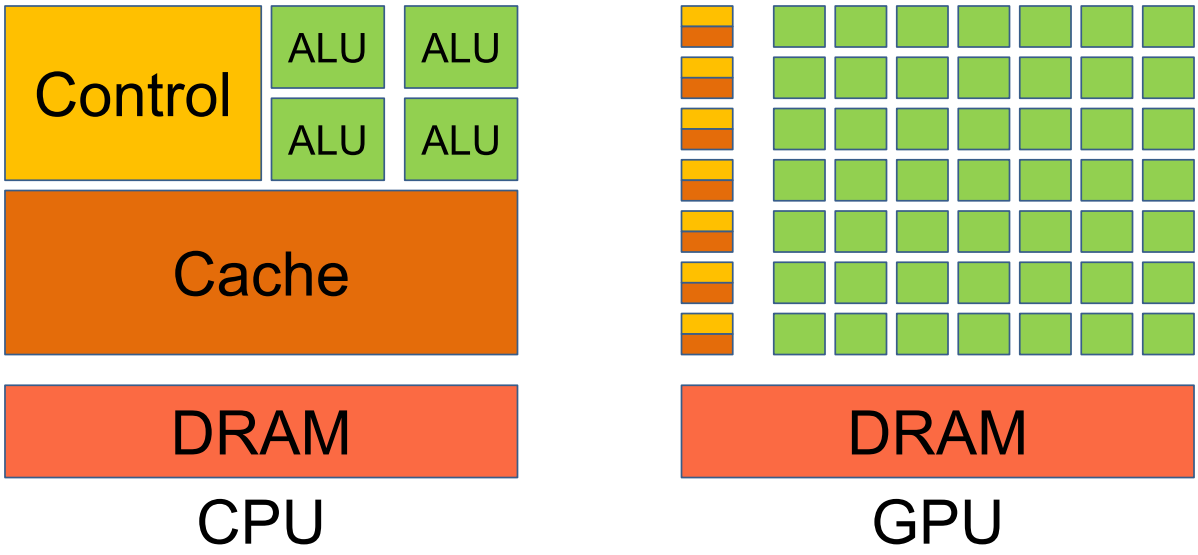

Figure 3.2: Comparison of CPU and GPU resource allocation.

to avoid slow DRAM accesses in favor of using the shared memory.

A key concept of CUDA devices is the single-instruction multiple-thread execution model [13]. Thereby, commands are organized and scheduled into groups of 32 parallel threads called warps. This concept facilitates the highly parallel execution of instructions. An arithmetic operation, the so-called kernel, can be applied to 32 image pixels by calling a warp with that instruction. However, this model, like GPU programming in general, requires a certain amount of optimization. Warp divergence, the case when the parallel kernels of a warp do not perform the same instruction, is a serious performance issue. This can happen on image edges or when the instruction set contains conditional statements. Commonly employed techniques are padding the memory to multiples of 32 units and ensuring coordinated memory access, which is called coalescing. Figure 3.3 shows an example of coalesced and non-coalesced memory access within a warp. The access scheme shown in Fig. 3.3A is optimized for the single-instruction multiple-thread execution model and yields optimal performance, while the scheme of Fig. 3.3B performs significantly slower due to threads T_3 and T_4 breaking the coordinated access and thread T_{25} not performing an operation at all. For a simple kernel consisting of a read, increment and write operation an average access time of 356 μs was reported for the coalesced case and 3494 μs for the non-coalesced scheme [14].

These and various other programming and optimization techniques required to effectively use the GPU resources were documented for example by Kirk [8] and Sanders [15].

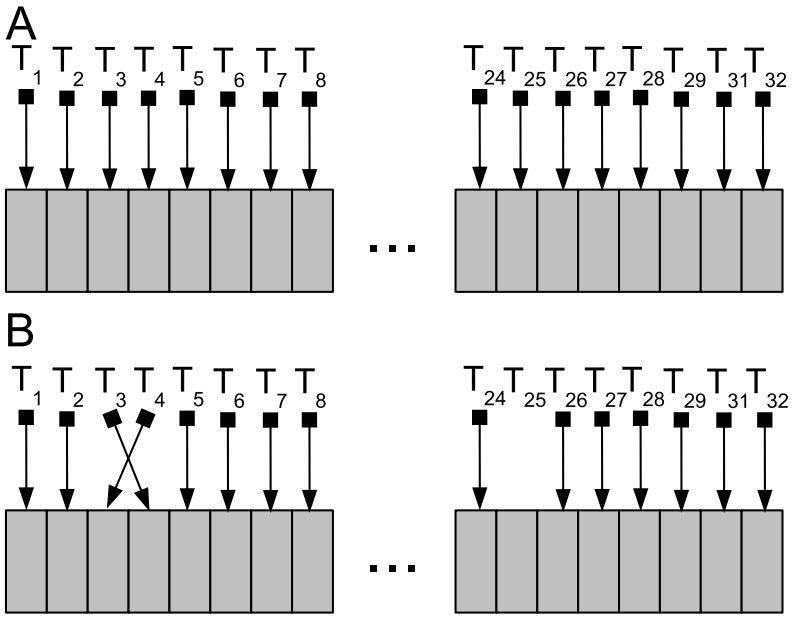

Figure 3.3: A) Example of a coalesced memory access where 32 threads read from neighboring memory blocks in a coordinated operation. B) Non-coalesced access where threads T_3 and T_4 break the coordinated access and thread T_{25} does not participate.

On a hybrid architecture, consisting of a host CPU and a GPU, such considerations play an important role. With the release of a series of GPUs based on the Fermi GF100 architecture [16, 17] some decisive improvements were introduced. Fermi GPUs offer faster double precision performance, concurrent kernel execution, improved atomic operations and support for error-correcting code (ECC). Importantly, a transparent L1 and L2 cache hierarchy was introduced and the shared memory was significantly enlarged [18]. Based on the new architecture, enhanced performance for standard arithmetic operations has been achieved [19, 20] and guidelines for tuning techniques have been developed to better exploit the new architecture's possibilities [21, 22]. Nickolls et al. [23] reported substantial speedups of up to 137$\times$ for GPU enhanced applications in a number of different fields. Notably, iterative image reconstruction in computed tomography was accelerated by a factor of 130 [24] and a similar improvement was also reported for an advanced image processing operation like contour detection [25].
With such achievements in mind authors have proclaimed "The GPU computing era" [23], however some challenges remain to bridge the gap between GPGPU and the conventional, widespread computing on CPUs. First, GPUs posses relatively small amounts of DRAM, commonly below 4 GB. Second, their memory can only be accessed via the system memory and

is thus not directly available to input/output (I/O) devices, a factor that limits performance and makes GPU less attractive for I/O device manufacturers. Third, despite some impressive speedups that have been realized on parallel architectures, the performance remains limited by the sequential portion of the program, an argument known as Amdahl's law [26]. Finally, current GPUs have not been designed to be employed and programmed in easily scalable multisocket systems like CPUs, where multiple chips operate on one board [18].

3.1.4 Implementation example: Demosaicking

The aforementioned GPU programming techniques are illustrated in this section on the color demosaicking implementation that is part of the intra-operative system software discussed in Section 2.1.

3.1.4.1 Demosaicking

Images in today's commercial digital cameras are usually acquired by a single charge-coupled device (CCD) sensor. Color images are recorded by placing a color filter array (CFA) on top of the sensor. Consequently, a single CCD pixel measures the incoming light solely in the limited spectral band of its overlaid filter. The most frequently used CFA arrangement was introduced and patented by Bryce Bayer [27]. It consists of 4×4 pixel blocks overlaid with two green, one red and one blue filters. The green channel is sampled at a higher rate to account for the fact, that the human eye is most sensitive to luminance in that region, while less sensor space is devoted to the chrominance components red and blue. This can be seen as a precursor to the chrominance subsampling approach that is widely established in video encoding today. However, various other filter arrangements as well as different methods for color image acquisition exist [28].
Figure 3.4A shows the commercially widespread RGGB Bayer pattern configuration, that was also employed by the color cameras used in this work, while Figure 3.4B displays how the spectral components are filtered to yield subsampled channels. A color image at the original, full resolution is obtained by interpolating the missing pixel information for all color planes. This process is referred to as demosaicking, and the unprocessed, raw data of the camera is hence named the mosaicked image.

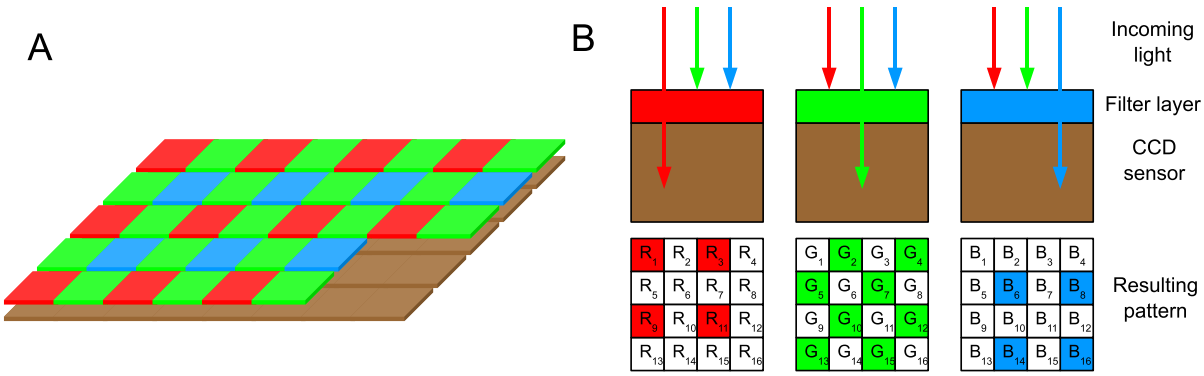

Figure 3.4: A) Configuration of the popular RGGB Bayer pattern. B) Schematic of the filtering of incoming light on the CCD sensor and the resulting pattern.

3.1.4.2 Demosaicking by optimal linear filtering

The simplest demosaicking algorithms use bilinear interpolation to calculate the missing color values from the measured ones. For the configuration shown in Figure 3.4B the red pixel R_6 was not measured, since a blue filter was placed over its position. Yet it can be interpolated as:

$$R_6 = \frac{1}{4}(R_1 + R_3 + R_9 + R_{11})$$

Bilinear interpolation is simple, computationally fast and can serve as a baseline for the evaluation of more advanced algorithms, however it generates visible artifacts along high-frequency components such as edges [29, 30]. Various more refined algorithms have been proposed and evaluated to reduce interpolation artifacts [31–33].

Herein the linear method published by Malvar et. al [34] was implemented in the CUDA framework and integrated into the intra-operative image processing pipeline previously discussed in Section 2.1.4. They solved for the optimal 5×5 filter kernel coefficients assuming correlation between neighboring raw pixel values of different colors, resulting in a gradient-corrected bilinear interpolation. This algorithm was preferred over other sequential or frequency-domain methods because a bilinear kernel filtering efficiently exploits the GPU's parallel architecture, and is easy to implement and optimize. The optimization techniques and speed gains reported for an implementation of this demosaicking approach in the 3D graphics API OpenGL [35] served as an additional incentive.

The filter coefficients for the interpolation of all possible pixel-location combinations as proposed by Malvar et al. [34] are displayed in Figure 3.5. It is important to note that among

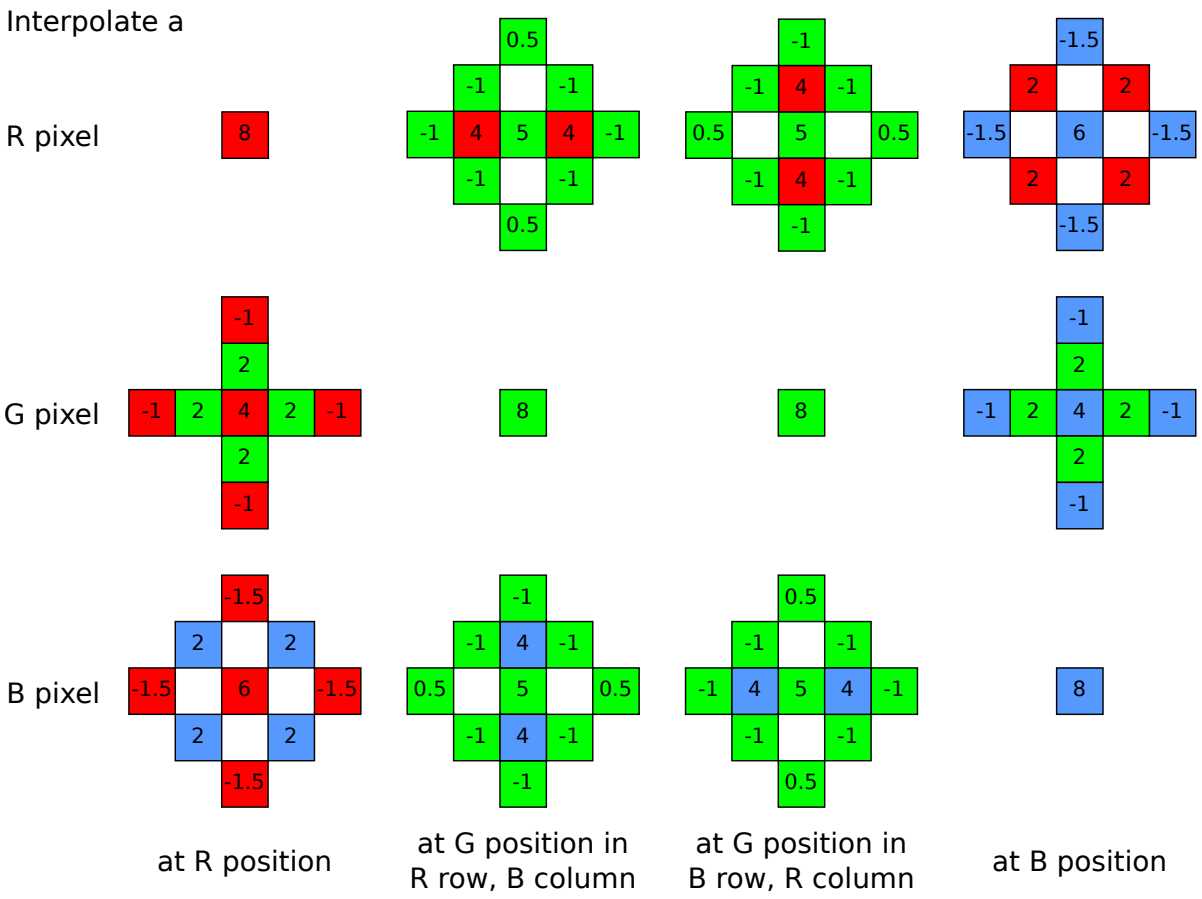

Figure 3.5: Filter coefficients for optimal 5×5 linear demosaicking. Normalized kernels are obtained by dividing the displayed values by 8.

the twelve arrangements four trivial identities and eight pairs of identical, shifted filters are contained, meaning that only five different kernels are eventually applied to the mosaicked data pixel neighborhood.

3.1.4.3 Unoptimized implementation

The straightforward pseudo-code implementation of the described algorithm is shown in Code 3.1. It shows the basic principle of hybrid CPU-GPU programming, where data is copied from the host (CPU) side to the device (GPU) and processed there by parallel threads.

```
// CPU (host) side function
void Demosaicking (int raw[m][n], int rgb[3][m][n])
{
    // Process the image in 16x16 blocks
    dim3 threadsPerBlock(16,16);
    // Create the appropriate number of blocks for the image size and
       the three output colors
    dim3 numBlocks(x/16, y/16, 3);
    // Copy the raw data to GPU global memory
    MemCopyHostToDevice(gpu_raw, raw);
    // Call the parallel GPU kernels. One kernel processes a single RGB
       pixel.
    gpu_kernel_demosaick<<<numBlocks,threadsPerBlock>>>(gpu_raw, gpu_rgb);
    // Copy the result back from the GPU to main computer memory
    MemCopyDeviceToHost(gpu_rgb, rgb);
}
// GPU kernel function to process one output pixel
__global__ void gpu_kernel_demosaick (int gpu_raw[m][n], gpu_rgb[3][m][n])
{
    // Horizontal position of the current kernel
    int x = 16 * blockNumber.x + threadNumber.x;
    // Vertical position of the current kernel
    int y = 16 * blockNumber.y + threadNumber.y;
    // Output color of the current kernel
    int col;
    // Get the 5 x 5 filter coefficients for the current position
    int coeffs[5][5] = GetCoeffsAtPosition(x, y, col);
```

```
    res = 0;
27  // Do the filtering
    for (int i=0; i<5; i++)
29  {
        for(int j=0; j<5; j++)
31      {
            res = res + coeffs[i][j] * gpu_raw[x-2+i][y-2+j];
33      }
    }
35  // Write result to demosaicked image
    gpu_rgb[col][x][y] = res;
37 }
```

Code 3.1: Pseudo-code of a possible GPU demosaicking implementation, where memory usage is not optimized.

It can be seen that this demosaicking implementation is easily parallelizable as every device kernel thread, a call of the GPU-side function gpu_kernel_demosaick, processes an output pixel independently from all the others. However, the memory usage in the above example is not optimal. Line 32 reads the 5×5 vicinity of the current position from GPU global memory. This memory space is accessible to all threads, yet read and write operations on it are extremely slow compared to shared memory, that is only locally accessible to individual thread blocks.

3.1.4.4 Implementation using optimized memory access

Since Code 3.1 performs multiple reads of every raw data pixel a natural optimization approach would be to read every pixel just once into the shared memory of a 16×16 thread block and perform the other read operations there. The necessary pseudo-code modifications of the GPU kernel to realize this optimization are shown in Code 3.2.

```
// GPU kernel function to process one output pixel
2 __global__ void gpu_kernel_demosaick (int gpu_raw[m][n], gpu_rgb[3][m][n])
{
4   // Horizontal position of the current kernel
    int x = 16 * blockNumber.x + threadNumber.x;
6   // Vertical position of the current kernel
```

```
    int y = 16 * blockNumber.y + threadNumber.y;
8   // Output color of the current kernel
    int col = threadNumber.z;
10  // Get the 5 x 5 filter coefficients for the current position
    int coeffs[5][5] = GetCoeffsAtPosition(x, y, col);
12  res = 0;
    // Use shared memory for faster read operations
14  __device__ __shared__ int rawBlock[20][20];
    // Every kernel reads one pixel to shared memory
16  rawBlock[threadNumber.x+2][threadNumber.y+2] = gpu_raw[x][y];
    // Handle 2 pixel apron of shared memory
18  HandleApron(...);
    // Do the filtering
20  for (int i=0; i<5; i++)
    {
22      for(int j=0; j<5; j++)
        {
24          res = res + coeffs[i][j] * ↪
                ↩ rawBlock[threadNumber.x+i][threadNumber.y+j];
        }
26  }
    // Write result to demosaicked image
28  gpu_rgb[col][x][y] = res;
}
```

Code 3.2: Pseudo-code of the GPU demosaicking kernel, where localized shared memory is used for optimized access performance.

The read operation in line 24 is now performed on the faster shared memory. The shared memory block int rawBlock[20][20] is loaded in line 16, with every kernel thread loading only a single pixel, thus ensuring coalesced access and no idle threads. An apron of 2 pixels on every side of the sub-block is required by the kernels. Loading this apron is not elaborated in Code 3.2 (line 18), but is still an important part of the memory optimization. It should be noted that using a block size of 20×20 where all threads load the shared memory and only the inner subset performs the filtering operation would not be a good solution since numerous kernels are inactive during the GPU function call. In the current implementation loading the inner block and the apron is distributed among the kernels associated with different output pixel colors.

3.1.4.5 Performance evaluation

The performance gain attained by hybrid computing for the demosaicking post-processing step was measured by comparing implementations in different programming languages and environments. The linear filtering algorithm was realized in CPU-only implementations in MATLAB (The MathWorks, Natick, MA, USA) and C/C++ as well as in a hybrid CPU/GPU environment using C/C++ and CUDA.

Demosaicking Implementation (Programming Language)	**Average Processing Time** (1.3 MPixel Image) [ms]
MATLAB	42160
C/C++	339
Hybrid C/C++ and CUDA	10

Table 3.3: Average computation times measured for implementations of the demosaicking in MATLAB, C/C++ and CUDA.

Table 3.3 shows the computation times obtained by averaging over 100 executions on sample images of 1.3 MPixel size. The results indicate, that a significant performance gain can be attained solely by using parallel hybrid computing in image processing. This becomes crucial for applications that require real-time or video-rate image processing, such as those being employed in the medical field. Detailed profiling reveals that a significant amount of the hybrid implementation processing time is required for copying data between host and GPU memory. This fact becomes an important bottleneck in most high-throughput GPU computations and further exemplifies the need for direct I/O access to the graphics card's memory.

It is important to note that the measured times do not represent an absolute lower limit for this algorithm but are rather based on straight-forward implementations. Optimization routines for image filtering with separable kernels are well known [36] and could be applied to all three codes to reduce processing times. MATLAB functions that already include such routines were not used to maintain comparability. Furthermore, MATLAB has already started to support parallel computing in newer versions, thus also harvesting performance gains from hybrid CPU/GPU computing [37]. This is perhaps another hint that parallel computing will play an increasingly important role in the future of various scientific fields.

3.2 Space-variant deconvolution

As discussed in Chapter 1, fluorescence imaging is a potent method to study molecular functions in tissue. It allows for non-contact imaging of in vivo cellular processes such as gene expression, protein function and cellular signaling [38], as well as the visualization of malignant tissue alterations [39]. The emergence of fluorescence molecular imaging as a means to enhance human vision in clinical applications such as surgery and endoscopy strengthens the need for accurate fluorescence images in turbid media. Surgical and endoscopic guidance, based on fluorescent agents that report on disease biochemistry using fluorescence emission, has received considerable attention in recent years. Both the induction of tissue autofluorescence [40] and the systemic administration of fluorescent probes with biomarker specificity [41, 42] have been successfully applied in clinical studies for the identification and demarcation of cancerous tissue.

The progress in developing agents has not been however matched by a corresponding drive for delivering high-end imaging systems. Typically the novelty in the systems developed is limited to the number of wavelengths that can be acquired multispectrally or the sensitivity of the camera employed. However, there are fundamental limitations on the accuracy of such systems imposed by the physics of photon propagation. The measured images are degraded by light scattering, resulting in a loss of both quantitative information about the marker concentration and spatial distortions.

Light-tissue interaction, as well as previous attempts to correct its effects, were discussed in Section 1.4.1. Herein, a method designed to operate in vivo while offering adaptive ability to account for tissue heterogeneity is presented. The diffuse nature of a fluorescence signal from within biological tissue was characterized as the convolution of the true fluorophore distribution with a space-variant fluorescence point spread function (FPSF). A space-variant deconvolution scheme was developed, which estimates the FPSF from spatial characteristics of spectral measurements and retrieves the fluorescence distribution within a turbid medium.

3.2.1 Methods

3.2.1.1 Theory

Space-variant convolution Convolution is a mathematical operation that is being used for a variety of applications in signal processing [43, 44], computer vision [45] and image

processing [46, 47]. The convolution of two functions $f(t)$ and $g(t)$ is defined as an integral transform:

$$(f * g)(t) = \int_{-\infty}^{+\infty} f(t-\tau)\, g(\tau)\, d\tau \tag{3.1}$$

Digital images are typically represented as a discrete two-dimensional array $I[x][y]$, when the convolution with a constant kernel $K[u][v]$ can be written as a sum.

$$(I * K)[x][y] = \sum_u \sum_v I[x-u][y-v]K[u][v] \tag{3.2}$$

Therein $I[x][y]$ is the image evaluated at pixel coordinates x and y, while K is the 2D convolution kernel. Various image processing steps can be performed utilizing constant kernels of certain shapes, for example edge detection, sharpening and blurring [48]. Consequently, deconvolution, the inversion of Equation (3.2), has been used for the deblurring of images in fields such as microscopy [49, 50] and astronomy [51, 52]. Thereby image blur is modeled as the convolution of the sharp image with a system-specific kernel, named the point spread function (PSF). In many cases the PSF is not known and cannot be easily measured. Hence, blind deconvolution has been developed [53, 54] to estimate both the PSF and the sharp image from the blurred measurement.

However, situations where the PSF changes with the image location require an extended correction scheme. Spatially variant blurs occur in various cases [55], e.g. astronomical adaptive optics imagery [56], in motion blur of multiple objects [57], as well as for collimator blurring in SPECT imaging [58]. It has been confirmed through simulations [59] and experiments [60, 61] that in general the blurring kernel should be modeled with a spatial dependency. For a space-variant image blur the convolution operation can be written as:

$$(I * K)[x][y] = \sum_u \sum_v I[x-u][y-v]K[u][v](x,y) \tag{3.3}$$

In contrast to Equation (3.2), the PSF value varies not only with the kernel image coordinates (u, v) but also with the image position (x, y), yielding a pointwise linear transformation. Various methods have been proposed to model space-variant kernels with reasonable computational complexity [62, 63], such as parametric models of the space-variant blur [64], tensor products [65], wavelet domain approximation [66] or piecewise space invariant convolutions [67, 68]. Spatially adaptive methods, in contrast to the conventional use of deblurring to

correct for degradations introduced by the imaging system, can also be employed the correct for properties of the sample itself [69–71].
Herein the space-variant deconvolution framework was adapted for the enhancement of diffuse fluorescence imaging, developing a novel method to correct for diffusive effects introduced by the sample properties. A space-invariant approach is insufficient to correct for optical diffusion caused by scattering in fluorescence imaging. Primarily, the diffuse signal measured from fluorescent molecules is influenced by tissue optical properties [72, 73], and thus is varying spatially in the sample.

Space-variant deconvolution The spatially variant kernel $K[u][v](x, y)$ can be interpreted as a fluorescence point spread function (FPSF) that describes the propagation of a fluorescent point emission from the image point (x, y). The FPSF was modeled as the product of a gaussian kernel with standard deviation $\sigma[x][y]$ and the anisotropy map $A[x][y]$. The latter accounts for the spatial variance of diffusion properties and is of the same size as the image I. We assumed that the diffusion anisotropy is separable from the standard deviation and only dependent on the kernel pixel location relative to the image. The space variant kernel can then be written as

$$K[u][v](x, y) = A[x][y]G(\sigma[x][y])[u][v] \tag{3.4}$$

where $G(\sigma)[u][v]$ is a 2D gaussian kernel with standard deviation σ. The distribution's full width at half maximum (FWHM) is related to the standard deviation as follows:

$$\mathrm{FWHM} = 2\sigma\sqrt{2\ln 2} \tag{3.5}$$

The kernels at all locations (x, y) were normalized so that

$$\sum_u \sum_v K[u][v](x, y) = 1 \tag{3.6}$$

The diffusion correction is performed by a modified Richardson-Lucy algorithm. This algorithm is widely used in microscopy [74] and astronomy [75] and is also employed as the basis of blind deconvolution [76]. It calculates the maximum-likelihood solution to a deconvolution

problem by performing a series of iterative convolutions [77].

$$I_{n+1} = I_n \left(\frac{C}{I_n * K} \right) * \overline{K} \tag{3.7}$$

Thereby I_n is the reconstruction at iteration step n, C is the observed blurred image, K is the convolution kernel and $\overline{K}$ is the kernel flipped along both coordinate axes. Equation (3.7) was extended to yield a space-variant deconvolution by replacing the two space-invariant convolution operations with the space-variant model described above, and applied with 75 iteration steps. For computational reasons the standard deviation map $\sigma[x][y]$ was discretized for the deconvolution iterations and interpolated afterwards. The modified Richardson-Lucy algorithm was implemented in MATLAB (The MathWorks, Natick, US-MA) in Fourier space, where the flipped kernel $\overline{K}$ simplifies to the complex conjugate.

3.2.1.2 Phantom experiment

A series of 15 tissue mimicking liquid phantoms was measured to characterize the effects of varying optical properties, both on the color reflectance images and the fluorescence point spread function. Phantoms contained a spherical inclusion of 500 nM Alexa Fluor 750 at a depth of about 5 mm below the surface. A solution containing $10.9 \frac{mg}{ml}$ titanium oxide (TiO_2) powder (Sigma-Aldrich, St. Louis, US-MO) was prepared to match the scattering properties of Intralipid 20% (Sigma-Aldrich) [78], which is frequently used for tissue mimicking phantoms [79]. The TiO_2 solution was added in concentrations of 0.4%, 0.8%, 1.2%, 1.6% and 2.0% respectively. Bovine blood was used as an absorber in concentrations of 1.0%, 2.0% and 4.0%, respectively. The range of both components was chosen to correspond to tissue optical properties documented in the literature [80].

The true shape of the fluorescent inclusion was measured from a phantom devoid of blood and TiO_2. The FPSF of every phantom was determined as the deconvolution of its imaged fluorescence and the gold standard inclusion. Additionally, a phantom consisting solely of the titanium solution was measured to serve as a reflectance standard. The samples were imaged using the intraoperative system as described in Section 2.1.

3.2.1.3 Tissue experiments

The proposed method was validated on images acquired from ongoing studies to provide realistic cases. In the first dataset, the fluorescent probe scVEGF-CY5.5 (SibTech, Brookfield, US-CT) was employed to target a subcutaneous 4T1 breast cancer allograft. The second dataset stems from a study to evaluate an experimental lipid-bound indocyanine green (ICG) based probe (Lipo-ICG) inside a subcutaneous 4T1 tumor. The third dataset investigated the bio-distribution of AlexaFluor750 (Molecular Probes, Eugene, US-OR) in excised mouse lungs after probe application using an inhalation technique [81].
Fluorescence and color measurements were taking using an imaging-cryoslicer system [82]. This system has an almost identical geometry with the clinical intra-operative and endoscopic setup, taking planar color and epi-fluorescence images of tissue blocks using sequential filter wheel acquisition. A major advantage of the cryoslicing system is the possibility to preserve the surface sample slice for validation and histology. Such thin tissue slices are virtually turbidity-free, since their thickness of about 20μm is significantly smaller than the mean free path. Makroscopic epi-fluorescence images of such preserved slices provided a gold standard validation of the fluorophore distribution to evaluate the deconvolution algorithm performance.

3.2.2 Results

3.2.2.1 Phantom experiment

The fluorescence point spread function (FPSF) was calculated for every phantom as the space-invariant deconvolution of the measured fluorescence image with the gold standard fluorescence distribution and is shown in Figure 3.6. The images indicate, that the obtained fluorescence point spread function is predominantly dependent on the scattering, which is denoted by the titanium concentration, and mostly invariant against changes of absorption. This is in agreement with the expectation that scattering is dominant over absorption effects in the NIR range for tissue.
Intensity profiles through the fluorophore location were calculated and averaged over all angles. The FWHM was measured from the resulting curves. Figure 3.7A shows the FWHM over the reduced scattering coefficient $\mu_s^{'}$, which was computed from the utilized $\mathrm{TiO_2}$ concentration. A linear fit of the measurement points was done and confirmed the high correlation of the kernel FWHM to the scattering ($\mathrm{R}^2 = 0.95$). Considering that $\mu_s^{'}$ is generally not known

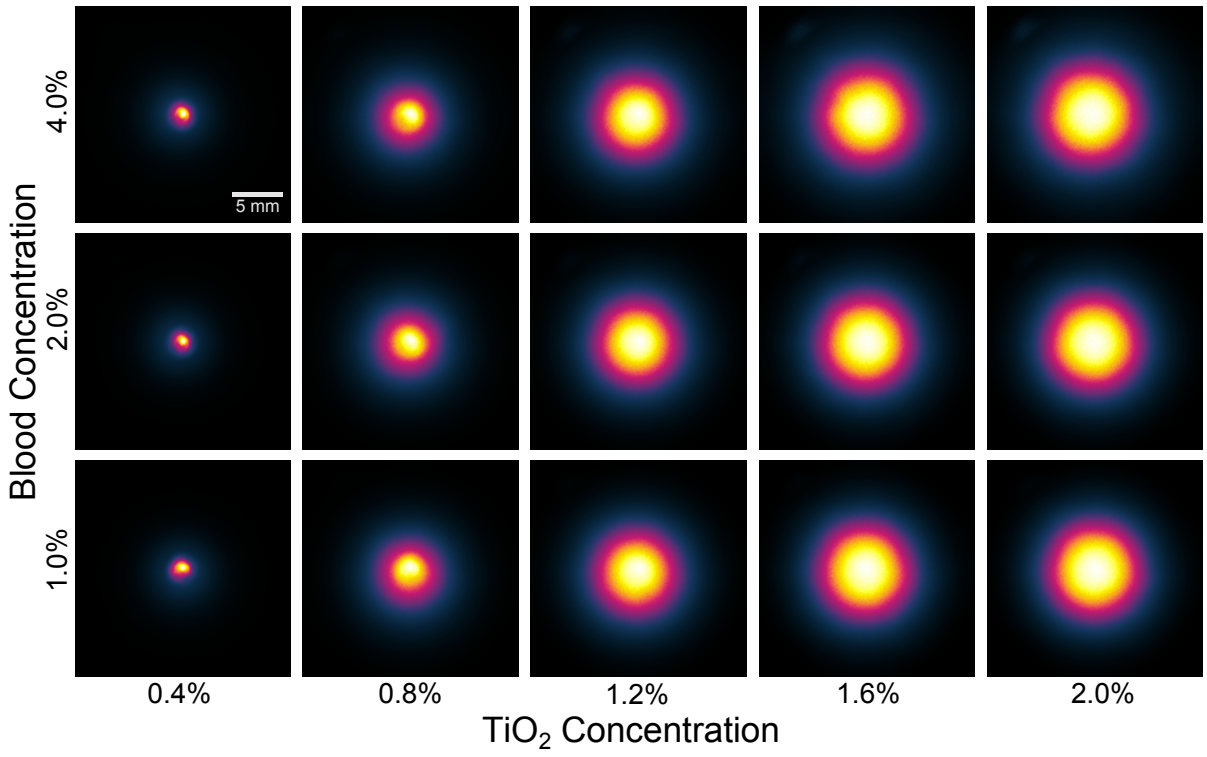

Figure 3.6: Fluorescence point spread function (FPSF) of the 15 tissue mimicking phantoms with varying absorption and scattering properties.

when measuring biological tissue, Figure 3.7B plots the FWHM over the average red pixel value of the phantom at the fluorophore location, which was obtained from the color camera measurements. As expected, the red intensity does not describe the kernel width as well as the scattering coefficient, yet a reasonable goodness of fit ($\mathrm{R}^2 = 0.86$) was achieved.
Based on the obtained fitting, the measured fluorescence was corrected using the proposed algorithm. Since the phantom's optical properties are homogeneous the inhomogeneity map A simplifies to a constant.

$$A = 1 \tag{3.8}$$

The standard deviation map was obtained using both linear fittings shown in Figure 3.7 in conjunction with Equation (3.5). Figure 3.8A displays the fluorescence image of phantom 7, which was corrected to yield the image in Figure 3.8B. Therein the red pixel count was used to obtain the gaussian kernel, decreasing the FWHM from 186 to 70 pixels after correction. The ground truth fluorescence, with a FWHM of 48 pixels, is plotted in Figure 3.8C. The correction

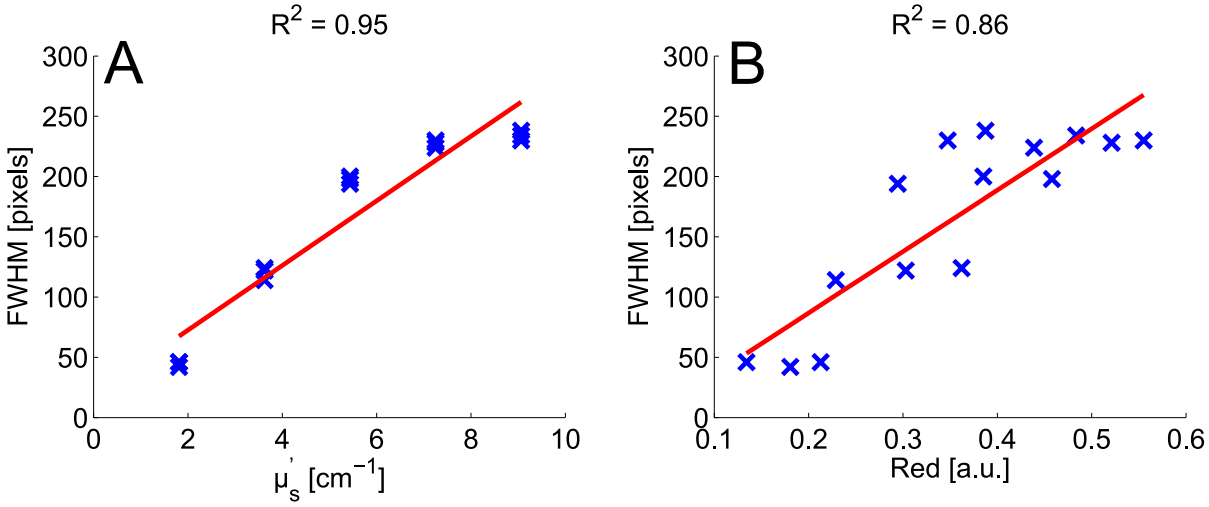

Figure 3.7: FWHM of the fluorescence point spread function (blue), corresponding linear fitting (red) and coefficient of determination R^2 as a function of the phantom's reduced scattering coefficient (A) and the average red pixel intensity (B).

performance over all phantoms is displayed in Figure 3.8D. Thereby the two methods to estimate the kernel were applied to decrease the measured fluorescence width (black) towards the actual fluorophore extend (cyan). The resulting average improvement of the FWHM was 73.7 % for the kernel estimation from the reduced scattering coefficient and 74.2 % using the red channel.

3.2.2.2 Tissue experiments

Measurements of the reduced scattering coefficient were not available for the tissue data, thus due to its simplicity and good performance in the phantom experiment the red channel of the corresponding color images was used to determine both the inhomogeneity A and the standard deviation map.

$$A = R \tag{3.9}$$

$$\sigma = c_1 R + c_2 \tag{3.10}$$

As no calibration measurements were available, the constants c_1 and c_2, relating the diffusion path in cm^{-1} to pixel units, were determined empirically. These constants account for differences in the field of view, magnification and illumination intensity between the utilized setups.

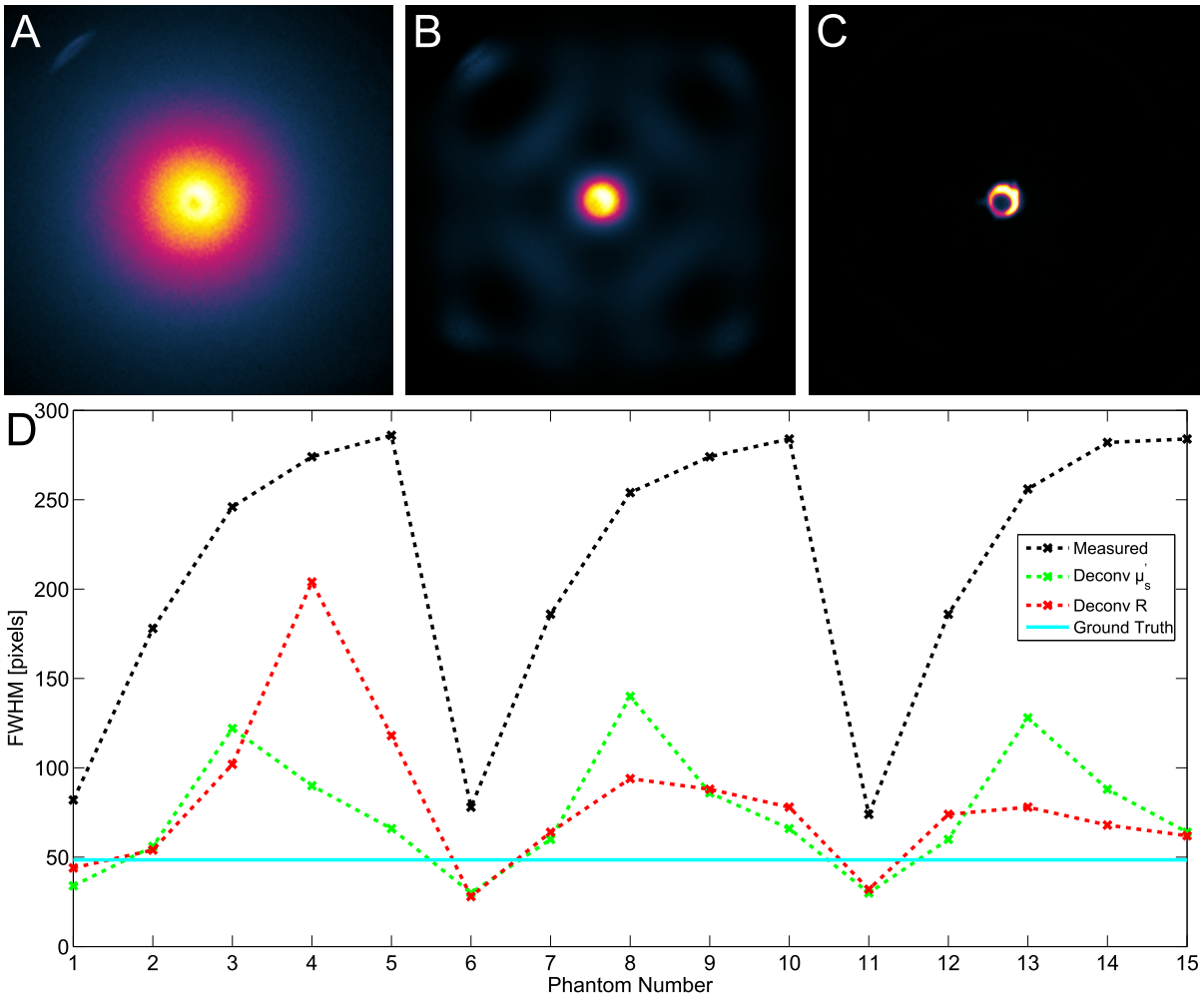

Figure 3.8: A) Fluorescence image of a representative phantom (#7) comprising 2 % Blood and 0.8 % $\mathrm{TiO_2}$ with a full width at half maximum of 186 pixels. B) Phantom image corrected by deconvolution, where the standard deviation was estimated from the red channel, with a FWHM of 70 pixels. C) Fluorescence image of the ground truth phantom, containing neither blood nor titanium (FWHM = 48). D) Graph plotting the FWHM of the 15 phantoms as originally measured (black) and after applying deconvolution where the kernel was obtained from either μ_s' (green) or from the red intensity (red).

Figure 3.9 shows how the space-variant point spread function is constructed from a color reflectance image (Fig. 3.9A) according to Equation (3.4). The color image's red channel is used both as the inhomogeneity map A (Fig. 3.9B) and to obtain the pointwise gaussian standard deviation (Fig. 3.9C) using Equation (3.10). The resulting kernel at the location indicated by the arrow is finally displayed in Figure 3.9D. This FPSF describes a preferred fluorescence propagation into the fatty tissue and a stronger attenuation by the more vascular region in the center.

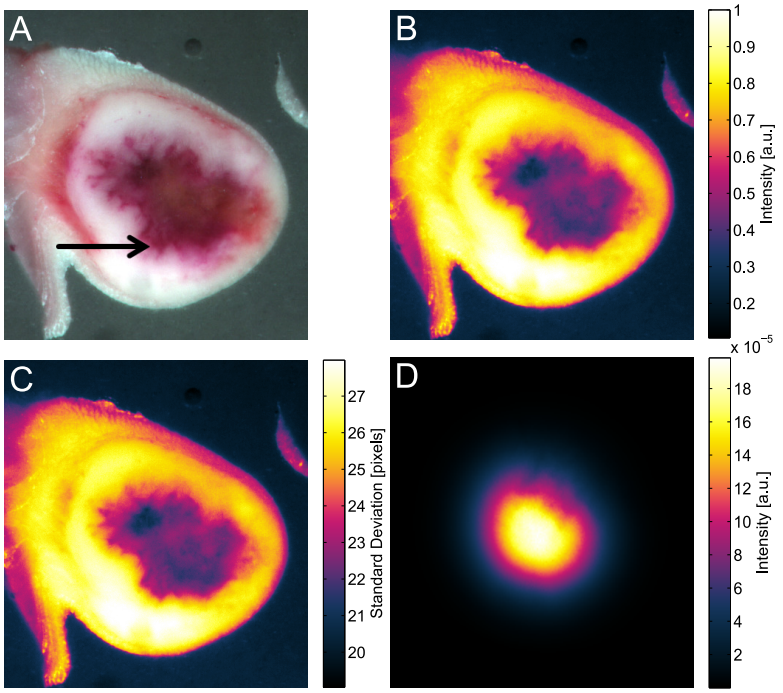

Figure 3.9: A) Color image of a mouse cryosection. B) Corresponding red channel, which is utilized as the inhomogeneity map. C) Map of the kernel standard deviation obtained from the red channel. D) Fluorescence point spread function at the location indicated by the arrow in A)

The results of the space-variant deconvolution, applied to the three mouse datasets, are presented in Figure 3.10. Using space-variant fluorescence point spread functions derived from the color images (Fig. 3.10A–I), the cryosection fluorescence images (Fig. 3.10B–J) are corrected to yield the images displayed in Figures 3.10C–K. For the three datasets a successful correction is achieved, yielding output images that bear a closer resemblance to the gold standard data (Fig. 3.10D–L) than the original fluorescence measurements.

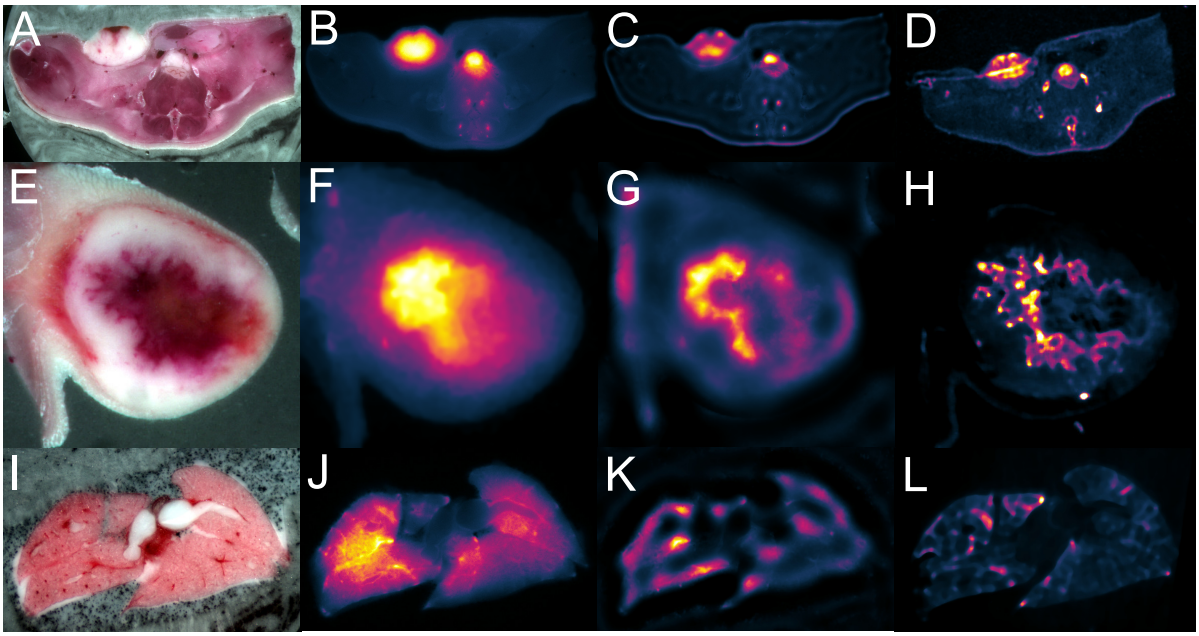

Figure 3.10: A–I) Color images of the three mouse cryosections. B–J) Corresponding fluorescence measurements. C–K) Correction result of the proposed space-variant deconvolution method. D–L) Gold standard scatter-free fluorescence image of a thin tissue slice.

3.2.3 Discussion

A scheme based on space-variant deconvolution was developed to correct the two dimensional signal distortions introduced by diffusive light propagation. Phantom experiments demonstrated, that the local deterioration introduced by scattering can be reversed by deconvolution with an appropriate kernel. Based on color reflectance measurements, a spatially varying fluorescence point spread function was determined. Space-variant deconvolution was realized by a modified Richardson-Lucy algorithm and applied to datasets of cryosectioned mouse tissue. A significant improvement, with respect to the gold standard fluorophor distribution, as measured from thin tissue slices, was observed in the analyzed cases. Specifically, the shape and extend of the fluorescence distribution could be evaluated more precisely, by reducing the signal spread to provide better demarcation (Fig. 3.10G and K) and by revealing features previously disguised by diffusion (Fig. 3.10C).

An important merit of the proposed approach, as opposed to pixel-wise intensity adjustment, is the two dimensional character. Since light propagates through optically inhomogeneous locations due to photon scattering, a correction of such effects requires a model for spatial

interaction. Herein, color reflectance measurements were used to construct a gaussian kernel, based on their observed correlation to the full width at half maximum (FWHM). The kernel was spatially modulated by an inhomogeneity map, also retrieved from the color channel. As the current approach employs only fluorescence and RGB measurements it can easily be integrated into the intraoperative imaging system presented in Chapter 2. In surgical applications of molecular fluorescence imaging, the more accurate spatial delineation of the fluorophore distribution yielded by the deconvolution approach would be of crucial importance to evaluate the tumor margins and preserve healthy tissue.
However, the kernel composition represents an obvious opportunity for improvement. The phantom experiments indicated that the kernel spread mostly varies with the scattering coefficient $\mu_s^{'}$, which however cannot be retrieved using the current setup due to the reflectance's scale invariance to the optical properties [83]. Consequently, further development of the approach could introduce an analytical model, whose parameters are determined by more advanced means, such as narrow band multispectral imaging or measurement schemes involving source-detector separation. Refinements of the iterative Richardson-Lucy implementation might be useful to reduce the influence of noise, ill-posedness and improve iteration convergence. Finally, considering the three-dimensionality of biological tissue and light propagation therein, an extension to incorporate depth effects should be considered, possibly accompanied by applications to 3D fluorescence tomography or volumetric cryoslice image data.

3.3 Wavelength optimization for the determination of tissue properties

Unlike conventional color imaging, which aims to replicate the perception of the human eye, the imaging of endogenous tissue contrast in biomedical applications intends to measure physiological tissue parameters that might be of diagnostic value. Herein, a method to optimize the imaged narrow wavelength bands in a way that yields the best representation of the sample optical properties is presented. Therefore an analytical model for the diffuse reflectance in epi-illumination imaging was investigated. It describes the reflected light intensity at a wavelength as a function of the absorption and scattering properties of tissue. However, the absorption and reduced scattering coefficients themselves are wavelength-dependent, and consequently cannot be resolved from multispectral images [83]. Instead, assuming hemoglobin absorption

and Mie scattering, a novel formulation in terms of three wavelength-independent optical properties is presented. From the analytical expressions the preferred wavebands are determined by optimizing for a well-conditioned inverse problem. Finally, the predicted wavelength sets are validated on liquid phantoms, showcasing that a precise determination of properties such as the hemoglobin oxygenation and scattering power is possible from merely three spectral bands.

3.3.1 Methods

3.3.1.1 Theory

Diffuse reflectance model The analytical model published by Farrell et al. [84] was used for the diffuse imaging of a turbid medium. It gives the following expression for the total reflectance R in a planar epi-illumination setup:

$$R = \frac{a}{2}\left(1 + \exp\left(-\frac{4}{3}N_r\sqrt{3\left(1-a\right)}\right)\right)\frac{1}{1+\sqrt{3\left(1-a\right)}} \tag{3.11}$$

Thereby a is the medium's transport albedo, while N_r is a boundary coefficient that accounts for the difference in refractive indices between air and the medium. For a relative refractive index $n_{rel} = \frac{n_t}{n_a}$ of the tissue-air interface N_r can be calculated as [85]:

$$N_r = \frac{1+r_d}{1-r_d} \tag{3.12}$$

$$r_d = -1.440n_{rel}^{-2} + 0.710n_{rel}^{-1} + 0.668 + 0.0636n_{rel} \tag{3.13}$$

Water is the main constituent of biological tissue, thus its refractive index of $n_{H_2O} = 1.33$ was used for the medium's n_t [86]. With $n_a = 1.00$ for air, a value of $N_r = 2.79$ was computed.

Inversion for albedo Equation (3.11) describes a function that projects an albedo $a \in A_0$ onto a normalized reflection measurement $R \in R_0$ where $R_0 = \{R \in \mathbb{R} | 0 \leq R \leq 1\}$.

$$f : A_0 \to R_0 \tag{3.14}$$

$$f(a) = R \tag{3.15}$$

The function $f(a)$ is defined over the set of albedo values $A_0 = \{a \in \mathbb{R} | 0 \leq a \leq 1\}$ and assumes positive values for the square root functions. Such a continuous and real function is injective if it is either strictly monotonically increasing or decreasing. This can be assessed from its derivative.

$$\begin{aligned}\frac{\partial R}{\partial a} = \frac{\exp\left(-\frac{4}{3}N_r\sqrt{3\,(1-a)}\right)+1}{2\left(\sqrt{3\,(1-a)}+1\right)} + \frac{\sqrt{3}\,a\,\left(\exp\left(-\frac{4}{3}N_r\sqrt{3\,(1-a)}\right)+1\right)}{4\left(\sqrt{3\,(1-a)}+1\right)^2\sqrt{1-a}} \\ + \frac{\sqrt{3}\,N_r\,a\,\exp\left(-\frac{4}{3}N_r\sqrt{3\,(1-a)}\right)}{3\left(\sqrt{3\,(1-a)}+1\right)\sqrt{1-a}}\end{aligned} \tag{3.16}$$

Evaluating the individual terms yields, that the partial derivative $\frac{\partial R}{\partial a}$ is always positive for positive roots and $a \in [0, 1[$. Thus it follows that f is injective. From the intermediate value theorem and the function values $f(a = 0) = 0$ and $f(a = 1) = 1$ it follows, that the computation of the set of the normalized diffuse reflectance $R_0 = \{R \in \mathbb{R} | 0 \leq R \leq 1\}$ is a bijective function. Therefore, f is invertible and an inverse function g exists for which:

$$g : R_0 \to A_0 \tag{3.17}$$

$$g(R) = a \tag{3.18}$$

The existence of an inverse function means that from a single diffuse reflection measurement the medium's transport albedo a can uniquely be determined.

Inversion for the wavelength-independent parameters The transport albedo a at a wavelength λ can be expressed by the reduced scattering coefficient $\mu_s'(\lambda)$ and the absorption coefficient $\mu_a(\lambda)$.

$$a(\lambda) = \frac{\mu_s'(\lambda)}{\mu_a(\lambda) + \mu_s'(\lambda)} \tag{3.19}$$

It was assumed that hemoglobin is the major source of optical absorption in tissue. The absorption coefficient for a blood volume of concentration c_B with the oxygen saturation sO_2 can then be written as follows:

$$\mu_a(\lambda) = c_B \left(sO_2 \mu_a^{HbO_2}(\lambda) + (1 - sO_2)\, \mu_a^{Hb}(\lambda) \right) \tag{3.20}$$

Thereby $\mu_a^{HbO_2}$ and μ_a^{Hb} denote the absorption coefficients of oxygenated and de-oxygenated hemoglobin, respectively. Their documented values in the visible wavelength range were used herein [87]. The reduced scattering coefficient $\mu_s^{'}$ can be expressed according to Mie theory [88] as:

$$\mu_s^{'} = A\lambda^{-b} \tag{3.21}$$

The wavelength-independent optical properties are given as

$$\mathbf{p} = \begin{bmatrix} sO_2 \\ b \\ v \end{bmatrix} \tag{3.22}$$

with $v = \frac{A}{c_B}$. Combining Equation (3.19) with Equations (3.20) and (3.21) yields the albedo as a function of the optical parameters $\mathbf{p}$.

$$a(\lambda, \mathbf{p}) = \frac{\lambda^{-b}}{v \left(sO_2 \mu_a^{HbO_2}(\lambda) + (1 - sO_2)\, \mu_a^{Hb}(\lambda) \right) + \lambda^{-b}} \tag{3.23}$$

As noted above, a series of N spectral measurements can be inverted to yield the albedo at the corresponding wavelengths:

$$G : R_0^N \rightarrow \{a \in \mathbb{R} | 0 \leq a \leq 1\} \tag{3.24}$$

For a set of N distinct wavelengths $\boldsymbol{\lambda} = \begin{bmatrix} \lambda_1 & \lambda_2 & \cdots & \lambda_N \end{bmatrix}^T$ the following notation is used:

$$\begin{bmatrix} a(\lambda_1, \mathbf{p}) \\ a(\lambda_2, \mathbf{p}) \\ \vdots \\ a(\lambda_N, \mathbf{p}) \end{bmatrix} = G \left(\begin{bmatrix} R(\lambda_1, \mathbf{p}) \\ R(\lambda_2, \mathbf{p}) \\ \vdots \\ R(\lambda_N, \mathbf{p}) \end{bmatrix} \right) \tag{3.25}$$

$$\mathbf{a}(\boldsymbol{\lambda}, \mathbf{p}) = G(\mathbf{R}(\boldsymbol{\lambda}, \mathbf{p})) \tag{3.26}$$

Therein $\mathbf{a}(\boldsymbol{\lambda}, \mathbf{p}) \in A_0^N$ and $\mathbf{R}(\boldsymbol{\lambda}, \mathbf{p}) \in R_0^N$. Thus a system of N equations with the three unknowns $\mathbf{p}$ is obtained. In the following the minimum required number of $N = 3$ spectral measurements is assumed to characterize if the system of equations can be solved and how well conditioned it is for different sets $\boldsymbol{\lambda}$.

Invertibility and condition number We consider the function H, that would solve the system denoted by Equation (3.26), i.e. yield the variables $\mathbf{p}$ from the albedo values $\mathbf{a}(\boldsymbol{\lambda})$.

$$H : A_0^N \rightarrow P_0^3 \tag{3.27}$$

$$\mathbf{p} = H(\mathbf{a}(\boldsymbol{\lambda})) \tag{3.28}$$

The concatenation of H and G determines the wavelength-independent parameters from a set of reflectance measurements.

$$\mathbf{p} = H(G(\mathbf{R}(\boldsymbol{\lambda}, \mathbf{p}))) \tag{3.29}$$

The Jacobian matrix $\mathbf{J}$ is used to analyze the resulting problem.

$$\mathbf{J}(\boldsymbol{\lambda}, \mathbf{p}) = \begin{bmatrix} \frac{\partial R(\lambda_1)}{\partial sO_2} & \frac{\partial R(\lambda_1)}{\partial b} & \frac{\partial R(\lambda_1)}{\partial v} \\ \frac{\partial R(\lambda_2)}{\partial sO_2} & \frac{\partial R(\lambda_2)}{\partial b} & \frac{\partial R(\lambda_2)}{\partial v} \\ \frac{\partial R(\lambda_3)}{\partial sO_2} & \frac{\partial R(\lambda_3)}{\partial b} & \frac{\partial R(\lambda_3)}{\partial v} \end{bmatrix} \tag{3.30}$$

Based on the concatenation of H and G, the partial derivatives therein can we written as follows:

$$\frac{\partial R}{\partial sO_2} = \frac{\partial R}{\partial a}\frac{\partial a}{\partial sO_2} \tag{3.31}$$

$$\frac{\partial R}{\partial b} = \frac{\partial R}{\partial a}\frac{\partial a}{\partial b} \tag{3.32}$$

$$\frac{\partial R}{\partial v} = \frac{\partial R}{\partial a}\frac{\partial a}{\partial v} \tag{3.33}$$

While the expression for $\frac{\partial R}{\partial a}$ is given in Equation (3.16), the partial derivatives of a were calculated to be:

$$\frac{\partial a}{\partial sO_2} = -\frac{v\ \left(\mu_a^{HbO_2} - \mu_a^{Hb}\right)}{\lambda^b\left(v\ \left(sO_2\mu_a^{HbO_2} + (1-sO_2)\,\mu_a^{Hb}\right) + \lambda^{-b}\right)^2} \tag{3.34}$$

$$\frac{\partial a}{\partial b} = \frac{\log(\lambda)}{\lambda^{2b}\left(v\ \left(sO_2\mu_a^{HbO_2} + (1-sO_2)\,\mu_a^{Hb}\right) + \lambda^{-b}\right)^2} - \frac{\log(\lambda)}{\lambda^b\ \left(v\ \left(sO_2\mu_a^{HbO_2} + (1-sO_2)\,\mu_a^{Hb}\right) + \lambda^{-b}\right)} \tag{3.35}$$

$$\frac{\partial a}{\partial v} = -\frac{sO_2\mu_a^{HbO_2} + (1-sO_2)\,\mu_a^{Hb}}{\lambda^b\left(v\ \left(sO_2\mu_a^{HbO_2} + (1-sO_2)\,\mu_a^{Hb}\right) + \lambda^{-b}\right)^2} \tag{3.36}$$

Let J_F be the Jacobian determinant of the matrix $\mathbf{J}$, which itself is a function of the optical properties and the measured wavelengths.

$$J_F\left(\boldsymbol{\lambda}, \mathbf{p}\right) = \det\left(\mathbf{J}\left(\boldsymbol{\lambda}, \mathbf{p}\right)\right) \tag{3.37}$$

If the function H exists for a set of values $\mathbf{p}$ and $\boldsymbol{\lambda}$ then the Jacobian determinant at that point is non-zero. The converse statement, namely that the existence of H follows from $J_F \neq 0$ remains unproven. For the polynomial case it is known as the Jacobian conjecture [89].

Equilibration is applied to the Jacobian in order to reduce the influence of scaling and obtain an optimal condition number [90].

$$\mathbf{J}^* = \mathbf{D}\mathbf{J} \tag{3.38}$$

Thereby the equilibration matrix $\mathbf{D}$ is a diagonal matrix whose k-th diagonal entry is the inverse of the k-th row sum of $\mathbf{J}$. An inverse of the Jacobian exists for a set of measured wavelengths and optical properties that yield a determinant $J_F \neq 0$.

$$\mathbf{J}_{inv}\left(\boldsymbol{\lambda}, \mathbf{p}\right) = \mathrm{inv}\left(\mathbf{J}^*\left(\boldsymbol{\lambda}, \mathbf{p}\right)\right) \tag{3.39}$$

The condition number $\kappa_{\mathbf{p}}$ of this linearized approximation can be computed as:

$$\kappa_{\mathbf{p}}\left(\boldsymbol{\lambda}, \mathbf{p}\right) = \frac{\left\|\mathbf{J}_{inv}^*\left(\boldsymbol{\lambda}, \mathbf{p}\right)\right\| \left\|\mathbf{R}\left(\boldsymbol{\lambda}, \mathbf{p}\right)\right\|}{\left\|\mathbf{p}\right\|} \tag{3.40}$$

Optimization It can be seen from Equation (3.40) that the condition number is a function of both the selected wavelengths $\boldsymbol{\lambda}$ and the specific wavelength-independent parameters $\mathbf{p}$. Consequently, the condition number of a set of wavelengths was defined as $\kappa_{\mathbf{p}}$ for the worst case parameters, i.e. by taking the maximum over the vector $\mathbf{p}$.

$$\kappa\left(\boldsymbol{\lambda}\right) = \max_{\mathbf{p}}\left(\kappa_{\mathbf{p}}\left(\boldsymbol{\lambda}, \mathbf{p}\right)\right) \tag{3.41}$$

The ranges given in Table 3.4, derived from data published in the literature [80], were utilized for the values in $\mathbf{p}$.

Parameter	Minimum	Maximum
sO_2	0 %	100 %
b	0.5	4.1
v	$1.5 \cdot 10^{-7}$	$5 \cdot 10^{-3}$

Table 3.4: Ranges of the wavelength-independent properties in biological tissue.

For the set of possible wavelengths, 10 nm bandpass filters around the central wavelengths shown in Table 3.5 were assumed, corresponding to the available optical filters for the phantom experiment.

460	470	480	491	500	510	520	532
541	550	561	570	580	590	600	610
620	630	640	650	660	670	790	800

Table 3.5: Central wavelengths of the 10 nm bandpass filers employed in the wavelength optimization.

The condition number $\kappa\left(\boldsymbol{\lambda}\right)$ was computed for all possible wavelength triplets, among which those with the lowest condition number were considered the best wavelengths for the determination of the optical properties, since they are minimally sensitive to variances of the diffuse reflectance measurements.

3.3.1.2 Phantom experiment

A series of eleven homogeneous liquid phantoms was measured as a gold standard reference for the retrieval of the wavelength-independent optical properties. Whole rabbit blood was mixed with Intralipid (Sigma-Aldrich, St. Louis, US-MO), with the blood concentration ranging from 2 % to 6 % and the Intralipid concentration ranging from 0.4 % to 2 %. The hemoglobin oxygenation status of the phantoms was modified by adding sodium dithionite in appropriate amounts [91]. The liquid was placed on a magnetic stirrer to prevent sedimentation and imaged with a Luca-R camera (Andor Technology, Belfast, Northern Ireland) through a Z16 APO A lens (Leica Microsystems, Wetzlar, Germany). Reference values for b and v were obtained by a least-squares fitting of the published spectrum of Intralipid [92] to Equation (3.21).

$$\mu_s^{'} = A\lambda^{-b} \tag{3.21}$$

The fitting result is plotted in Figure 3.11, wherein the values $A = 6.45 \cdot 10^5$ and $b = 0.966$ were obtained. From the value of A and the known blood and Intralipid concentrations the

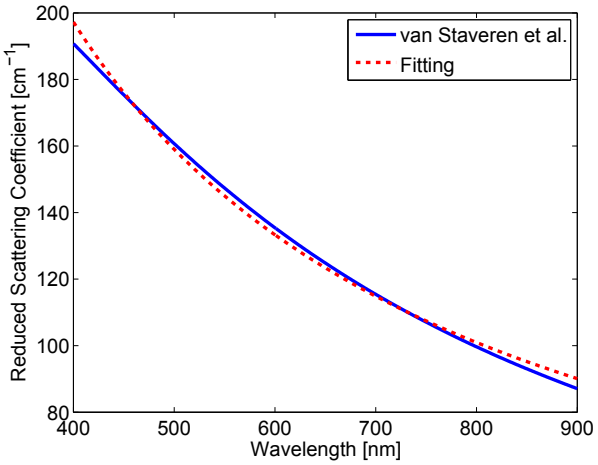

Figure 3.11: Least-squares fitting of the spectrum of Intralipid 10 % ($c_I = 0.1$) to Equation (3.21), with the computed variables $A = 6.45 \cdot 10^5$ and $b = 0.966$.

values of v were calculated by:

$$v = \frac{c_B}{c_I A} \tag{3.42}$$

The utilized mixing concentrations, as well as the respective wavelength-independent parameters over the phantom set are detailed in Table 3.6.

Phantom	$[\#]$	1	2	3	4	5	6	7	8	9	10	11
c_I	$[\%]$	2.0	1.2	2.0	1.2	2.0	1.2	2.0	0.4	2.0	1.2	1.2
c_B	$[\%]$	6.0	4.0	4.0	6.0	4.0	4.0	6.0	2.0	4.0	6.0	4.0
sO_2	$[\%]$	95	98	98	98	2	69	76	100	39	97	87
b							0.966					
v	$[10^{-6}]$	4.7	5.2	3.1	7.8	3.1	5.2	4.7	7.8	3.1	7.8	5.2

Table 3.6: Phantom properties for the wavelength reference experiment, comprising the Intralipid concentrations c_I, the blood concentration c_B, the measured hemoglobin oxygenation sO_2, the scattering power b and the parameter v.

Reflectance measurements of the phantoms were taken with a total of 24 different 10 nm bandpass filters (Chroma Technology, Bellows Falls, US-VT) placed in a custom made filter wheel (Cairn-Research, Kent, UK), whose central wavelengths are listed in Table 3.5. Illumination was provided by a KL2500 halogen lamp (Schott AG, Mainz, Germany). The spectral behavior of the light source and the CCD sensor response over wavelength needed to be taken into account. Consequently, one of the eleven phantoms was used for calibration by assuming its properties to be known, while the other ten were used for the evaluation, i.e. their parameters were retrieved from an inversion of the diffuse reflectance model using non-linear least-squares curve fitting. The average reconstruction error over the possible parameter range (Tab. 3.4) was computed by using every phantom for calibration once and taking the mean of all iterations, effectively a leave-ten-out cross-validation scheme.
In this way the average reconstruction error for the 2024 possible wavelength triplets was calculated, providing a gold standard quality metric for all possible combinations of three filters.

3.3.2 Results

The condition number $\kappa(\boldsymbol{\lambda})$ was calculated for all possible wavelength triplets $\boldsymbol{\lambda} = \begin{bmatrix} \lambda_1 & \lambda_2 & \lambda_3 \end{bmatrix}^T$ among the available filters. Condition number values ranged from 325.3 to $1.5 \cdot 10^9$, the latter indicating a Jacobian with a determinant J_F that is numerically close to zero, making it impossible to retrieve the desired parameters. Non-linear least-squares inversion was performed on the phantom data and the average error was computed with respect to the known optical properties. The optimal wavelength sets, determined analytically and from the phantoms, are

listed in Table 3.7.

Optimization					Phantoms				
Rank [#]	κ [a.u.]	Wavelengths [nm]			Rank [#]	Avg. Error [%]	Wavelengths [nm]		
1	325.3	500	790	800	1	4.58	480	630	800
2	408.9	510	670	800	2	4.60	470	500	550
3	419.2	510	660	800	3	4.62	480	640	800
4	429.9	510	650	800	4	4.66	480	620	800
5	432.4	500	670	800	5	4.66	470	491	550
6	440.3	500	660	800	6	4.69	480	630	790
7	441.1	510	640	800	7	4.72	480	640	790
8	448.6	500	650	800	8	4.82	480	660	800
9	449.1	510	670	790	9	4.83	460	491	550
10	451.0	520	670	800	10	4.84	510	640	800

Table 3.7: Optimal set of wavelength triplets as determined from the condition number and phantom experiments, with their respective rank and quality measure.

It can be seen that there is a good agreement between the numerical solution and the phantom experiment data. Specifically, both methods suggest that measuring a green wavelength (480–510 nm), a red wavelength (640–670 nm) and a near-infrared wavelength (790–800 nm) promises a good result. The phantom results show that for realistic cases a residual error of about 4.5 % range persists, which can be considered a good result given the broad parameter range and the limited number of spectral measurements.
The attained reconstruction error for the wavelength sets suggested by condition number optimization is plotted in Figure 3.12. On average, the reconstruction error for the 50 wavelength sets with the lowest condition number was 0.46 % higher than the error for the 50 optimal wavelengths. However, the highest ranked triplet represents a notable outlier that yields a significantly higher error than the subsequent ones.

3.3.3 Discussion

The optimal set of narrow-band filters for the reconstruction of wavelength-independent tissue optical properties was determined from an analytical model of the total diffuse reflectance. The predicted quality of possible wavelength triplets among a set of available filters was com-

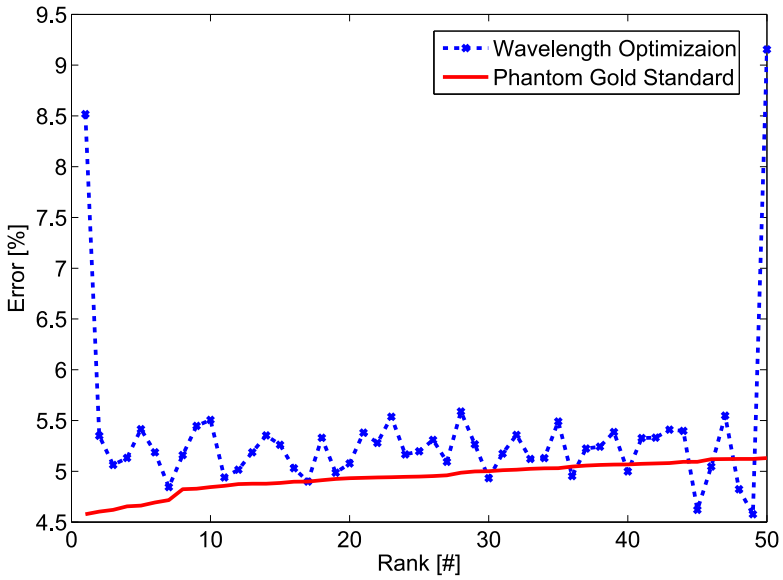

Figure 3.12: Optical properties reconstruction error for the wavelength sets yielded by the numerical analysis (blue) with respect to the gold standard error obtained from the phantom experiment (red).

pared with the reconstruction error on liquid phantoms of known optical properties. A good agreement between the predicted and measured inversion accuracy was observed, indicating that the proposed analytical model is suitable to determine optimal spectral measurement points without the need for an empirical validation. A consistent pattern in the highest ranked triplets was the selection of a green, a red and a near-infrared wavelength.

An important feature of the presented approach is that it is based purely on the assumed light propagation model and optical spectra, not taking into account the method used for inversion or the image acquisition process. On the one hand this can be considered an advantage, because an optimization that addresses the properties of the underlying mathematical problem can be considered to be more universal and independent of the specific setup and measurement conditions. On the other hand, the relatively high reconstruction error obtained from the triplet with the lowest condition number suggests that inaccuracies in the model reduce the predictive power of individual numeric results. While just two outliers in the first 50 ranks show the general correctness of the approach, it has to be noted that common patterns among the optimal wavelengths should be considered rather than precise individual numbers. Possible model refinements could increase the reliability and robustness of the presented op-

timization technique. Incorporating the scattering properties of blood, as documented in the literature [93], could be a promising approach, resulting in a more complex formula than Equation (3.21). Similarly, blood has been considered as the only absorber, while it is known that water [94] and other tissue components also contribute [95]. Furthermore, the wavelength dependence of both the light source and the CCD sensor could be included in the model to account for their contribution to the spectral variance in real measurements. Recently an alternative model for the diffuse reflectance has been published [96], and while a strong agreement with the model utilized herein has been reported [97] it could still be interesting to compare the results between them.

Bibliography

[1] G. Moore, "Cramming more components onto integrated circuits", *Electronics*, vol. 38, no. 8, pp. 114–117, Apr. 1965.

[2] D. Geer, "Chip makers turn to multicore processors", *Computer*, vol. 38, no. 5, pp. 11–13, May 2005.

[3] C. H. van Berkel, "Multi-core for mobile phones", in *Proceedings of the Conference on Design, Automation and Test in Europe*, ser. DATE '09, European Design and Automation Association, 2009, pp. 1260–1265.

[4] H. Sutter and J. Larus, "Software and the concurrency revolution", *Queue*, vol. 3, pp. 54–62, 7 Sep. 2005.

[5] S. Akhter and J. Roberts, *Multi-core programming: increasing performance through software multi-threading*. Intel Press, 2006.

[6] T. Möller, T. Akenine-Möller, E. Haines, and N. Hoffman, *Real-time rendering*. AK Peters Ltd, 2008.

[7] Nvidia Corporation, *Compute Unified Device Architecture Programming Guide*, NVIDIA, Santa Clara, CA, 2007.

[8] D. Kirk and W. Wen-mei, *Programming massively parallel processors: A Hands-on approach*. Morgan Kaufmann Publishers Inc. San Francisco, CA, USA, 2010.

[9] J. D. Owens, D. Luebke, N. Govindaraju, M. Harris, J. Krüger, A. Lefohn, and T. J. Purcell, "A survey of general-purpose computation on graphics hardware", *Computer Graphics Forum*, vol. 26, no. 1, pp. 80–113, 2007.

[10] W. Hwu, K. Keutzer, and T. Mattson, "The concurrency challenge", *Design & Test of Computers, IEEE*, vol. 25, no. 4, pp. 312–320, 2008.

[11] J. Rattner, "Tera-Scale Research Program", in *Intel Dev. Forum, Spring*, 2006.

[12] J. Held, J. Bautista, and S. Koehl, "From a few cores to many: a tera-scale computing research overview", *Intel White Paper*, 2006.

[13] E. Lindholm, J. Nickolls, S. Oberman, and J. Montrym, "Nvidia tesla: a unified graphics and computing architecture", *Micro, IEEE*, vol. 28, no. 2, pp. 39–55, 2008.

[14] P. Micikevicius, "Optimizing CUDA", *NVIDIA Developer Newsletter*, 2008.

[15] J. Sanders and E. Kandrot, *CUDA by Example: An Introduction to General-Purpose GPU Programming*. Addison-Wesley, 2010.

[16] NVIDIA, *NVIDIA's Next Generation CUDA Compute Architecture: FERMI*, 2009.

[17] C. Wittenbrink, E. Kilgariff, and A. Prabhu, "Fermi GF100 GPU architecture", *Micro, IEEE*, vol. 31, no. 2, pp. 50–59, 2011.

[18] D. Patterson, "The top 10 innovations in the new NVIDIA Fermi architecture, and the top 3 next challenges", *NVIDIA Whitepaper*, 2009.

[19] R. Nath, S. Tomov, and J. Dongarra, "An improved MAGMA GEMM for Fermi graphics processing units", *International Journal of High Performance Computing Applications*, vol. 24, no. 4, pp. 511–515, 2010.

[20] G. Tan, L. Li, S. Triechle, E. Phillips, Y. Bao, and N. Sun, "Fast implementation of DGEMM on Fermi GPU", in *Proceedings of 2011 International Conference for High Performance Computing, Networking, Storage and Analysis*, ACM, 2011, p. 35.

[21] Y. Torres, A. Gonzalez-Escribano, and D. R. Llanos, "Understanding the impact of CUDA tuning techniques for Fermi", in *High Performance Computing and Simulation (HPCS), 2011 International Conference on*, IEEE, 2011, pp. 631–639.

[22] Y. Torres, A. Gonzalez-Escribano, and D. R. Llanos, "Using Fermi architecture knowledge to speed up CUDA and OpenCL programs", in *Parallel and Distributed Processing with Applications (ISPA), 2012 IEEE 10th International Symposium on*, IEEE, 2012, pp. 617–624.

[23] J. Nickolls and W. Dally, "The GPU computing era", *Micro, IEEE*, vol. 30, no. 2, pp. 56–69, 2010.

[24] Y. Pan, R. Whitaker, A. Cheryauka, and D. Ferguson, "Feasibility of GPU-assisted iterative image reconstruction for mobile C-arm CT", *Medical Imaging*, 72585J–1, 2009.

[25] B. Catanzaro, B. Su, N. Sundaram, Y. Lee, M. Murphy, and K. Keutzer, "Efficient, high-quality image contour detection", in *Computer Vision, 2009 IEEE 12th International Conference on*, IEEE, 2009, pp. 2381–2388.

[26] M. D. Hill and M. R. Marty, "Amdahl's law in the multicore era", *Computer*, vol. 41, no. 7, pp. 33–38, Jul. 2008.

[27] B. Bayer, "Color imaging array", US Patent 3,971,065, 1976.

[28] R. Lukac and K. N. Plataniotis, "Color filter arrays: design and performance analysis", *Consumer Electronics, IEEE Transactions on*, vol. 51, no. 4, pp. 1260–1267, 2005.

[29] J. Adams and J. Hamilton, "Design of practical color filter array interpolation algorithms for digital cameras", in *Proc. SPIE*, vol. 3028, 1997, pp. 117–125.

[30] P. Longère, X. Zhang, P. Delahunt, and D. Brainard, "Perceptual assessment of demosaicing algorithm performance", *Proceedings of the IEEE*, vol. 90, no. 1, pp. 123–132, 2002.

[31] B. K. Gunturk, J. Glotzbach, Y. Altunbasak, R. W. Schafer, and R. M. Mersereau, "Demosaicking: color filter array interpolation", *Signal Processing Magazine, IEEE*, vol. 22, no. 1, pp. 44–54, 2005.

[32] R. Ramanath, W. Snyder, G. Bilbro, and W. Sander, "Demosaicking methods for bayer color arrays", *Journal of Electronic imaging*, vol. 11, no. 3, pp. 306–315, 2002.

[33] X. Li, B. Gunturk, and L. Zhang, "Image demosaicing: a systematic survey", in *Proc. of SPIE*, vol. 6822, 2008, 68221J.

[34] H. S. Malvar, L. He, and R. Cutler, "High-quality linear interpolation for demosaicing of bayer-patterned color images", in *Acoustics, Speech, and Signal Processing, 2004. Proceedings.(ICASSP'04). IEEE International Conference on*, IEEE, vol. 3, 2004, p. 485.

[35] M. McGuire, "Efficient, high-quality bayer demosaic filtering on GPUs", *Journal of Graphics, GPU, and Game Tools*, vol. 13, no. 4, pp. 1–16, 2008.

[36] D. Dudgeon and R. Mersereau, "Multidimensional digital signal processing", *Prentice-Hall Signal Processing Series, Englewood Cliffs: Prentice-Hall, 1984*, vol. 1, 1984.

[37] J. Reese and S. Zaranek, "GPU Programming in MATLAB", *MATLAB Newsletter: Technical Articles*, 2011.

[38] R. Weissleder and V. Ntziachristos, "Shedding light onto live molecular targets", *Nature medicine*, vol. 9, no. 1, pp. 123–128, 2003.

[39] R. Weissleder, "Molecular imaging in cancer", *Science*, vol. 312, no. 5777, pp. 1168–1171, 2006.

[40] W. Stummer, U. Pichlmeier, T. Meinel, O. D. Wiestler, F. Zanella, and H.-J. Reulen, "Fluorescence-guided surgery with 5-aminolevulinic acid for resection of malignant glioma: a randomised controlled multicentre phase iii trial", *The Lancet Oncology*, vol. 7, no. 5, pp. 392–401, 2006.

[41] G. M. van Dam, G. Themelis, L. M. A. Crane, N. J. Harlaar, R. G. Pleijhuis, W. Kelder, A. Sarantopoulos, J. S. de Jong, H. J. G. Arts, A. G. J. van der Zee, B. Joost, P. S. Low, and V. Ntziachristos, "Intraoperative tumor-specific fluorescence imaging in ovarian cancer by folate receptor-α targeting: first in-human results", *Nature Medicine*, vol. 17, no. 10, pp. 1315–1319, 2011.

[42] P.-L. Hsiung, J. Hardy, S. Friedland, R. Soetikno, C. B. Du, A. P. Wu, P. Sahbaie, J. M. Crawford, A. W. Lowe, C. H. Contag, *et al.*, "Detection of colonic dysplasia *in vivo* using a targeted heptapeptide and confocal microendoscopy", *Nature Medicine*, vol. 14, no. 4, pp. 454–458, 2008.

[43] A. V. Oppenheim, R. W. Schafer, J. R. Buck, *et al.*, *Discrete-time signal processing*. Prentice-hall Englewood Cliffs, 1989, vol. 2.

[44] J. G. Proakis, *Digital Signal Processing–Principles, Algorithms and Applications*. Upper Saddle River, NJ: Prentice Hall, 1995.

[45] G. H. Granlund and H. Knutsson, *Signal processing for computer vision*. Springer, 1995, vol. 2.

[46] J. C. Russ, *The image processing handbook*. CRC press, 2010.

[47] R. N. Bracewell, *The Fourier transform and its applications*, 3rd edition. Boston, MA: McGraw Hill, 2000.

[48] R. C. Gonzalez and R. E. Woods, *Digital Image Processing*, 3rd Edition. Upper Saddle River, NJ: Prentice Hall, 2007.

[49] J. G. McNally, T. Karpova, J. Cooper, and J. A. Conchello, "Three-dimensional imaging by deconvolution microscopy", *Methods*, vol. 19, no. 3, pp. 373–385, 1999.

[50] J. B. Sibarita, "Deconvolution microscopy", in *Microscopy Techniques*, Springer, 2005, pp. 201–243.

[51] J. L. Starck, E. Pantin, and F. Murtagh, "Deconvolution in astronomy: a review", *Publications of the Astronomical Society of the Pacific*, vol. 114, no. 800, pp. 1051–1069, 2002.

[52] E. Pantin, J. L. Starck, and F. Murtagh, "Deconvolution and blind deconvolution in astronomy", in *Blind Image Deconvolution: Theory and Applications*, P. Campisi and K. Egiazarian, Eds. Boca Raton, US-FL: CRC Press, 2007.

[53] P. Campisi and K. Egiazarian, *Blind Image Deconvolution: Theory and Applications*. Boca Raton, US-FL: CRC Press, 2007.

[54] D. Kundur and D. Hatzinakos, "Blind image deconvolution", *Signal Processing Magazine, IEEE*, vol. 13, no. 3, pp. 43–64, 1996.

[55] A. Lohmann and D. Paris, "Space-variant image formation", *JOSA*, vol. 55, no. 8, pp. 1007–1013, 1965.

[56] T. Lauer, "Deconvolution with a spatially-variant psf", in *Astronomical Telescopes and Instrumentation*, International Society for Optics and Photonics, 2002, pp. 167–173.

[57] H. J. Trussell and S. Fogel, "Identification and restoration of spatially variant motion blurs in sequential images", *Image Processing, IEEE Transactions on*, vol. 1, no. 1, pp. 123–126, 1992.

[58] W. Xia, R. M. Lewitt, and P. R. Edholm, "Fourier correction for spatially variant collimator blurring in spect", *Medical Imaging, IEEE Transactions on*, vol. 14, no. 1, pp. 100–115, 1995.

[59] J. Brauers, C. Seiler, and T. Aach, "Direct PSF estimation using a random noise target", in *IS&T/SPIE Electronic Imaging*, International Society for Optics and Photonics, 2010, 75370B–75370B.

[60] J. Wang, B. Guo, Q. Sun, and Z. Lu, "Third-order aberration fields of pupil decentered optical systems", *Optics Express*, vol. 20, no. 11, pp. 11 652–11 658, 2012.

[61] K. Thompson, "Description of the third-order optical aberrations of near-circular pupil optical systems without symmetry", *JOSA A*, vol. 22, no. 7, pp. 1389–1401, 2005.

[62] J. G. Nagy and D. P. O'leary, "Fast iterative image restoration with a spatially varying psf", in *Optical Science, Engineering and Instrumentation'97*, International Society for Optics and Photonics, 1997, pp. 388–399.

[63] L. Denis, E. Thiébaut, and F. Soulez, "Fast model of space-variant blurring and its application to deconvolution in astronomy", in *Image Processing (ICIP), 2011 18th IEEE International Conference on*, IEEE, 2011, pp. 2817–2820.

[64] J. Simpkins and R. L. Stevenson, "Parameterized modeling of spatially varying optical blur", *Journal of Electronic Imaging*, vol. 23, no. 1, pp. 013 005–013 005, 2014.

[65] J. G. Nagy and D. P. O'Leary, "Restoring images degraded by spatially variant blur", *SIAM Journal on Scientific Computing*, vol. 19, no. 4, pp. 1063–1082, 1998.

[66] P. Escande, P. Weiss, and F. Malgouyres, "Image restoration using sparse approximations of spatially varying blur operators in the wavelet domain", in *Journal of Physics: Conference Series*, IOP Publishing, vol. 464, 2013, p. 012 004.

[67] B. Zhang, J. Zerubia, and J.-C. Olivo-Marin, "Gaussian approximations of fluorescence microscope point-spread function models", *Applied Optics*, vol. 46, no. 10, pp. 1819–1829, 2007.

[68] L. Bar, N. Sochen, and N. Kiryati, "Restoration of images with piecewise space-variant blur", in *Scale Space and Variational Methods in Computer Vision*, Springer, 2007, pp. 533–544.

[69] A. G. Marrugo, M. S. Millán, M. Šorel, and F. Šroubek, "Restoration of retinal images with space-variant blur", *Journal of Biomedical Optics*, vol. 19, no. 1, pp. 016 023–016 023, 2014.

[70] L. Shao and J. Karp, "Cross-plane scattering correction-point source deconvolution in PET", *Medical Imaging, IEEE Transactions on*, vol. 10, no. 3, pp. 234–239, 1991.

[71] Z. Kam, B. Hanser, M. Gustafsson, D. Agard, and J. Sedat, "Computational adaptive optics for live three-dimensional biological imaging", *Proceedings of the National Academy of Sciences*, vol. 98, no. 7, pp. 3790–3795, 2001.

[72] G. Themelis, J. Yoo, K. Soh, R. Schulz, and V. Ntziachristos, "Real-time intraoperative fluorescence imaging system using light-absorption correction", *Journal of Biomedical Optics*, vol. 14, no. 6, p. 064 012, 2009.

[73] P. A. Valdés, F. Leblond, A. Kim, B. T. Harris, B. C. Wilson, X. Fan, T. D. Tosteson, A. Hartov, S. Ji, K. Erkmen, *et al.*, "Quantitative fluorescence in intracranial tumor: implications for ala-induced ppix as an intraoperative biomarker", *Journal of Neurosurgery*, vol. 115, no. 1, p. 11, 2011.

[74] N. Dey, L. Blanc-Feraud, C. Zimmer, P. Roux, Z. Kam, J.-C. Olivo-Marin, and J. Zerubia, "Richardson–lucy algorithm with total variation regularization for 3d confocal microscope deconvolution", *Microscopy research and technique*, vol. 69, no. 4, pp. 260–266, 2006.

[75] M. Prato, R. Cavicchioli, L. Zanni, P. Boccacci, and M. Bertero, "Efficient deconvolution methods for astronomical imaging: algorithms and idl-gpu codes.", *Astronomy & Astrophysics/Astronomie et Astrophysique*, vol. 539, 2012.

[76] D. Fish, A. Brinicombe, E. Pike, and J. Walker, "Blind deconvolution by means of the richardson–lucy algorithm", *JOSA A*, vol. 12, no. 1, pp. 58–65, 1995.

[77] D. L. Snyder, "Modifications of the lucy-richardson iteration for restoring hubble space telescope imagery", in *The Restoration of HST Images and Spectra*, R. L. White and R. J. Allen, Eds., vol. 1, Space Telescope Science Institute, 1991, pp. 56–62.

[78] M. I. Cabrera, O. M. Alfano, and A. E. Cassano, "Absorption and scattering coefficients of titanium dioxide particulate suspensions in water", *The Journal of Physical Chemistry*, vol. 100, no. 51, pp. 20 043–20 050, 1996.

[79] S. T. Flock, S. L. Jacques, B. C. Wilson, W. M. Star, and M. J. van Gemert, "Optical properties of intralipid: a phantom medium for light propagation studies", *Lasers in Surgery and Medicine*, vol. 12, no. 5, pp. 510–519, 1992.

[80] S. L. Jacques, "Optical properties of biological tissues: a review", *Physics in medicine and biology*, vol. 58, no. 11, R37, 2013.

[81] N. Barapatre, P. Symvoulidis, W. Möller, F. Prade, N. C. Deliolanis, S. Hertel, G. Winter, A. Ö. Yildirim, T. Stoeger, O. Eickelberg, V. Ntziachristos, and O. Schmid, "Cryoslicing imaging for quantitative assessment of 3d dose distribution of fluorescent substances in the lungs of mice", 2014.

[82] A. Sarantopoulos, G. Themelis, and V. Ntziachristos, "Imaging the bio-distribution of fluorescent probes using multispectral epi-illumination cryoslicing imaging", *Molecular Imaging and Biology*, vol. 13, no. 5, pp. 874–885, 2011.

[83] G. Zonios and A. Dimou, "Modeling diffuse reflectance from semi-infinite turbid media: application to the study of skin optical properties", *Optics express*, vol. 14, no. 19, pp. 8661–8674, 2006.

[84] T. J. Farrell, M. S. Patterson, and B. Wilson, "A diffusion theory model of spatially resolved, steady-state diffuse reflectance for the noninvasive determination of tissue optical properties invivo", *Medical Physics*, vol. 19, no. 4, pp. 879–888, 1992.

[85] R. Groenhuis, J. Ten Bosch, and H. A. Ferwerda, "Scattering and absorption of turbid materials determined from reflection measurements. 2: measuring method and calibration", *Applied Optics*, vol. 22, no. 16, pp. 2463–2467, 1983.

[86] E. Hecht and A. Zajac, *Optics*, 4th edition. San Francisco, US-CA: Addison-Wesley, 2002.

[87] S. Prahl. (1999). Optical absorption of hemoglobin, [Online]. Available: `http://omlc.ogi.edu/spectra/hemoglobin/`.

[88] C. F. Bohren and D. R. Huffman, *Absorption and scattering of light by small particles*. Hoboken, US-NJ: John Wiley & Sons, 2008.

[89] A. van den Essen, *Polynomial Automorphisms and the Jacobian Conjecture*, ser. Progress in Mathematics. Basel: Birkhäuser, 2000, vol. 190.

[90] A. V. D. Sluis, "Condition numbers and equilibration of matrices", *Numerische Mathematik*, vol. 14, no. 1, pp. 14–23, 1969.

[91] K. Briely-Sabo and A. Bjornerud, "Accurate de-oxygenation of ex vivo whole blood using sodium dithionite", in *Proc. Intl. Sot. Mag. Reson. Med*, vol. 8, 2000, p. 2025.

[92] van Staveren, Hugo J and Moes, Christian J M and van Marie, Jan and Prahl, Scott A and van Gemert, Martin J C, "Light scattering in intralipid-10% in the wavelength range of 400-1100 nm", *Applied Optics*, vol. 30, no. 31, pp. 4507–4514, 1991.

[93] D. J. Faber, M. C. Aalders, E. G. Mik, B. A. Hooper, M. J. Gemert, and T. G. Leeuwen, "Oxygen saturation-dependent absorption and scattering of blood", *Physical review letters*, vol. 93, no. 2, p. 028 102, 2004.

[94] R. M. Pope and E. S. Fry, "Absorption spectrum (380–700 nm) of pure water. II. Integrating cavity measurements", *Applied Optics*, vol. 36, no. 33, pp. 8710–8723, 1997.

[95] C.-L. Tsai, J.-C. Chen, and W.-J. Wang, "Near-infrared absorption property of biological soft tissue constituents", *Journal of Medical and Biological Engineering*, vol. 21, no. 1, pp. 7–14, 2001.

[96] J. R. Lorenzo, *Principles of diffuse light propagation: light propagation in tissues with applications in biology and medicine*. World Scientific, 2012.

[97] P. Symvoulidis, K. M. Jentoft, P. B. Garcia-Allende, J. Glatz, J. Ripoll, and V. Ntziachristos, "Steady-state total diffuse reflectance with an exponential decaying source", *Optics Letters*, vol. 39, no. 13, pp. 3919–3922, 2014.

Chapter 4

Experimental validation

4.1 Pre-clinical imaging

4.1.1 Laparoscopic imaging of colorectal cancer in mice[1]

4.1.1.1 Introduction

Colorectal cancer (CRC) is the third most prevalent cancer in the United States [2] and worldwide [3], resulting in an estimated number of 608.000 deaths annually [4]. Treatment of colorectal cancer is frequently performed using endoscopic approaches, in particular laparoscopic intervention, which is a preferred method over open surgery [5, 6]. Cancer identification during surgical treatment relies on the physician's visual ability to discriminate healthy from malignant tissue under white light illumination. However, the low intrinsic contrast of carcinomas, especially with respect to the propagating tumor margin or smaller foci of disease, makes it difficult to precisely demarcate and completely excise during surgery. In addition, color endoscopy cannot visualize under the surface, making it virtually impossible to discriminate deep-seated cancer or accurately evaluate the penetration extend of carcinomas. As a result, color endoscopy is known to miss tumors in up to 24 % of the cases [7].
Optical contrast enhancement using narrow band imaging (NBI), chromoendoscopy and autofluorescence imaging (AFI) has been considered in imaging colorectal cancer during colonoscopy. NBI uses narrow bandpass filters to enhance the hemoglobin contrast and thus visualize the tumor vascularization [8]. A randomized study published by Adler et al. [9] concluded that

[1] Text and images from this section have been published in Ref. [1].

adenomata are detected more frequently using NBI compared to color endoscopy, however the detection difference observed between the two methods was not statistically significant. In chromoendoscopy non-specific dyes are applied to visualize micro-anatomical changes in the mucosa, but the technique is mostly used for biopsy guidance. Autofluorescence imaging is based on the emission of intravital fluorescent molecules and has been used for the detection of lesions [10] and polyps [11] in colonoscopy as well as in oral oncology [12], among others. While AFI can help to identify molecular differences between tissues, the method lacks sufficient sensitivity and specificity for improving clinical outcome. These techniques have been mostly applied for screening and diagnostic purposes in colonoscopy and their use in surgical laparoscopy of colorectal cancer is not established.

The administration of fluorescent agents has been also considered to improve endoscopic detection of cancer. Indocyanine green (ICG) is an FDA approved fluorescent dye that has been used in medical procedures for over 50 years. ICG is a cyanine dye used as a blood-pool agent that can be administered intravenously to visualize blood vessels, for example in eye angiography [13]. It may demarcate vascular tumors and extravagate in cases of elevated vascular permeability, however it has not shown highly specific cancer identification. Similar cancer detection performance has been observed with other non-specific dyes, such as fluorescein. Alternatively, fluorescent molecules with targeting capacity to cancer moieties have been instead considered in recent years to increase the sensitivity and specificity of cancer detection [14, 15]. Their ability to specifically target molecular signatures of cancer promises a great increase of efficiency and recognition rates also in colonoscopic screening [16]. Importantly, the first clinical translation of a targeted agent was recently achieved for surgical guidance in open ovarian cancer surgery [17], possibly heralding the use of targeted fluorescent agents in endoscopic procedures as well. The study indicated that targeted fluorochromes may result in higher detection of cancer over visual inspection, offering a promising outlook for surgical molecular guidance.

In order to facilitate the clinical translation of these molecular agents to laparoscopic interventions the intra-operative imaging system was adapted for laparoscopic use, as described in Section 2.2.2. Herein, its ability to detect colorectal cancer in animal models at video-rate performance is demonstrated, based on targeted fluorescence signals in vivo.

4.1.1.2 Animal model

To induce tumors, 8 week old FvB mice (Charles River, Wilmington, US-MA) were injected into the peritoneum with a single dose of azoxymethane (AOM; A2853, Sigma-Adrich, St. Louis, US-MO) at $10\frac{\mathrm{mg}}{\mathrm{kg}}$. AOM is a methylating genotoxic colonic carcinogen [18] that induces mutations in the β-catenin gene, resulting in the persistent activation of the wnt pathway [19] and initiates tumor development in the distal colon of mice and rats [20]. Since hyperactivation of the wnt signaling pathway by mutations is considered one of the earliest events in the sequence of genetic changes that leads to human colon cancer development, AOM induced mouse colon tumors recapitulates molecular and pathological features seen in the sporadic form of the human disease [21].
After AOM treatment animals were exposed to 3 cycles of dextran sulfate sodium salt administration (DSS; 160110, MP Biomedicals, Illkirch, France) in the drinking water (cycle 1: 3 %, 5 days; cycle 2: 2 %, 5 days; cycle 3: 1,5 %, 5 days). DSS is directly toxic for intestinal epithelial cells and impairs the integrity of the mucosal barrier that induces inflammation [22]. Administration of several cycles of DSS leads to chronic colitis and drives tumor progression [23, 24].
IntegriSense 750 (PerkinElmer, Waltham, US-MA) was injected intravenously at the recommended dose of 2 nmol per mouse. IntegriSense is a nonpeptide fluorescence imaging agent that specifically targets αvβ3 integrin receptors commonly expressed by tumor cells as well as by neovasculature [25]. Mice were sacrificed 24 hours after agent injection and intra-operative and ex vivo images of the murine colon were taken. For ex vivo imaging the colon was removed, flushed with phosphate buffered saline (PBS) and cut open. White light and laser illumination was delivered through the human laparoscope and video-rate recordings were acquired at a working distance of 2 cm. The sample was placed in a light-tight box, into which the laparoscope was inserted through a small incision, thus creating an environment mimicking the conditions during human laparoscopy.
The presence of colorectal tumors was further confirmed using common histological techniques. The colon was fixed as a "Swiss roll" in 4 % paraformaldehyde at 4 °C overnight and embedded in paraffin. Sections of 2 μm were cut and stained with hematoxylin and eosin (H&E). All procedures were performed in accordance with institutional guidelines.

4.1.1.3 Results

The epi-illumination images obtained from the colon of the mouse are shown in Figure 4.1. This model showcases the system's ability to image fluorescent markers with high resolution and high sensitivity in tissue.
The color images displayed in Figure 4.1A) and E) directly relate to the surgeon's vision, however, the lack of contrast between healthy and malignant tissue is apparent. The fluorescence images in Figure 4.1B) and F) show a distinct accumulation of the NIR contrast agent in the colon. The fluorescence and color channel overlay was created using PCA color picking as described in Section 2.1.5 and is shown in Figure 4.1C) and G). Histopathological examination using hematoxylin and eosin (H&E) staining was performed on the excised colon to confirm the malignant nature of the tissue. In addition, video recordings were acquired during the experiments, with a frame rate of 10 fps or more, to showcase the system's capability for real-time imaging. The video-rate display of the molecular contrast provided by IntegriSense not only helps in localizing the tumor but can also give instant feedback during surgical resection.

4.1.1.4 Discussion

Applied to tissue measurements, the system was shown capable to detect physiologically relevant fluorescence signals from tumors when using targeted fluorochromes at frame-rates of 10 fps. The average signal-to-noise ratio (SNR) in the tissue measurements was approximately 21 dB, which was well above the detection limit of the camera. Clinical application of the imaging system will make high demands on sensitivity. However, by adapting the illumination intensity within ANSI limits and by possibly slowing down the video rate, even more sensitive detection could be achieved for areas of controversial signal appearance. Using the GPU processing power such adaptive processes could be applied dynamically during the measurement. The ability to simultaneously visualize color and fluorescence images in video mode can be beneficial during a surgical intervention in comparison with systems that switch between color and fluorescence measurements in a time-share mode. In addition the use of a low end camera may not be an optimal solution for high-performance fluorescence imaging. Therefore a dual channel, dual CCD-chip system would be necessary for endoscopic fluorescence molecular imaging, for example in laparoscopic colorectal surgery.

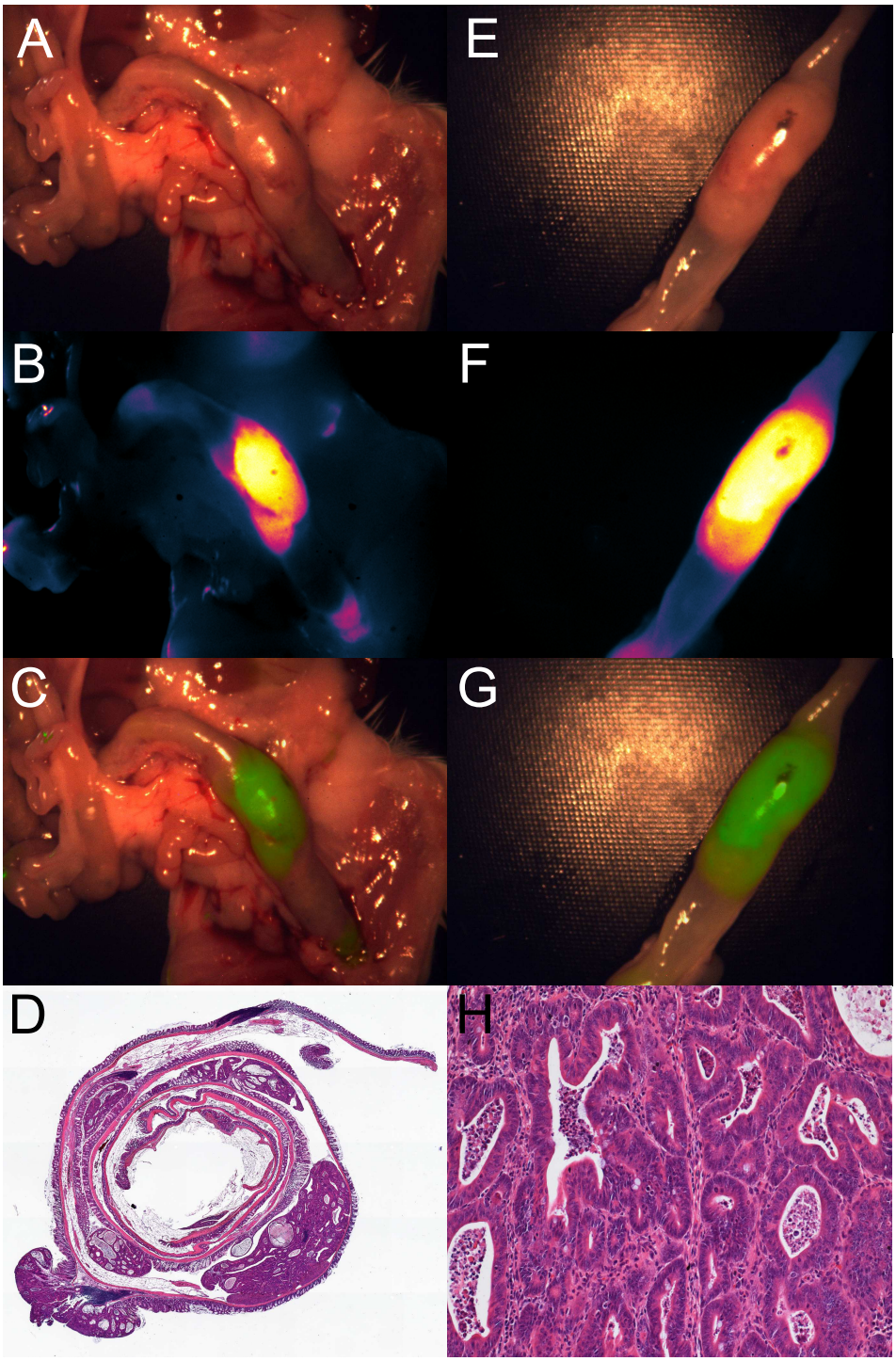

Figure 4.1: Laparascopic imaging of the mouse colon performed ex vivo in the abdomen (A-C) and on the excised colon (E-G). A) and E) Color channel images. B) and F) Fluorescence images of the IntegriSense 750 distribution within the colon. C) and G) Composite overlay image, where the fluorescence is thresholded and superimposed via alpha blending on the color image for better visualization. D) H&E stained "Swiss roll" of the colon. H) Detail (20x) of H&E staining.

4.1.2 Drug-based molecular imaging of colorectal cancer[2]

Widespread clinical use of targeted imaging with near-infrared fluorescence has been limited by translational hurdles. The successful development and approval of novel contrast agents is a time and cost intensive process. Prior to toxicity and efficacy studies of the agent, promising targets need to be identified through the histological characterization with respect to marker overexpression, histomorphological and molecular heterogeneity of excised tumor lesions. A recently proposed approach to overcome the regulatory hurdles for the administration of such novel contrast agents involves the usage of optically labeled drugs [27]. Among the proposed drugs, bevacizumab (Avastin®, Hoffmann-La Roche, Basel, Switzerland) was identified as a promising choice. Bevacizumab is a humanized monoclonal antibody that prevents the growth of blood vessels by neutralizing all isoforms of vascular endothelial growth factor A (VEGF-A), which is expressed by tumors to stimulate angiogenesis. Anti-VEGF therapy was originally studied for colorectal cancer [28] and has since found widespread clinical use for the treatment of various other cancer types. The antibody bevacizumab was combined with clinically applicable NIR fluorophores, specifically IRDye 800CW, as suggested in [29]. Such dyes are not FDA approved, but are currently being used clinically in Europe (ClinicalTrials.gov number, NCT01508572).

Recently, the NIR fluorescent tracer bevacizumab-800CW was shown to exhibit selective tumor uptake in mouse xenografts of human ovarian, breast and gastric cell lines [30]. In this Section, its applicability for the endoscopic imaging of colorectal cancer (CRC) shall be evaluated. In Section 2.2.4 an adaptation of a clinical grade gastrointestinal fiberscope for simultaneous, video-rate, color and NIR fluorescence imaging, as well as a miniaturized alternative that can be integrated with conventional medical videocolonoscopes were presented. Herein, the technique for in vivo characterization of the molecular characteristics of CRC lesions is pre-clinically validated in a mouse model, employing targeted fluorescent antibodies.

Colonoscopy is recommended as a colorectal cancer screening method every ten years for patients older than 50 years [31, 32]. Screening strategies based on sigmoidoscopy and colonoscopy are cost-effective [33] and commonly used [34] procedures that are expected to reduce the incidence of CRC by about 80 % [35, 36]. However they currently miss up to 22 % of polyps or flat adenomata [37], underlining the need for improved contrast in screening modalities.

[2]Text and images from this section have been published in Ref. [26].

4.1.2.1 Materials and methods

The IRDye 800CW-NHS (LI-COR Biosciences, Lincoln, US-NE) was labeled to bevacizumab as described previously [30]. Briefly, bevacizumab was reacted with the dye at a molar ratio of 1:4 in a phosphate buffered medium and subsequently purified by ultra centrifugation. A labeling efficiency of 85–90 % was obtained using size-exclusion high-performance liquid chromatography, resulting in an average of 3.5 dye molecules per antibody.
Six male athymic nude mice (Harlan, Horst, The Netherlands), 16–20 weeks old, were subcutaneously inoculated with $2 \cdot 10^6$ human colon tumor cell lines HCT116$^{\mathrm{luc}}$ (Caliper Life Sciences, Hopkinton, US-MA) in the left dorsal flank. Growth of the tumors was monitored by measuring their diameter with a digital caliper, while stable transfection of the cell lines with the firefly gene *luciferase* also allowed for screening by luminescence imaging of the mice using an IVIS Spectrum (Caliper Life Sciences). The mice were fed with alfalfa-free food to minimize intestinal autofluorescence. The labeled antibody bevacizumab-800CW was intravenously administrated via the penile vein after four weeks, when tumors measured approximately 6–15 mm in diameter. All experiments were performed using general anesthesia (2.5 % isoflurane in oxygen $0.4\frac{\mathrm{l}}{\mathrm{min}}$), approved by the animal welfare committee of the University of Groningen and carried out in accordance with the Dutch Animal Welfare Act of 1997. Endoscopic explorations are performed in epi-illumination and detection geometry. Consequently, the fluorescence intensity measured by the proposed imaging platforms is modulated by the tissue optical properties and the depth of the recorded activity, and does not directly report the underlying agent concentration. Although correction techniques that aim at the compensation of the effects of absorption and scattering in tissue to quantify the absolute fluorophore concentration are emerging [38, 39], an overall solution to this challenge is still pending. In light of this, the tumor-to-background ratio (TBR) for the labeled antibody is estimated as the quotient of the average fluorescence intensities in the segmented lesion and a ring region of interest (ROI) adjacent to the tumor. Because of the fluorescence signal being diffused to the surrounding areas as a consequence from scattering, this approach might result in estimated TBRs being significantly smaller than if a non-tumorous region away from the lesion was selected. It tries, however, to minimize the variation of the tissue optical properties between selected areas.

4.1.2.2 Results

Representative images of the in vivo testing of the sensitivity of the proposed NIR fluorescence endoscopes are presented in Figure 4.2. The shown images correspond to a subcutaneous colonic tumor created by inoculating human colon carcinoma cells in the left dorsal flank of the mouse. The mouse was intravenously administered with the targeted contrast agent 48 hours prior to the examination. Color and NIR fluorescence epi-illumination images were obtained with the adapted gastrointestinal endoscope (Fig. 4.2A and 4.2B) and the miniature cholangioscope (Fig. 4.2D and 4.2E) placed above the mouse. The mouse is in turn placed on a $1\,\text{cm} \times 1\,\text{cm}$ grid to have an estimation of the tumor size. Gaussian filtering was applied to mitigate the visualization of the honeycomb pattern typical of fiberscopes and originating from the claddings around each fiber within the coherent imaging bundle. Coregistered color and fluorescence images are displayed both independently and superimposed (Fig. 4.2C and 4.2F) to the user by the custom designed software. The fluorescence images in Fig. 4.2D and 4.2E are superimposed on the color images using the overlay as described in Section 2.1.5 to generate the composite images in Fig. 4.2C and 4.2F. Comparison of the top and middle horizontal panels in Figure 4.2 evidences the limitations of the alternative designed to be inserted through the accessory channel of conventional videoscopes, mainly regarding its low resolution, as expected from the restricted number of individual fibers that compose the coherent bundle, and its restricted field of view. The observed fluorescence signal, which is elevated even through the skin, also suggests that its sensitivity, however, is sufficient.
In clinical endoscopy the endoscope is first introduced towards the proximal end of the colon, the cecum, and then imaging is performed while extracting the endoscope backwards. In this situation the section of the colon lumen that needs to be imaged at every instant has approximately a cylindrical shape with a diameter between 2.5–4 cm (depending on insufflation) and a depth of 4–5 cm from the tip of the endoscope. Figure 4.3 demonstrates the capability of the proposed approach for the minimally invasive visualization of the VEGF expression in the lesions present in this cylindrical imaged section of the colon for future human clinical studies. The adapted fiberscope for gastrointestinal endoscopy was again placed above the mouse at approximate distances of 2, 4 and 6 cm. It is important to note here the sharpness of the margins between the subcutaneous lesion and the surrounding areas, which showcases the preferential accumulation in the lesions of the targeted agent. The average TBR measured from the segmented subcutaneous lesions to the surrounding ring ROIs was 2.07.

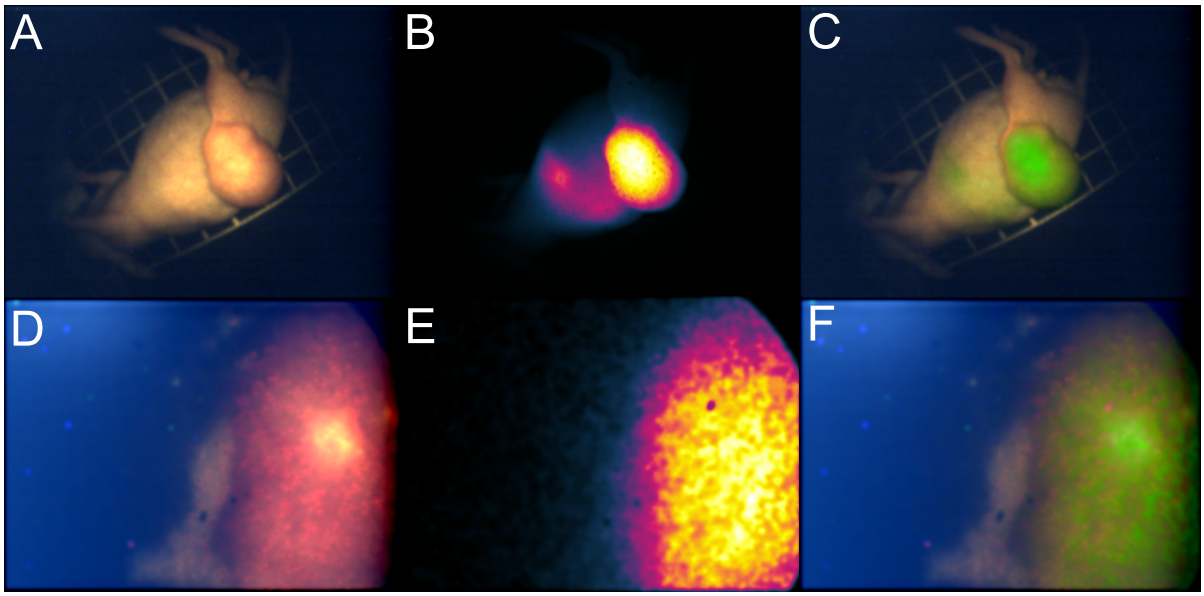

Figure 4.2: Comparison of the visualization of a subcutaneous tumor with the proposed imaging platforms; Color images under white-light illumination, fluorescence and color with superimposed fluorescence acquired with the adapted fiberscope for gastrointestinal endoscopy (A–C) and the miniature cholangioscope (D–F).

4.1.2.3 Discussion

Fluorescence molecular guidance is expected to have outstanding relevance regarding early lesion detection and can reveal functional and morphological information of the detected lesions, thereby improving the diagnostic yield of surveillance colonoscopy and identifying the optimal treatment for the diagnosed patient. However, these clinical potentialities are currently prevented by the regulatory difficulties in the clinical propagation of disease-specific fluorescent agents and the lack of a commercially available flexible endoscope that is capable of acquiring simultaneous color and NIR fluorescence images at video-rates. The straight-forward development of an adequate technological platform was realized in Section 2.2.4, while herein the employment of a contrast agent based on an approved monoclonal antibody for therapy was showcased.

Regarding the minimization of the translational risk with respect to new chemical entities that have never been administered to humans, an optical agent based on a clinically approved drug, that targets a therapeutically relevant carcinoma-related biomarker, namely bevacizumab targeting VEGF, was used. Specificity of binding of the labeled drug was demonstrated in sub-

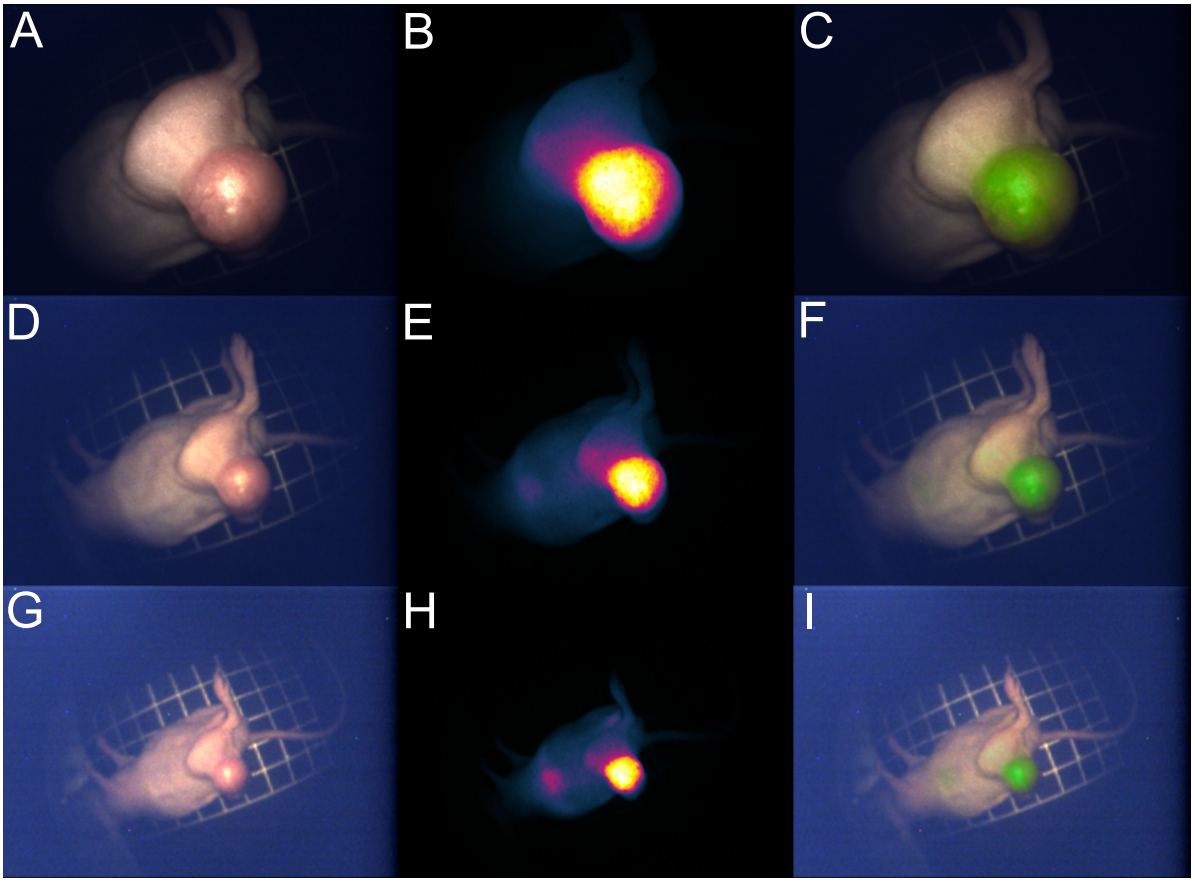

Figure 4.3: Representative images that showcase the characterization of the VEGF expression in the inoculated subcutaneous tumor in 2-6 cm upfront in the bowel with an insufflation-dependent diameter; color images (A, D, and G), fluorescence (B, E, and H), and color with superimposed fluorescence (C, F, and I) were acquired with the adapted fiberscope for gastrointestinal endoscopy at 2, 4 and 6 cm distances, respectively.

cutaneous murine tumor models and an average TBR in the NIR fluorescence channel of over 2 was found even when the ROI for the background was selected adjacent to the segmented lesions. The employment of an antibody targeting disease-associated human biomarkers, which is intended to enable the pathway to clinical translation in colonoscopy of the technique, prevents, however, its demonstration in an animal model of colon cancer. Future research includes the investigation of alternative mouse models, such as modified peritoneal, orthotopic and genetic tumor models to allow their visualization from inside the colon lumen. Furthermore, and although the study was focused on the visualization of biomarker expression for the identification of optimal treatments, a red-flag technique that facilities the detection of small and precursor lesions could be based on an identical methodology, provided that alternative contrast agents targeting established biomarkers that are overexpressed in colorectal adenomas, such as trastuzumab targeting human epidermal growth factor receptor 2 (HER2), were used [40]. Although the data on HER2 expression in colorectal cancer are still ambiguous due to differences in staining and scoring techniques, further confirmation of the pathophysiological role of cytoplasmic HER2 would create a new treatment option for about 360000 patients a year, a clear breakthrough in the treatment of colorectal cancer. This molecular characterization would allow immediate patient selection, and in the case of tumor heterogeneity can potentially be used for follow-up of targeted therapy [41].

Systemically administered agents may offer better lesion targeting within the entire field of view, as well as avoid spraying inhomogeneity, and provide better access to deeper seated lesions by comparison with topically sprayed fluorescent agents that are also considered as an alternative approach to reduce the translational risk for new agents. Although challenged by the difficulties in the regulatory process, it is expected that these agents benefit from the experience in nuclear medicine [42] and, thereby, are expected to find a pathway to clinical translation (ClinicalTrials.gov number, NCT01508572).

The benefits of fluorescence imaging in the NIR have been highlighted in the accomplished preclinical validation, namely deep photon penetration, the enhancement in the tumor-to-background ratio through a minimization of the tissue autofluorescence and its easiness of integration around conventional white-light endoscopy in patient care suites since it does not overlap with normal human or color vision. In spite of this, detected fluorescence intensity, and as a consequence the characterization of the heterogeneity of the biomarker expression, is still affected by light-tissue interaction phenomena and further research is required for precise quantification of the agent uptake. Though, areas with clear positive and negative target

expression can be elucidated with this approach. Another limitation is that cross-sectional imaging is not possible and, even if the fluorescence signals can be collected from depths of at least few millimeters, these appear attenuated and mixed with more superficial signals. This implies that the determined molecular information will always be surface-weighted and to address this limitation other novel imaging modalities would need to be incorporated [43]. Altogether, a pre-clinical wide-field technique based on NIR targeted fluorescence was developed for the detection of precursor lesions of CRC and the determination of the molecular characteristics of the detected lesions. Specific binding of a monoclonal antibody labeled with IRDye 800CW to lesions overexpressing a therapeutically relevant carcinoma-related human biomarker was shown and the sensitivity of the proposed endoscopic imaging platforms was proven to be sufficient for the inspection of 0.72–6 cm upfront in the bowel with an insufflation-dependent diameter, as it is expected for the clinical application. The relevance of this endoscopic imaging modality in surveillance colonoscopy procedures is being explored in an ongoing clinical study (NL-43407.042.113).

4.2 Interventional imaging

4.2.1 Near infrared fluorescence cholangiopancreatoscopy[3]

4.2.1.1 Introduction

The diagnosis of malignant conditions in the biliary and pancreatic ducts remains challenging [45, 46]. Endoscopic retrograde cholangiopancreatography (ERCP) is a widespread method for the assessment and therapy of biliary and pancreatic diseases [47], however, its diagnostic sensitivity is considered unsatisfactory, with reported values ranging from 43–81% [48]. The recognition of small lesions and tumors in early stages is particularly challenging [49]. *Cholangiopancreatoscopy*, i.e. white light imaging of the biliary and pancreatic ducts through fiber- or camera-based miniature endoscopes, provides improved biopsy guidance [50] and direct visualization of epithelial lesions. Optical inspection has been found beneficial for the diagnosis and localization of various conditions of the biliary ducts [51]. It was originally introduced for the visualization of stones during bile duct exploration [52], but the technique has since gained importance in diagnosing cholangiocarcinoma [53] as well as the localization

[3]Text and images from this section have been published in Ref. [44].

of intraductal papillary mucinous neoplasm (IPMN) [54]. However, white light endoscopy is still mostly based on visual inspection, leading to high miss rates and lack of specificity, which makes the detection of small or subsurface lesions challenging. Uhlmann et al. reported a benign histopathological diagnosis for 14 % of patients with suspected cholangiocarcinoma [55]. Endoscopic procedures are furthermore affected by parameters that range from resolution achieved by the employed endoscopes to the training and experience of the physician [56].

Enhanced endoscopic imaging methods such as chromoendoscopy [57, 58], narrow band imaging (NBI) [59, 60], and autofluorescence imaging (AFI) [61, 62] have been introduced to emphasize the fine features of the mucosal structure of biliary and pancreatic tracts, however none of them yielded the desired sensitivity and specificity [63–65].

Near-infrared fluorescence guidance using exogenously administered dyes differs from these approaches since contrast can be engineered by selecting and targeting desired biomarkers. It comes therefore with the potential to enhance the sensitivity and the specificity of detection. A strong advantage of fluorescence detection is that it can outline even small lesions, since fluorescence signals can act as physiological or molecular beacons, compared to NBI or AFI which generally exhibit strong background signals and therefore reduced contrast. Correspondingly, selection of adept biomarkers can lead to enhancing tissue characterization, differentiation and diagnosis. Fluorescence imaging directly relates to the physician's vision and, when near-infrared fluorochromes are employed, sub-surface visualization and reduced contamination by tissue auto-fluorescence can be accomplished over imaging in the visible. These essential advantages have been for long heralded as important for improving interventional procedures and have been more recently demonstrated in the field of optical image-guided surgery, showing the advantages of fluorescence molecular imaging for highlighting the contrast between healthy and malignant tissue in resection surgeries [66, 67] and for sentinel lymph node mapping [68, 69]. Additionally, NIR fluorescence imaging with tumor specific agents would offer optimal specificity and facilitate an accurate assessment of tumor-free margins [17].

The use of NIR detection becomes even more important in cholangiopancreatoscopy. As the endoscopes employed become smaller for insertion in narrow cavities, image quality also drops, making color endoscopy more challenging. In this case the use of beacon signals may be invaluable for improving detection and outline regions that possibly require closer inspection. For this reason we examined here NIR detection through a clinical cholangioscope employed in routine procedures, combined with real-time sensitive color and fluorescence imaging.

Medical endoscopes that are currently employed in hospitals are, with few exceptions, videoscopes [70], i.e. camera tip based scopes, with insufficient sensitivity to acquire fluorescence signals within the real-time constraints of surveillance procedures. Additionally, they do not provide the capability to simultaneously acquire color and fluorescence signals. In the particular case of cholangioscopy, both reusable and semidisposable fiberoptic cholangioscope systems are available for peroral retrograde and percutaneous use [71]. Furthermore, enhanced intraoperative visualization of pancreatic tumors has been previously reported [72] employing a rigid laparoscope and a single camera that swapped between visible and fluorescent images with a foot switch.

Instead we opted herein for concurrent white-light and NIR fluorescence flexible endoscopy utilizing a system comprising a color camera and an ultra-sensitive CCD for fluorescence acquisition operating in parallel, combined with a common fiber-optic bundle, in a similar fashion to custom instruments used by others in endovascular imaging [73]. This section demonstrates the contrast enhancement in the visualization of diseased tissue attained with NIR-fluorescence guidance in clinical cholangiopancreatoscopies. These endoscopic explorations provide direct visualization of the biliary and pancreatic ducts and are performed with miniature endoscopes that are mostly fiberoptic based due to the limited commercial availability of video-cholangioscopes [71]. Consequently, it is the ideal medical discipline for demonstrating the first clinical translation, according to the authors' knowledge, of this novel gastroendoscopic imaging technique based on NIR-fluorescence guidance and processing approach.

4.2.1.2 Patients

Two patients suspected for biliopancreatic malignancy were examined. Endoscopic examinations were performed under conscious sedation with midazolam and propofol. ICG was injected intravenously at a dose of $0.5\frac{\mathrm{mg}}{\mathrm{kg}}$. Image acquisition was performed within 30 minutes after injection, using the fiberoptic babyscope introduced via the accessory channel of the mother endoscope, as described above. Procedures were performed according to the hospital's ethics commission approval #2381/09.

Patient one (male, 49 years) was referred to the department with an incidentally detected cystic lesion of the pancreatic head. Routine laboratory tests were normal and the patient did not report any symptoms. Endoscopic ultrasound revealed a dilation of the main pancreatic duct in the pancreatic head, and main duct intraductal papillary mucinous neoplasm (MD-

IPMN) was suspected. For further evaluation, pancreatoscopy was performed.
Patient two (male, 63 years) was transferred to the department with painless jaundice and increasing cholestasis. Indeterminate distal biliary stricture was described using CT scan and magnetic resonance cholangiopancreatography. Endoscopic retrograde pancreatography (ERCP) and endoscopic brush cytology were performed for further evaluation.

4.2.1.3 Results

ICG is well known to bind to plasma proteins such as albumin, globulins, and lipoproteins [74] and has therefore been largely exploited for imaging of angiogenesis. However, if only ICG fluorescence images are provided, the overall accuracy of the approach may be compromised. Since color and NIR fluorescence images are acquired strictly simultaneously it is possible to provide the endoscopist with a pseudo-diagnosis image that overlays on the color image the areas with higher probability of tumor appearance.
Real-life fluorescence guidance in routine clinical surveillance endoscopies was conducted to demonstrate the capabilities of the imaging system and the contrast enhancement attained in tumor visualization.
Figure 4.4A–C) and E–G) show representative images obtained during the endoscopic procedures. Gaussian filtering was applied to suppress the honeycomb pattern resulting from the fiber claddings. The color images A) and E) show suspicious areas in the pancreatic and bile duct respectively, however the low tissue contrast makes accurate lesion delineation difficult. The corresponding fluorescence images in B) and F) both exhibit a signal-to-noise ratio (SNR) of approximately 15 dB, which lies well above the detection limit. While ICG does not directly highlight cancer, the obtained SNR indicates a significantly increased perfusion in the respective areas. Color and NIR images were co-registered, segmented and superimposed using transparent alpha-blending to produce the overlay images C) and G).
In patient one, white light pancreatoscopy showed a suspicious area in the pancreatic head. Using ICG fluorescence imaging, a villous proliferation within the pancreatic duct highly suspected for IPMN was detected. Additionally, the detailed extent of the IPMN could be evaluated. Based on these results, the patient was transferred to surgery to perform pancreaticoduodenectomy. Figure 4.4D) shows the hematoxylin and eosin (H&E) staining of a biopsy sample. Pathological analysis of the operative specimen confirmed suspected diagnosis of intestine type IPMN with papillary structure, columnar epithelium and luminal mucin.

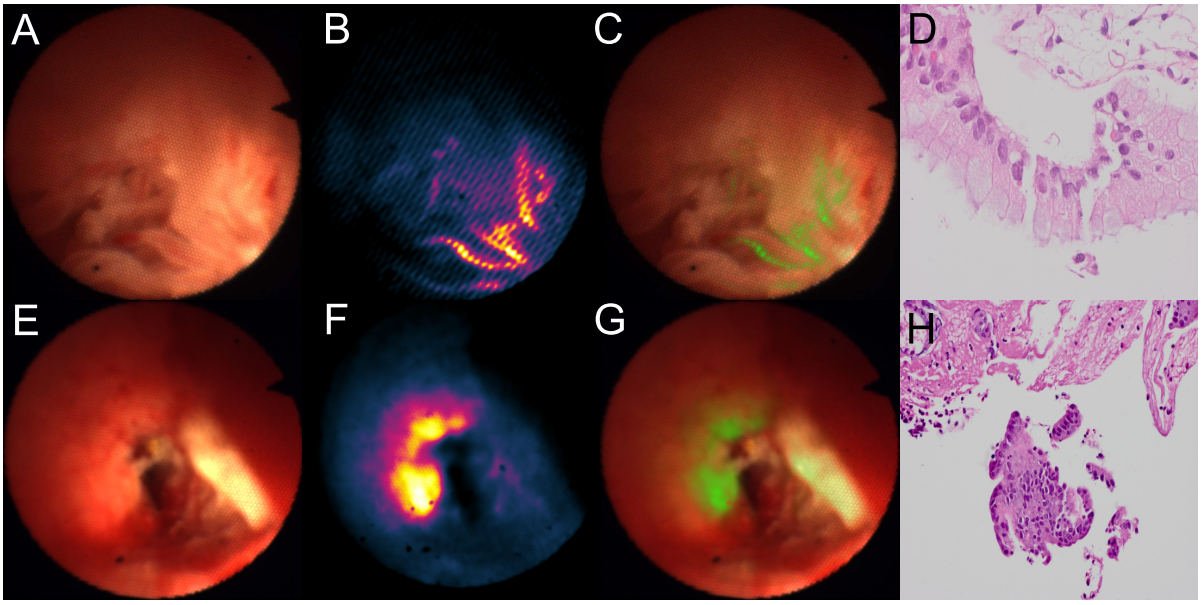

Figure 4.4: Intraoperative images acquired in the pancreatic duct (A–C) and the bile duct (E–G). Thereby A) and E) represent the color channel, B) and F) show the fluorescence signal of ICG and C) and G) are a composite overlay image. hematoxylin and eosin (H&E) staining of biopsies confirmed IPMN (D) and inflammation in the bile duct (H), respectively.

In patient two, cholangioscopy demonstrated distal biliary stenosis (2 cm). Direct inspection of the epithelium was not suspected for carcinoma and a benign fibrotic cause of stenosis was suspected. However, ICG fluorescence imaging demonstrated contrast enhancement in the stenotic area indicative for malignant lesions rather than scarred tissue. Cytological analysis revealed cells highly suspected for cholangiocarcinoma. Because of declining performances status, the patient decided for a conservative therapeutic approach. Biopsy samples displayed in Figure 4.4H) showed unspecific signs of inflammation. Malignant stenosis could not be obtained.

4.2.1.4 Discussion

The study showcased previously undocumented concurrent color and NIR fluorescence cholangiopancreatoscopy in patients. To examine the clinical imaging feasibility and perform system characterization in patients we employed the indocyanine green (ICG) fluorescent dye, which is well established for medical applications. ICG is not expected to offer specific cancer detection capacity as it only outlines areas of high vascularization and permeability and was utilized

herein to establish the feasibility of this pilot study. However areas of elevated fluorescence both in the pancreatic and bile duct were biopsied. Analysis of the biopsies confirmed the presence of malignancy in both fluorescent lesions visualized.
The system's capability to process fluorescence signals at video rates could enable adept capabilities during endoscopy, as it provides immediate feedback on suspicious lesions for biopsy guidance. With the use of agents with targeting specificity to cancer it is possible that increased accuracy and reproducibility in endoscopic procedures can be afforded, and operator variability minimized. A long list of tumor specific NIR fluorescent probes has been developed over the past years [75] that could offer enhanced visualization over the non-specific dye employed herein.
NIR fluorescence endoscopic imaging could be easily integrated in patient care suites, operating around conventional white light color endoscopy with a minimal impact on the normal clinical workflow given the real-time imaging capabilities and the ease of adaption to the endoscopy theater compared with radiological technologies. Conversely, the employment of a fiberscope compromises the resolution, as can be observed in the images displayed in Figure 4.4. These show the typical honeycomb effect that originates from the cladding around each fiber within the coherent imaging bundle. However, none of the available high quality videoscopes provide sufficient sensitivity for fluorescence imaging in the NIR range. An alternative approach would be the employment of a fiber optic imaging bundle that is long and thin enough to be guided through the accessory channel of a traditional videoscope. Thereby, physicians would still have the high-resolution images from the videoscope at their disposal for routine diagnostic means and utilize the fluorescence guidance as an aid in assessing the biologic importance of the lesion. Rigid relay lens scopes could be adopted in other endoscopic disciplines to attain improved image quality, but would also require a more invasive procedure. Altogether, we demonstrated that NIR fluorescence-guidance in cholangiopancreatoscopy enhances lesion visualization in the bile and pancreatic ducts and offers sensitivity that allows the detection of femptomole fluorophore amounts and video-rate fluorescence implementation.

4.2.2 Intra-operative breast cancer imaging

4.2.2.1 Rationale

Clinical studies have identified vascular endothelial growth factor (VEGF) and its role in angiogenesis as an important factor in the progression of breast cancer [76]. Importantly, increased

vascularization is already present in precursor and pre-invasive lesions [77]. This overexpression of VEGF in malignant and pre-malignant tissue makes it a promising molecular target in breast cancer, the more so as it is expressed by a reported 72–98 % of breast cancer patients [77, 78]. Furthermore, the identification of angiogenesis as a therapeutic target in general [79], and specifically the inhibition of its key mediator VEGF [80], have lead to the usage of anti-angiogenic drugs such as bevacizumab (Avastin®, Hoffmann-La Roche, Basel, Switzerland), a humanized monoclonal antibody, in breast cancer therapy. However the attained success, risk and precise indications remain controversial [81].
On the other hand, the high percentage of VEGF-positive patients and its sensitivity to malignant tissue make it an excellent marker for molecular imaging. Pre-clinical studies demonstrated that radio-labeled bevacizumab exhibits selective uptake in ovarian cancer [82] and renal cancer [83], enabling noninvasive molecular imaging with positron emission tomography (PET). However, the ionizing radiation and bulky instrumentation render PET imaging an inadequate method for intra-operative use. Instead, optical fluorescence labeling of bevacizumab and similar therapeutic drugs has been proposed to introduce new, highly tumor specific fluorescence agents into clinical practice with reduced translational risk [27]. In Section 4.1.2 bevacizumab was labeled with the NIR fluorescent IRDye 800CW-NHS (LI-COR Biosciences, Lincoln, US-NE) and imaged with the developed intra-operative system in a mouse model. Herein, the next step is taken by evaluating the feasibility of molecular imaging with bevacizumab-800CW during breast cancer surgery by utilizing the concept of microdosing [84], where less than 1 % of a drug's pharmacologically active amount is injected.

4.2.2.2 Methods

Materials The intra-operative imaging system as described in Section 2.1 was used to measure color and fluorescence images in real-time during the surgical intervention. Electrical safety was ensured by connecting the system's electronics to an isolation transformer to provide galvanic isolation. Since the camera arm and imaging system are used in the sterile field of the operating room (OR) they were covered in surgical drapes to prevent contamination.
The contrast agent bevacizumab-800CW was produced as previously described in Section 4.1.2 and in [30]. Three days before the surgery patients were injected intravenously with a microdose of 4.5 mg of bevacizumab-IRDye 800CW, equivalent to an amount of 30 nanomoles. Tumor resection was performed as a partial lumpectomy or mastectomy, depending on the

tumor size and infiltration. Intra-operatives images were taken of the tumor before surgical removal to provide surgical guidance and after the resection to assess margins and residual disease. Similarly, the sentinel lymph node and its cavity were imaged before and after removal. The excised lymph nodes and the sliced tumor specimen were also imaged immediately after the surgery.
Finally, some of the excised tissue was fixed in formalin and embedded in paraffin for histological analysis. Color and fluorescence images were taken of the sample blocks to verify ex vivo fluorescence emission. Microscopic slices were cut from the block to assess tumor presence and malignancy using hematoxylin and eosin (H&E) staining. The overexpression of VEGF on the slices was detected by staining with anti-VEGF (A-20) antibodies (sc-152, Santa Cruz Biotechnology, Dallas, US-TX).

Patients At the time of writing, nine patients (1 male, 8 female) were included in the study, ranging from 46 to 81 years of age. Inclusion criteria were a diagnosed invasive ductal carcinoma, validated by cytology or histology, that measured at least 6 mm in diameter, informed consent and a WHO performance score [85] of 0-2. Patients with other serious medical conditions, pregnancy and those that have previously received radiotherapy or chemotherapy were excluded from the study population. An overview of the patient characteristics and the performed interventions is listed in Table 4.1.

4.2.2.3 Results

Intra-operative imaging Fluorescence and color images were acquired during the surgical procedures for eight out of nine patients. The imaging steps did not interfere with the normal clinical workflow and only slightly extended the total surgery duration by no more than 20 minutes. No side effects or adverse reactions to the bavacizumab-800CW injection were observed in any patient. Representative images of the intra-operative tumor fluorescence are shown in Figure 4.5A–F. During the surgical intervention no direct imaging of cancerous tissue on the surface could be obtained, instead, as in the displayed samples, the tumor was typically located several millimeters to centimeters below the surface. Consequently, the measured signal, after having propagated through the tissue, appears strongly diffuse. By contrast, Fig. 4.5G–I shows the fluorescence signal obtained from two lymph nodes, both of which later

Patient number *[#]*	Sex	Age *[y]*	Surgery	Tumor diameter *[mm]*
1	m	67	Mastectomy	22
2	f	57	Mastectomy	23
3	f	46	Lumpectomy	25
4	f	81	Mastectomy	25
5	f	70	Mastectomy	28
6	f	71	Lumpectomy	19
7	f	64	Mastectomy	13
8	f	62	Lumpectomy	11
9	f	66	Lumpectomy	6

Table 4.1: Overview of patient data and performed surgeries in the breast cancer study, showing sex, age, the type of surgical intervention and the tumor size as measured by ultrasound imaging.

tested positive for metastases, that are more clearly delineated.

Ex vivo imaging Excised tissue was imaged ex vivo in the operating room to achieve a clearer, unobstructed view. Figure 4.6A–C shows a specimen removed during lumpectomy, that exhibits a strong fluorescence emission on the dorsoventral side, while Fig. 4.6G–I displays the fluorescence from an excised lymph node. The removed tumors were subsequently cut into approximately 3 mm thick slices for pathological evaluation and separate imaging (Fig. 4.6D–F), which allowed for the investigation of the entire tumor specimen, unobstructed by tissue diffusion.

Validation Figure 4.7A–C shows the color, fluorescence and overlay images of a paraffin embedded tumor sample. Therein, the tumor is located on the right side, while on the left side autofluorescence from skin can be seen. Standard histological staining with H&E confirmed the malignant nature of the tissue and corresponded well to the measured fluorescence (Fig. 4.7D), however it is important to distinguish between unspecific autofluorescence, e.g. from skin, and the molecular targeting by the bevacizumab-800CW agent. Staining for hematoxylin and VEGF is shown in Figs. 4.7E–F, which were taken at the two respective positions indicated in Fig. 4.7D. As expected, the overexpression of VEGF corresponds both to the tumor localization and fluorescence emission, showcasing the successful molecular targeting of breast cancer with

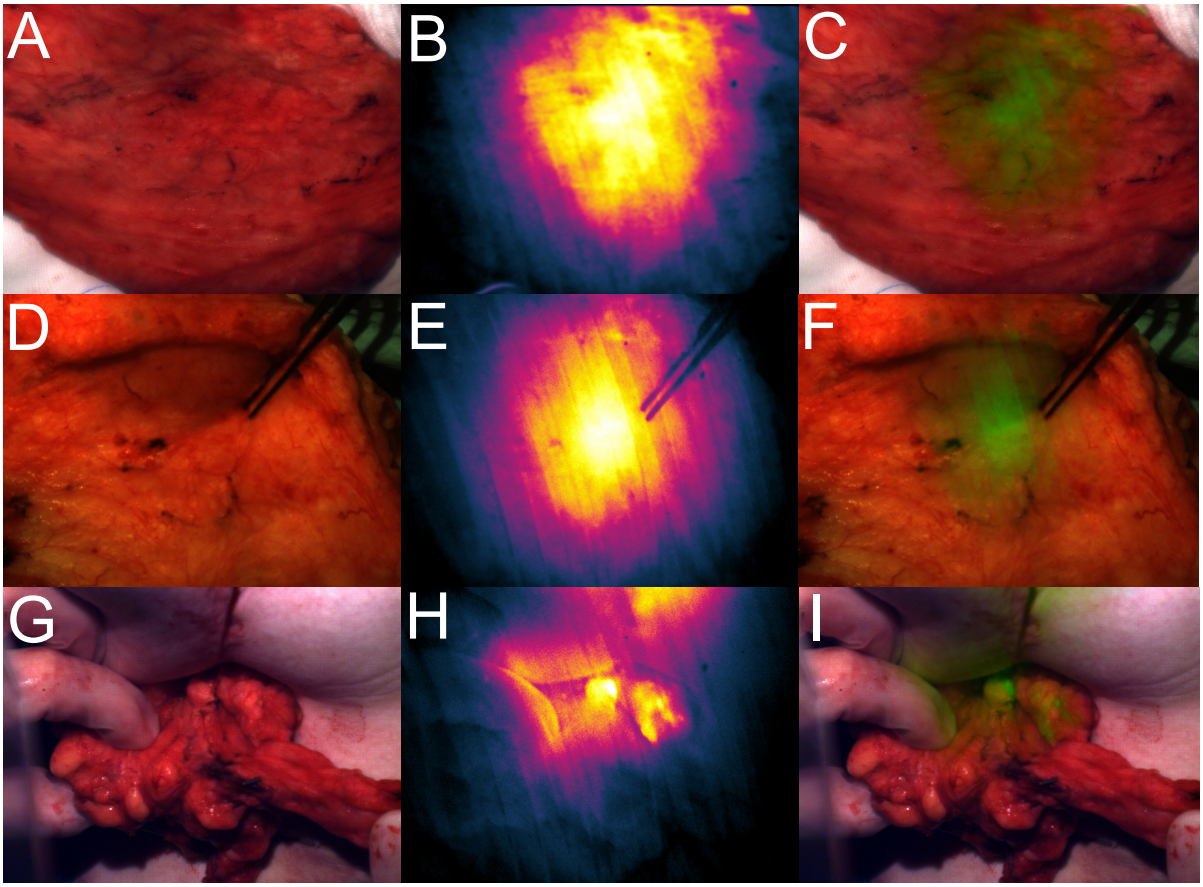

Figure 4.5: Intra-operative color, fluorescence and overlay images acquired with the imaging system during breast cancer surgery, utilizing the molecular bevacizumab-800CW agent. Intra-operative fluorescence from the tumor as seen during mastectomy (A–C) and lumpectomy (D–F). (G–I) Intra-operative fluorescence assessment of lymph nodes.

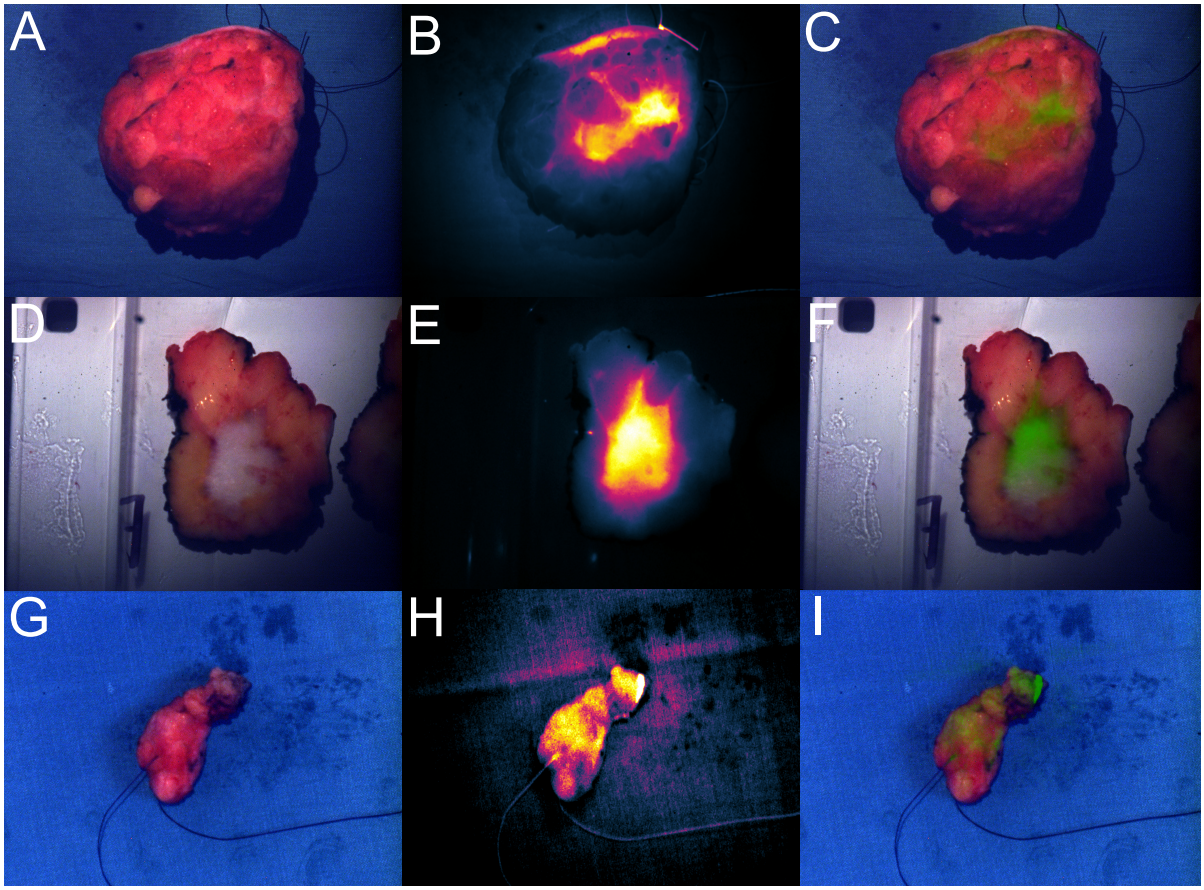

Figure 4.6: Ex vivo images, showing an excised tumor lump (A–C), a single 3 mm slice through the same lump (D–F) and an excised lymph node (G–I).

the conjugated antibody.

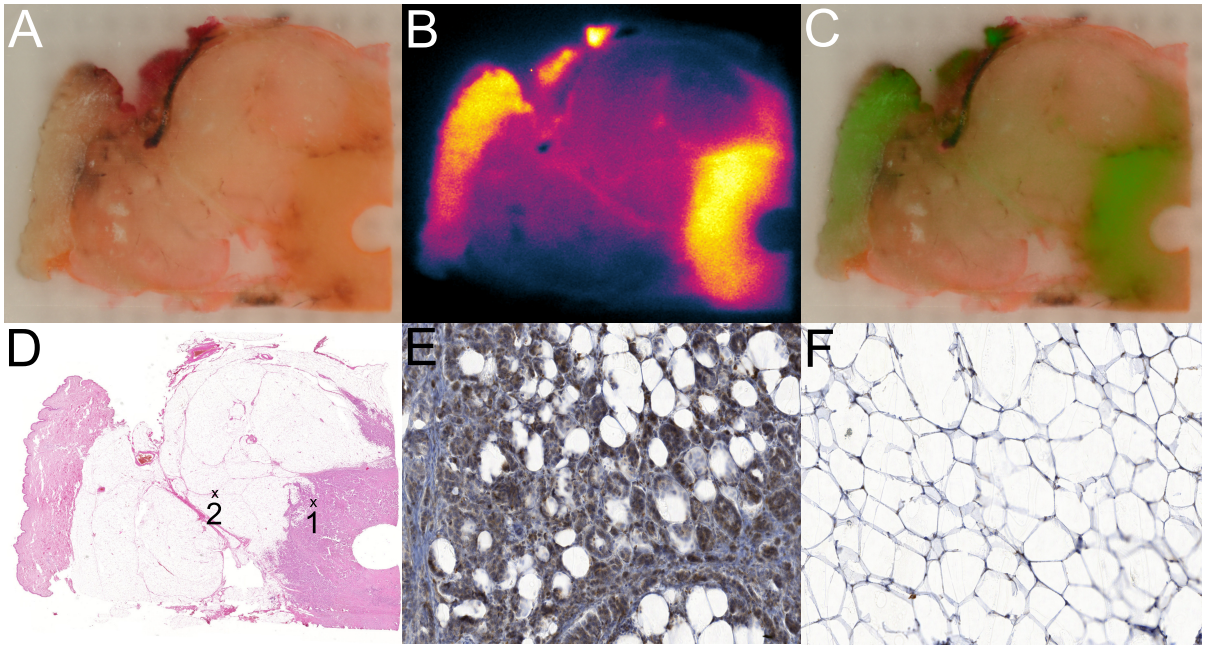

Figure 4.7: Validation of tumor targeting by bevacizumab-800CW, showing color, fluorescence and overlay images of a paraffin embedded tissue sample (A–C). D) Hematoxylin and eosin staining of the top slice. Staining for VEGF (brown, 20X) and hematoxylin revealed strong expression at position 1 (E) and virtually no presence at position 2 (F).

4.2.2.4 Discussion

It is important to note that the study is still ongoing, however some preliminary observations can be made at this point. The most important one concerns the proposed usage of therapeutic drugs as molecular imaging agents, where the available results confirm the feasibility of the proposed approach of conjugating a NIR dye and injecting the obtained agent in microdosing amounts. Histopathological analysis of excised tissue confirmed the selective accumulation of bevcizumab-800CW in areas of increased VEGF expression, which also coincided with malignancy. The marker seems to offer high sensitivity, as the main tumor location exhibited fluorescence in all patients during ex vivo slice imaging. However, the precise specificity still needs to be assessed, importantly it remains unclear whether VEGF overexpression is restricted to the tumor sites.

Due to the complex nature of the imaging process, a precise quantification of the method's

performance has to take the efficacy of several biochemical and physical processes into account. The first step in contrast formation is the expression of VEGF by malignant tumors, thus the specificity of this expression represents a first limiting factor for the approach. As numerous previous works addressed this issue it shall not be evaluated on the small number of samples in the current study. A second major step is the selective contrast agent accumulation in areas of elevated VEGF presence. Detailed microscopic analysis based on antibody staining as demonstrated in Figure 4.7 needs to be conducted for all patient samples to verify, that the distribution of bevcizumab-800CW corresponds to the presence of VEGF. Finally, the fluorescence image formation has to be validated, noting that sources other than the contrast agent might be detected in the fluorescence channel. Thereby, it is also important to discriminate the different acquisition environments, parameters and circumstances, most notably intra-operative and ex vivo data. Due to the more controlled conditions and reduced patient-to-patient variability the analysis of ex vivo samples represents the more promising path towards a preliminary assessment of the imaging sensitivity and specificity.

Regarding intra-operative imaging, some challenges were encountered. Signal intensity from tumors located several centimeters below the tissue surface turned out to be relatively low, with autofluorescence and crosstalk from unfiltered light sources in the operating room further degrading detection. Additionally, optical diffusion severely distorted the signal, hampering the envisioned surgical guidance application. The intra-operative evaluation of sentinel lymph node seems to represent an interesting possibility (Fig. 4.5G–I), however the expression of VEGF in lymphatic metastases needs to be investigated more closely, considering that in other patients no fluorescence was detected in positive nodes.

Intra-operative imaging of bevacizumab-800CW can potentially be employed to evaluate tumor margins, since fluorescence emission was also measured in tissue slices that contained smaller lesions distant from the main tumor mass. However, no case of positive margins was encountered in the patients so far, and thus it remains unclear whether small foci of residual disease can be imaged with reasonable sensitivity using microdosing amounts of the tracer.

Indeed, various issues could be ameliorated by increasing the contrast agent dose, thus amplifying the signal-to-background ratio with respect to parasitic signals and autofluorescence. With the current study showcasing the possibility of using drug-based agents for optical imaging it is envisioned that future applications using higher doses can pass the regulatory hurdles more easily. Other molecular targets, such as human epidermal growth factor receptor 2 (HER2), which is associated with a negative prognosis and expressed by over 20 % of patients

[86, 87], could also be targeted by appropriate antibodies.

4.2.3 Fluorescence colonoscopy

4.2.3.1 Rationale

Among all types of cancer, colorectal cancer (CRC) is the second most common cause of death [88, 89]. Regular colorectal screening via white light endoscopy is recommended for patients above the age of 50 to facilitate earlier detection and thus improve prognosis [90, 91]. However, especially small and flat adenomas are difficult to detect during colonoscopy due to the low tissue contrast, with reported lesion miss rates ranging from 20–26 % [37, 92, 93]. As discussed previously, fluorescence molecular imaging could significantly improve detection rates by providing a red-flag detection technique that can visualize tissue alterations which are imperceptible to the human eye over a large field of view [94]. The intra-operative imaging system developed in this work has been adapted for the use in laparoscopy (Section 2.2.2) and endoscopy (Section 2.2.4) and validated for clinical use with a NIR blood pool contrast agent in Section 4.2.1 [44].

The final crucial component thus is the identification of a suitable molecular cancer marker and a corresponding clinically applicable contrast agent. Angiogenesis, the formation of new blood vessels, plays an important role in the development and progression of CRC. As a main mediator of angiogenesis, vascular endothelial growth factor (VEGF) has been the subject of extensive research in diagnostic and therapeutic studies. Overexpression of VEGF has been found in colorectal cancer, and, importantly, seems to coincide with the progression from adenoma to cancer, enabling its exploitation for early stage lesions [95–98]. Similar to breast cancer, as discussed in the previous section, bevacizumab (Avastin®, Hoffmann-La Roche, Basel, Switzerland) has also, and indeed initially, been studied for the treatment of CRC by inhibiting angiogenesis, with studies reporting a prolonged survival time [28, 99] of patients who received anti-angiogenic treatment.

In Section 4.1.2 the therapeutic drug bevacizumab was conjugated to IRDye 800CW-NHS (LI-COR Biosciences, Lincoln, US-NE), yielding a molecular NIR fluorescent agent, and utilized successfully to target colorectal cancer in a mouse model, while Section 4.2.2 described the first in human usage of the bevacizumab-800CW agent in breast cancer patients. Herein, the same contrast mechanism, the overexpression of VEGF in cancerous tissue, is used to image CRC, employing a standard clinical fiberscope (GIF-XQ20, Olympus, Tokyo, Japan)

connected to the intra-operative system.

4.2.3.2 Methods

The gastroscope GIF-XQ20 was previously characterized for imaging in the NIR range in Section 2.2.1 and found suitable for clinical use, with an attenuation of 7.3 dB. The scope was connected to the imaging system as described in Section 2.2.4, facilitating concurrent color and NIR fluorescence image acquisition. An isolation transformer was used to ensure electrical safety.
The molecular contrast agent, a compound of bevacizumab and IRDye 800CW, was produced as described in Section 4.1.2 and [30]. A total of three patients with diagnosed CRC were imaged. The patients received an intravenous injection of the microdose amount of 4.5 mg three days before the intervention. Each patient was imaged twice, session 1 was performed before he or she received any treatment, while session 2 took place after the patient had received radiochemotherapy for three weeks.
Initially, during each session, videocolonoscopy is performed to assess the tumor using the clinical standard, followed by fluorescence endoscopy to locate areas of selective contrast agent accumulation. Finally, biopsies are taken, again under videocolonoscopy guidance, from the proximal end of the tumor, the tumor center and the distal point. For each biopsy sample the measured fluorescence level was recorded, normalizing the intensity by the unspecific autofluorescence levels of nearby healthy tissue.

4.2.3.3 Results

Representative images from the first imaging session of the three patients are shown in Figure 4.8. In the color images (Figs. 4.8A, D and G) the anatomical structures can be seen, while the tumor lesions can be recognized from their discoloration. However, improved specificity is afforded by the fluorescence channel (Figs. 4.8B, E and H), which exhibits selective contrast agent presence and thus NIR signal emission in the colorectal tumors.
Images of the corresponding sites acquired during session 2, i.e. after 3 weeks of radiochemotherapy, are shown in Figure 4.9. Tissue alterations as a result of the treatment can be recognized in the color images, most notably in Patient 1 (Figs. 4.8A–C), however the measured fluores-

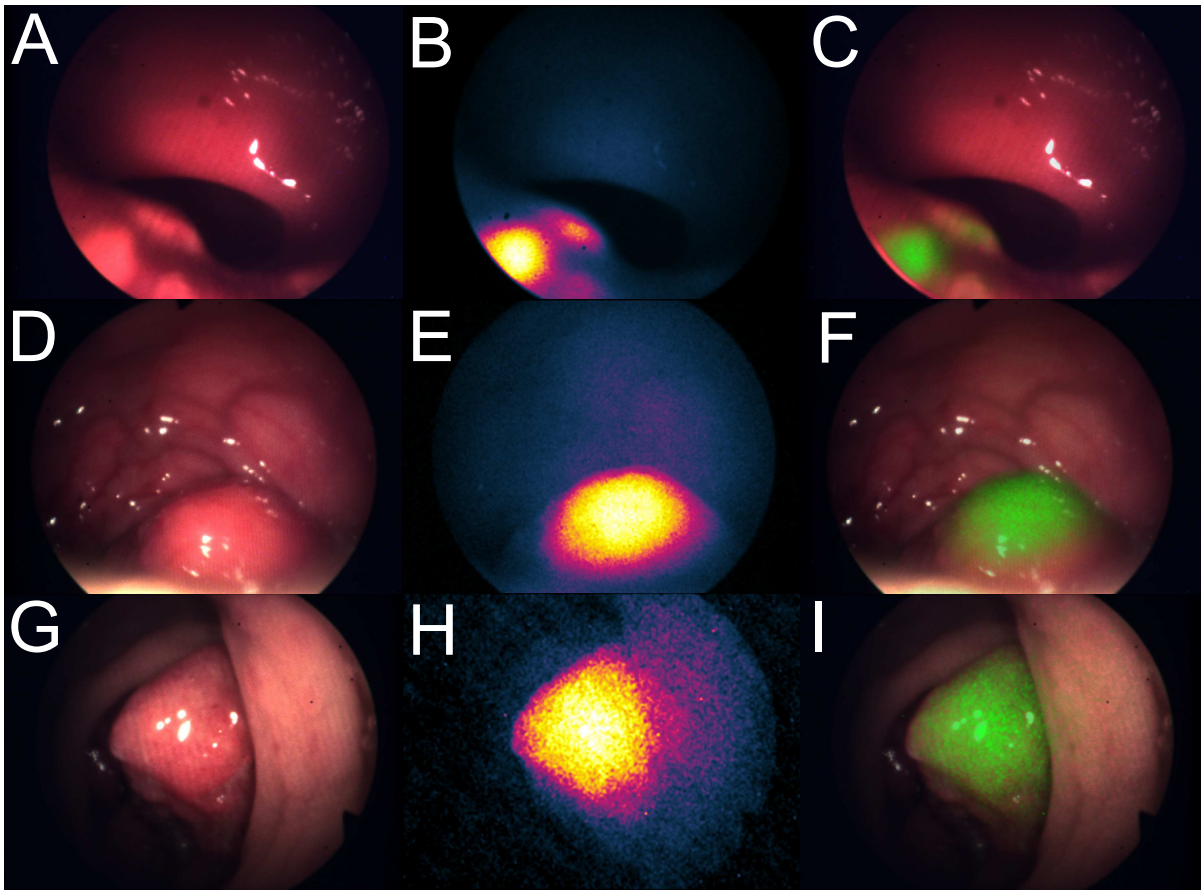

Figure 4.8: Color, fluorescence and overlay images acquired before treatment (session 1) from the first (A–C), second (D–F) and third (G–I) colorectal cancer patient.

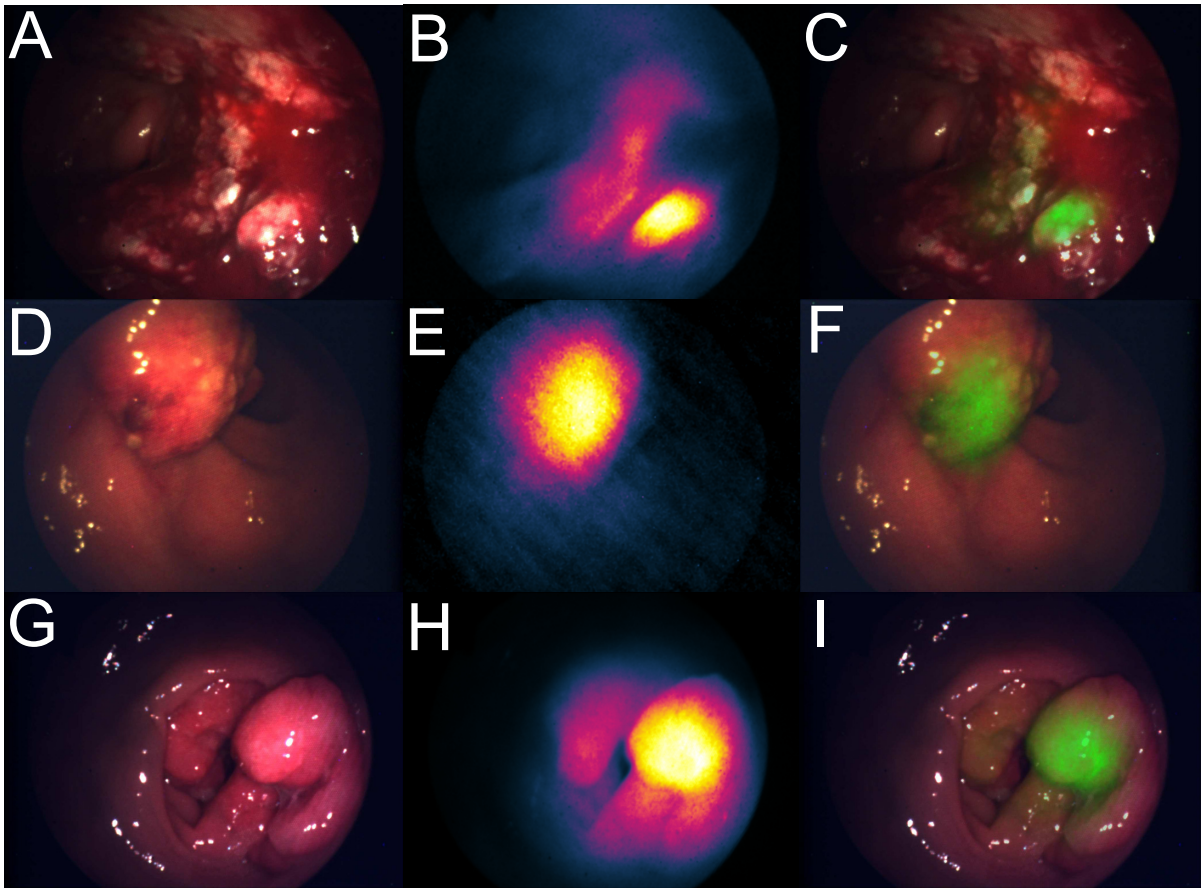

Figure 4.9: Color, fluorescence and overlay images acquired after treatment (session 2) from the first (A–C), second (D–F) and third (G–I) colorectal cancer patient.

cence intensity remained inconclusive. Due to heavy variations in acquisition geometry and parameters as well as the difficulty in identifying corresponding areas between the sessions the fluorescence emission before and after treatment could not easily be compared. Analyzing the ratio of tumor to background fluorescence counts, no clear decrease was seen after treatment. However, the analysis of the resected tissue biopsies is still outstanding at the time of writing. Indeed the evaluation of such samples represents a better opportunity to quantify contrast agent presence and VEGF expression before and after the treatment, as the measurement conditions are more controlled and standardized. Furthermore, final confirmation of the co-localization of NIR fluorescence and malignant CRC should also be obtained from the pathological sample analysis, however, fluorescence intensity corresponded well to the physician's visual assessment during videocolonoscopy.

4.2.3.4 Discussion

Molecularly targeted NIR fluorescence colonoscopy was realized for the first time in human patients. This was achieved by employing a modification of the developed real-time imaging system, wherein a fiberscope is used the deliver the illumination and acquire color and fluorescence images concurrently. The monoclonal antibody bevacizumab, conjugated to a NIR dye, was employed as a molecular contrast agent, as previously realized in mouse models (Sec. 4.1.2) and breast cancer patients (Sec. 4.2.2).
Even though the pathological analysis of the excised tissue was not completed at the time of writing, it has to be noted that the available information indicates successful targeting of colorectal cancer by bevacizumab-800CW, given that the detected fluorescence accurately corresponded to the physician's evaluation of the lesions from videocolonoscopy. This opens the exciting possibility of a red-flag detection strategy, based on molecular agents and surveillance fluorescence colonoscopy, which has the potential to improve lesion detection rates significantly. It is important to characterize the contrast agent's sensitivity and specificity in further studies. While the current results show great promise, a high clinical impact requires a statistically significant decrease in lesion miss rates to be demonstrated on a broader patient population. Additionally, the suitability of alternative molecular targets, e.g. human epidermal growth factor receptor 2 (HER2) should be investigated. Considering that cancer is a distinctively heterogeneous disease, a personalized approach to its molecular targeting might be called for.

Concerning the system adaptation to endoscopy, an alternative setup was proposed in Section 2.2.4, namely one where a fiber bundle is coupled to the cameras and guided through the working channel of a clinical endoscope. While the usage of a fiberscope offers the advantage of an available working channel, it suffers from the downside of a significantly decreased color image quality. Consequently, in the present study, the physicians preferred to take biopsies under standard videocolonoscopy guidance. Major sources for the decreased color image quality are the fiber claddings and the inefficient light coupling. On the other side, the fiberscope setup was characterized to yield an increased fluorescence sensitivity, thus allowing for the detection of smaller contrast agent doses. Notably, fluorescence imaging was feasible in real-time, setting acquisition times of 100 ms and below, thus providing immediate feedback and intuitive orientation. Future work should explore the alternative imaging setup using a fiber bundle, as a "minimally invasive translation" approach, that impacts standard clinical procedures as little as possible, while complementing them with molecular fluorescence information.

Bibliography

[1] J. Glatz, J. Varga, P. B. Garcia-Allende, M. Koch, F. R. Greten, and V. Ntziachristos, "Concurrent video-rate color and near-infrared fluorescence laparoscopy", *Journal of Biomedical Optics*, vol. 18, no. 10, p. 101 302, 2013.

[2] R. Siegel, E. Ward, O. Brawley, and A. Jemal, "Cancer statistics, 2011", *CA: A Cancer Journal for Clinicians*, vol. 61, no. 4, pp. 212–236, 2011.

[3] F. Bray, J.-S. Ren, E. Masuyer, and J. Ferlay, "Global estimates of cancer prevalence for 27 sites in the adult population in 2008", *International Journal of Cancer*, 2012.

[4] J. Ferlay, H.-R. Shin, F. Bray, D. Forman, C. Mathers, and D. M. Parkin, "Estimates of worldwide burden of cancer in 2008: GLOBOCAN 2008", *International Journal of Cancer*, vol. 127, no. 12, pp. 2893–2917, 2010.

[5] N. S. Abraham, J. M. Young, and M. J. Solomon, "Meta-analysis of short-term outcomes after laparoscopic resection for colorectal cancer", *British Journal of Surgery*, vol. 91, no. 9, pp. 1111–1124, 2004.

[6] E. Kuhry, W. Schwenk, R. Gaupset, U. Romild, and H. Bonjer, "Long-term results of laparoscopic colorectal cancer resection", *Cochrane Database Syst Rev*, vol. 2, 2008.

[7] D. Rex, C. Cutler, G. Lemmel, E. Rahmani, D. Clark, D. Helper, G. Lehman, and D. Mark, "Colonoscopic miss rates of adenomas determined by back-to-back colonoscopies", *Gastroenterology*, vol. 112, no. 1, pp. 24–28, 1997.

[8] H. Machida, Y. Sano, Y. Hamamoto, M. Muto, T. Kozu, H. Tajiri, S. Yoshida, *et al.*, "Narrow-band imaging in the diagnosis of colorectal mucosal lesions: a pilot study.", *Endoscopy*, vol. 36, no. 12, p. 1094, 2004.

[9] A. Adler, H. Pohl, I. S. Papanikolaou, H. Abou-Rebyeh, G. Schachschal, W. Veltzke-Schlieker, A. C. Khalifa, E. Setka, M. Koch, B. Wiedenmann, and T. Rösch, "A prospective randomised study on narrow-band imaging versus conventional colonoscopy for adenoma detection: does narrow-band imaging induce a learning effect?", *Gut*, vol. 57, no. 1, pp. 59–64, 2008.

[10] K. Inoue, N. Wakabayashi, Y. Morimoto, K. Miyawaki, A. Kashiwa, N. Yoshida, K. Nakano, H. Takada, Y. Harada, N. Yagi, Y. Naito, T. Takamatsu, and T. Yoshikawa, "Evaluation of autofluorescence colonoscopy for diagnosis of superficial colorectal neoplastic lesions", *International Journal of Colorectal Disease*, vol. 25, pp. 811–816, 7 2010.

[11] A. McCallum, J. Jenkins, D. Gillen, and R. Molloy, "Evaluation of autofluorescence colonoscopy for the detection and diagnosis of colonic polyps", *Gastrointestinal endoscopy*, vol. 68, no. 2, pp. 283–290, 2008.

[12] D. De Veld, M. Witjes, H. Sterenborg, and J. Roodenburg, "The status of in vivo autofluorescence spectroscopy and imaging for oral oncology", *Oral oncology*, vol. 41, no. 2, pp. 117–131, 2005.

[13] L. Yannuzzi, J. Slakter, J. Sorenson, D. Guyer, and D. Orlock, "Digital indocyanine green videoangiography and choroidal neovascularization", *Retina*, vol. 12, no. 3, pp. 191–223, 1992.

[14] R. Y. Tsien, "Building and breeding molecules to spy on cells and tumors", *FEBS Letters*, vol. 579, no. 4, pp. 927–932, 2005.

[15] R. Weissleder and M. Pittet, "Imaging in the era of molecular oncology", *Nature*, vol. 452, no. 7187, pp. 580–589, 2008.

[16] P. Pasricha and M. Motamedi, "Optical biopsies,"bioendoscopy", and why the sky is blue: the coming revolution in gastrointestinal imaging", *Gastroenterology*, vol. 122, no. 2, pp. 571–575, 2002.

[17] G. M. van Dam, G. Themelis, L. M. A. Crane, N. J. Harlaar, R. G. Pleijhuis, W. Kelder, A. Sarantopoulos, J. S. de Jong, H. J. G. Arts, A. G. J. van der Zee, B. Joost, P. S. Low, and V. Ntziachristos, "Intraoperative tumor-specific fluorescence imaging in ovarian cancer by folate receptor-α targeting: first in-human results", *Nature Medicine*, vol. 17, no. 10, pp. 1315–1319, 2011.

[18] A. Pegg, "Methylation of the o6 position of guanine in dna is the most likely initiating event in carcinogenesis by methylating agents", *Cancer investigation*, vol. 2, no. 3, pp. 223–231, 1984.

[19] M. Takahashi, S. Nakatsugi, T. Sugimura, and K. Wakabayashi, "Frequent mutations of the β-catenin gene in mouse colon tumors induced by azoxymethane", *Carcinogenesis*, vol. 21, no. 6, pp. 1117–1120, 2000.

[20] F. Greten, L. Eckmann, T. Greten, J. Park, Z. Li, L. Egan, M. Kagnoff, and M. Karin, "IKKβ links inflammation and tumorigenesis in a mouse model of colitis-associated cancer", *Cell*, vol. 118, no. 3, pp. 285–296, 2004.

[21] K. Guda, M. Upender, G. Belinsky, C. Flynn, M. Nakanishi, J. Marino, T. Ried, and D. Rosenberg, "Carcinogen-induced colon tumors in mice are chromosomally stable and are characterized by low-level microsatellite instability", *Oncogene*, vol. 23, no. 21, pp. 3813–3821, 2004.

[22] S. Wirtz, C. Neufert, B. Weigmann, and M. Neurath, "Chemically induced mouse models of intestinal inflammation", *Nature protocols*, vol. 2, no. 3, pp. 541–546, 2007.

[23] M. Ernst and R. G. Ramsay, "Colorectal cancer mouse models: integrating inflammation and the stroma", *Journal of Gastroenterology and Hepatology*, vol. 27, no. 1, pp. 39–50, 2012.

[24] M. L. Clapper, H. S. Cooper, and W.-C. L. Chang, "Dextran sulfate sodium-induced colitis-associated neoplasia: a promising model for the development of chemopreventive interventions", *Acta Pharmacologica Sinica*, vol. 28, no. 9, pp. 1450–1459, 2007.

[25] J. Desgrosellier and D. Cheresh, "Integrins in cancer: biological implications and therapeutic opportunities", *Nature Reviews Cancer*, vol. 10, no. 1, pp. 9–22, 2010.

[26] P. B. Garcia-Allende, J. Glatz, M. Koch, J. J. Tjalma, E. Hartmans, A. G. Terwisscha van Scheltinga, P. Symvoulidis, G. M. van Dam, W. B. Nagengast, and V. Ntziachristos, "Towards clinically translatable nir fluorescence molecular guidance for colonoscopy", *Biomedical Optics Express*, vol. 5, no. 1, pp. 78–92, 2014.

[27] W. Scheuer, G. van Dam, M. Dobosz, M. Schwaiger, and V. Ntziachristos, "Drug-based optical agents: infiltrating clinics at lower risk", *Science Translational Medicine*, vol. 4, no. 134, 134ps11–134ps11, 2012.

[28] H. Hurwitz, L. Fehrenbacher, W. Novotny, T. Cartwright, J. Hainsworth, W. Heim, J. Berlin, A. Baron, S. Griffing, E. Holmgren, *et al.*, "Bevacizumab plus irinotecan, fluorouracil, and leucovorin for metastatic colorectal cancer", *New England journal of medicine*, vol. 350, no. 23, pp. 2335–2342, 2004.

[29] M. V. Marshall, D. Draney, E. M. Sevick-Muraca, and D. M. Olive, "Single-dose intravenous toxicity study of IRDye 800CW in Sprague-Dawley rats", *Molecular Imaging and Biology*, vol. 12, no. 6, pp. 583–594, 2010.

[30] A. G. T. van Scheltinga, G. M. van Dam, W. B. Nagengast, V. Ntziachristos, H. Hollema, J. L. Herek, C. P. Schröder, J. G. Kosterink, M. N. Lub-de Hoog, and E. G. de Vries, "Intraoperative near-infrared fluorescence tumor imaging with vascular endothelial growth factor and human epidermal growth factor receptor 2 targeting antibodies", *Journal of Nuclear Medicine*, vol. 52, no. 11, pp. 1778–1785, 2011.

[31] D. Rex, D. Johnson, J. Anderson, P. Schoenfeld, C. Burke, and J. Inadomi, "American college of gastroenterology guidelines for colorectal cancer screening 2008", *The American journal of gastroenterology*, vol. 104, no. 3, pp. 739–750, 2009.

[32] R. W. Burt, "Colorectal cancer screening", *Current Opinion in Gastroenterology*, vol. 25, no. 5, pp. 466–470, 2010.

[33] A. Sonnenberg, F. Delcò, and J. M. Inadomi, "Cost-effectiveness of colonoscopy in screening for colorectal cancer.", *Annals of Internal Medicine*, vol. 133, no. 8, pp. 573–584, 2000.

[34] D. A. Lieberman, D. G. Weiss, J. H. Bond, D. J. Ahnen, H. Garewal, W. V. Harford, D. Provenzale, S. Sontag, T. Schnell, T. E. Durbin, D. B. Nelson, S. L. Ewing, G. Triadafilopoulos, F. C. Ramirez, J. G. Lee, J. F. Collins, M. B. Fennerty, T. K. Johnston, C. L. Corless, K. R. McQuaid, R. E. Sampliner, T. G. Morales, R. Fass, R. Smith, Y. Maheshwari, and G. Chejfec, "Use of colonoscopy to screen asymptomatic adults for colorectal cancer", *New England Journal of Medicine*, vol. 343, no. 3, pp. 162–168, 2000.

[35] D. F. Ransohoff, "How much does colonoscopy reduce colon cancer mortality?", *Annals of internal medicine*, vol. 150, no. 1, pp. 50–52, 2009.

[36] E. Thiis-Evensen, G. S. Hoff, J. Sauar, F. Langmark, B. M. Majak, and M. H. Vatn, "Population-based surveillance by colonoscopy: effect on the incidence of colorectal cancer: Telemark Polyp Study I", *Scandinavian journal of gastroenterology*, vol. 34, no. 4, pp. 414–420, 1999.

[37] J. C. van Rijn, J. B. Reitsma, J. Stoker, P. M. Bossuyt, S. J. van Deventer, and E. Dekker, "Polyp miss rate determined by tandem colonoscopy: a systematic review", *The American journal of gastroenterology*, vol. 101, no. 2, pp. 343–350, 2006.

[38] R. S. Bradley and M. S. Thorniley, "A review of attenuation correction techniques for tissue fluorescence", *Journal of the Royal Society Interface*, vol. 3, no. 6, pp. 1–13, 2006.

[39] P. A. Valdés, F. Leblond, V. L. Jacobs, B. C. Wilson, K. D. Paulsen, and D. W. Roberts, "Quantitative, spectrally-resolved intraoperative fluorescence imaging", *Scientific reports*, vol. 2, 2012.

[40] E. J. Blok, P. J. Kuppen, J. E. van Leeuwen, and C. F. Sier, "Cytoplasmic overexpression of her2: a key factor in colorectal cancer", *Clinical Medicine Insights. Oncology*, vol. 7, p. 41, 2013.

[41] M. Goetz, M. Hoetker, M. Diken, P. Galle, and R. Kiesslich, "In vivo molecular imaging with cetuximab, an anti-egfr antibody, for prediction of response in xenograft models of human colorectal cancer", *Endoscopy*, no. EFirst, 2013.

[42] A. J. McEwan, H. F. Van Brocklin, and C. Divgi, "Action plan for emerging molecular imaging technologies", *Journal of Nuclear Medicine*, vol. 49, no. 2, 37N–40N, 2008.

[43] P. B. Garcia-Allende, J. Glatz, M. Koch, and V. Ntziachristos, "Enriching the interventional vision of cancer with fluorescence and optoacoustic imaging", *Journal of Nuclear Medicine*, vol. 54, no. 5, pp. 664–667, 2013.

[44] J. Glatz, P. B. Garcia-Allende, V. Becker, M. Koch, A. Meining, and V. Ntziachristos, "Near-infrared fluorescence cholangiopancreatoscopy: initial clinical feasibility results", *Gastrointestinal Endoscopy*, vol. 79, pp. 664–668, 2014.

[45] M. Hidalgo, "Pancreatic cancer", *New England Journal of Medicine*, vol. 362, no. 17, pp. 1605–1617, 2010.

[46] P. C. de Groen, G. J. Gores, N. F. LaRusso, L. L. Gunderson, and D. M. Nagorney, "Biliary tract cancers", *New England Journal of Medicine*, vol. 341, no. 18, pp. 1368–1378, 1999.

[47] D. G. Adler, T. H. Baron, R. E. Davila, J. Egan, W. K. Hirota, J. A. Leighton, W. Qureshi, E. Rajan, M. J. Zuckerman, R. Fanelli, *et al.*, "ASGE guideline: the role of ERCP in diseases of the biliary tract and the pancreas", *Gastrointestinal Endoscopy*, vol. 62, no. 1, pp. 1–8, 2005.

[48] M. de Bellis, S. Sherman, E. L. Fogel, H. Cramer, J. Chappo, L. McHenry Jr, J. L. Watkins, and G. A. Lehman, "Tissue sampling at ercp in suspected malignant biliary strictures (part 2)", *Gastrointestinal Endoscopy*, vol. 56, no. 5, pp. 720–730, 2002.

[49] J. M. Cha, M.-H. Kim, and S. J. Jang, "Early bile duct cancer", *World Journal of Gastroenterology*, vol. 13, no. 25, p. 3409, 2007.

[50] R. J. Shah, D. A. Langer, M. R. Antillon, and Y. K. Chen, "Cholangioscopy and cholangioscopic forceps biopsy in patients with indeterminate pancreaticobiliary pathology", *Clinical Gastroenterology and Hepatology*, vol. 4, no. 2, pp. 219–225, 2006.

[51] Y. Fukuda, T. Tsuyuguchi, Y. Sakai, S. Tsuchiya, and H. Saisyo, "Diagnostic utility of peroral cholangioscopy for various bile-duct lesions", *Gastrointestinal Endoscopy*, vol. 62, no. 3, pp. 374–382, 2005.

[52] M. McIver, "An instrument for visualizing the interior of the common duct at operation", *Surgery*, vol. 9, pp. 112–4, 1941.

[53] J. Tischendorf, M. Krüger, C. Trautwein, N. Duckstein, A. Schneider, M. Manns, and P. Meier, "Cholangioscopic characterization of dominant bile duct stenoses in patients with primary sclerosing cholangitis", *Endoscopy*, vol. 38, no. 07, pp. 665–669, 2006.

[54] T. Kaneko, A. Nakao, S. Nomoto, T. Furukawa, Y. Hirooka, N. Nakashima, and T. Nagasaka, "Intraoperative pancreatoscopy with the ultrathin pancreatoscope for mucin-producing tumors of the pancreas", *Archives of Surgery*, vol. 133, no. 3, p. 263, 1998.

[55] D. Uhlmann, M. Wiedmann, F. Schmidt, R. Kluge, A. Tannapfel, F. Berr, J. Hauss, and H. Witzigmann, "Management and outcome in patients with klatskin-mimicking lesions of the biliary tree", *Journal of Gastrointestinal Surgery*, vol. 10, no. 8, pp. 1144–1150, 2006.

[56] M. B. Wallace and R. Kiesslich, "Advances in endoscopic imaging of colorectal neoplasia", *Gastroenterology*, vol. 138, no. 6, pp. 2140–2150, 2010.

[57] L. M. Wong Kee Song, D. G. Adler, B. Chand, J. D. Conway, J. Croffie, J. A. DiSario, D. S. Mishkin, R. J. Shah, L. Somogyi, W. M. Tierney, *et al.*, "Chromoendoscopy", *Gastrointestinal Endoscopy*, vol. 66, no. 4, pp. 639–649, 2007.

[58] A. Hoffman, R. Kiesslich, F. Bittinger, P. Galle, and M. Neurath, "Methylene blue-aided cholangioscopy in patients with biliary strictures: feasibility and outcome analysis", *Endoscopy*, vol. 40, no. 7, pp. 563–571, 2008.

[59] L. M. Wong Kee Song, D. G. Adler, J. D. Conway, D. L. Diehl, F. A. Farraye, S. V. Kantsevoy, R. Kwon, P. Mamula, B. Rodriguez, R. J. Shah, *et al.*, "Narrow band imaging and multiband imaging", *Gastrointestinal Endoscopy*, vol. 67, no. 4, pp. 581–589, 2008.

[60] A. Itoh, Y. Hirooka, H. Kawashima, Y. Niwa, and H. Goto, "Endoscopic approach to the pancreatobiliary tract using narrow band imaging", *Digestive Endoscopy*, vol. 19, no. s1, S115–S120, 2007.

[61] L. M. Wong Kee Song, S. Banerjee, D. Desilets, D. L. Diehl, F. A. Farraye, V. Kaul, S. R. Kethu, R. S. Kwon, P. Mamula, M. C. Pedrosa, *et al.*, "Autofluorescence imaging", *Gastrointestinal Endoscopy*, vol. 73, no. 4, pp. 647–650, 2011.

[62] K. Izuishi, H. Tajiri, M. Ryu, J. Furuse, Y. Maru, K. Inoue, M. Konishi, and T. Kinoshita, "Detection of bile duct cancer by autofluorescence cholangioscopy: a pilot study.", *Hepato-gastroenterology*, vol. 46, no. 26, p. 804, 1999.

[63] T. Itoi, Y. Shinohara, K. Takeda, K. Nakamura, and K. Takei, "Improvement of choledochoscopy: chromoendocholedochoscopy, autofluorescence imaging, or narrow-band imaging", *Digestive Endoscopy*, vol. 19, no. s1, S95–S104, 2007.

[64] W. Curvers, L. Baak, R. Kiesslich, A. Van Oijen, T. Rabenstein, K. Ragunath, J.-F. Rey, P. Scholten, U. Seitz, F. Ten Kate, *et al.*, "Chromoendoscopy and narrow-band imaging compared with high-resolution magnification endoscopy in barrett's esophagus", *Gastroenterology*, vol. 134, no. 3, pp. 670–679, 2008.

[65] J. P. Nass and S. E. Connolly, "Current status of chromoendoscopy and narrow band imaging in colonoscopy", *Clinics in Colon and Rectal Surgery*, vol. 23, no. 1, p. 21, 2010.

[66] M. C. Pierce, D. J. Javier, and R. Richards-Kortum, "Optical contrast agents and imaging systems for detection and diagnosis of cancer", *International Journal of Cancer*, vol. 123, no. 9, pp. 1979–1990, 2008.

[67] T. Aoki, D. Yasuda, Y. Shimizu, M. Odaira, T. Niiya, T. Kusano, K. Mitamura, K. Hayashi, N. Murai, T. Koizumi, *et al.*, "Image-guided liver mapping using fluorescence navigation system with indocyanine green for anatomical hepatic resection", *World Journal of Surgery*, vol. 32, no. 8, pp. 1763–1767, 2008.

[68] L. M. A. Crane, G. Themelis, R. G. Pleijhuis, N. J. Harlaar, A. Sarantopoulos, H. J. G. Arts, A. G. J. van der Zee, V. Ntziachristos, and G. M. van Dam, "Intraoperative multispectral fluorescence imaging for the detection of the sentinel lymph node in cervical cancer: a novel concept", *Molecular Imaging and Biology*, vol. 13, no. 5, pp. 1043–1049, 2011.

[69] L. M. A. Crane, G. Themelis, H. J. G. Arts, K. T. Buddingh, A. H. Brouwers, V. Ntziachristos, G. M. van Dam, and A. G. J. van der Zee, "Intraoperative near-infrared fluorescence imaging for sentinel lymph node detection in vulvar cancer: first clinical results", *Gynecologic Oncology*, vol. 120, no. 2, pp. 291–295, 2011.

[70] R. S. Kwon, D. G. Adler, B. Chand, J. D. Conway, D. L. Diehl, S. V. Kantsevoy, P. Mamula, S. A. Rodriguez, R. J. Shah, L. M. Wong Kee Song, *et al.*, "High-resolution and high-magnification endoscopes", *Gastrointestinal Endoscopy*, vol. 69, no. 3, pp. 399–407, 2009.

[71] R. J. Shah, D. G. Adler, J. D. Conway, D. L. Diehl, F. A. Farraye, S. V. Kantsevoy, R. Kwon, P. Mamula, S. Rodriguez, L. M. Wong Kee Song, *et al.*, "Cholangiopancreatoscopy", *Gastrointestinal Endoscopy*, vol. 68, no. 3, pp. 411–421, 2008.

[72] T. Aoki, M. Murakami, D. Yasuda, Y. Shimizu, T. Kusano, K. Matsuda, T. Niiya, H. Kato, N. Murai, K. Otsuka, *et al.*, "Intraoperative fluorescent imaging using indocyanine green for liver mapping and cholangiography", *Journal of hepato-biliary-pancreatic Sciences*, vol. 17, no. 5, pp. 590–594, 2010.

[73] R. Upadhyay, R. A. Sheth, R. Weissleder, and U. Mahmood, "Quantitative real-time catheter-based fluorescence molecular imaging in mice", *Radiology*, vol. 245, no. 2, pp. 523–531, 2007.

[74] S. Mordon, J. M. Devoisselle, S. Soulie-Begu, and T. Desmettre, "Indocyanine green: physicochemical factors affecting its fluorescence in vivo", *Microvascular Research*, vol. 55, no. 2, pp. 146–152, 1998.

[75] S. A. Hilderbrand and R. Weissleder, "Near-infrared fluorescence: application to *in vivo* molecular imaging", *Current Opinion in Chemical Biology*, vol. 14, no. 1, pp. 71–79, 2010.

[76] G. W. Sledge Jr, "VEGF-targeting therapy for breast cancer", *Journal of mammary gland biology and neoplasia*, vol. 10, no. 4, pp. 319–323, 2005.

[77] P. Viacava, A. G. Naccarato, G. Bocci, G. Fanelli, P. Aretini, A. Lonobile, G. Evangelista, G. Montruccoli, and G. Bevilacqua, "Angiogenesis and VEGF expression in pre-invasive lesions of the human breast", *The Journal of pathology*, vol. 204, no. 2, pp. 140–146, 2004.

[78] I. Kostopoulos, P. Arapantoni-Dadioti, H. Gogas, S. Papadopoulos, V. Malamou-Mitsi, C. D. Scopa, S. Markaki, E. Karagianni, V. Kyriakou, A. Margariti, *et al.*, "Evaluation of the prognostic value of HER-2 and VEGF in breast cancer patients participating in a randomized study with dose–dense sequential adjuvant chemotherapy", *Breast cancer research and treatment*, vol. 96, no. 3, pp. 251–261, 2006.

[79] N. Ferrara and R. S. Kerbel, "Angiogenesis as a therapeutic target", *Nature*, vol. 438, no. 7070, pp. 967–974, 2005.

[80] B. P. Schneider and G. W. Sledge, "Drug insight: VEGF as a therapeutic target for breast cancer", *Nature Clinical Practice Oncology*, vol. 4, no. 3, pp. 181–189, 2007.

[81] A. J. Montero, M. Escobar, G. Lopes, S. Glück, and C. Vogel, "Bevacizumab in the treatment of metastatic breast cancer: friend or foe?", *Current oncology reports*, vol. 14, no. 1, pp. 1–11, 2012.

[82] W. B. Nagengast, E. G. de Vries, G. A. Hospers, N. H. Mulder, J. R. de Jong, H. Hollema, A. H. Brouwers, G. A. van Dongen, L. R. Perk, and M. N. Lub-de Hooge, "In vivo vegf imaging with radiolabeled bevacizumab in a human ovarian tumor xenograft", *Journal of Nuclear Medicine*, vol. 48, no. 8, pp. 1313–1319, 2007.

[83] I. M. Desar, A. B. Stillebroer, E. Oosterwijk, W. P. Leenders, C. M. van Herpen, W. T. van der Graaf, O. C. Boerman, P. F. Mulders, and W. J. Oyen, "111in-bevacizumab imaging of renal cell cancer and evaluation of neoadjuvant treatment with the vascular endothelial growth factor receptor inhibitor sorafenib", *Journal of Nuclear Medicine*, vol. 51, no. 11, pp. 1707–1715, 2010.

[84] U.S. Department of Health and Human Services, Center for Drug Evaluation and Research, "Guidance for industry, investigators, and reviewers. exploratory ind studies", United States Food and Drug Administration, Washington DC, 2006.

[85] M. M. Oken, R. H. Creech, D. C. Tormey, J. Horton, T. E. Davis, E. T. McFadden, and P. P. Carbone, "Toxicity and response criteria of the eastern cooperative oncology group", *American journal of clinical oncology*, vol. 5, no. 6, pp. 649–656, 1982.

[86] D. J. Slamon, G. M. Clark, S. G. Wong, W. J. Levin, A. Ullrich, and W. L. McGuire, "Human breast cancer: correlation of relapse and survival with amplification of the HER-2/neu oncogene", *Science*, vol. 235, no. 4785, pp. 177–182, 1987.

[87] H. J. Burstein, "The distinctive nature of HER2-positive breast cancers", *New England Journal of Medicine*, vol. 353, no. 16, pp. 1652–1654, 2005.

[88] International Agency for Research on Cancer, *GLOBOCAN 2012: estimated cancer incidence, mortality and prevalence worldwide in 2012*, 2012.

[89] R. Siegel, J. Ma, Z. Zou, and A. Jemal, "Cancer statistics 2014", *CA: A Cancer Journal for Clinicians*, vol. 64, no. 1, pp. 9–29, 2014.

[90] S. Winawer, R. Fletcher, D. Rex, J. Bond, R. Burt, J. Ferrucci, T. Ganiats, T. Levin, S. Woolf, D. Johnson, *et al.*, "Colorectal cancer screening and surveillance: clinical guidelines and rationale - update based on new evidence", *Gastroenterology*, vol. 124, no. 2, pp. 544–560, 2003.

[91] D. Rockey, E. Paulson, D. e. Niedzwiecki, W. Davis, H. Bosworth, L. Sanders, J. Yee, J. Henderson, P. Hatten, S. Burdick, *et al.*, "Analysis of air contrast barium enema, computed tomographic colonography, and colonoscopy: prospective comparison", *The Lancet*, vol. 365, no. 9456, pp. 305–311, 2005.

[92] E. M. Stoffel, D. K. Turgeon, D. H. Stockwell, L. Zhao, D. P. Normolle, M. K. Tuck, R. S. Bresalier, N. E. Marcon, J. A. Baron, M. T. Ruffin, *et al.*, "Missed adenomas during colonoscopic surveillance in individuals with lynch syndrome (hereditary non-polyposis colorectal cancer)", *Cancer Prevention Research*, vol. 1, no. 6, pp. 470–475, 2008.

[93] D. Heresbach, T. Barrioz, M. Lapalus, D. Coumaros, P. Bauret, P. Potier, D. Sautereau, C. Boustière, J. Grimaud, C. Barthélémy, *et al.*, "Miss rate for colorectal neoplastic polyps: a prospective multicenter study of back-to-back video colonoscopies.", *Endoscopy*, vol. 40, no. 4, pp. 284–290, 2008.

[94] M. S. Hoetker and M. Goetz, "Molecular imaging in endoscopy", *United European Gastroenterology Journal*, vol. 1, no. 2, pp. 84–92, 2013.

[95] C. A. Staton, A. S. Chetwood, I. C. Cameron, S. S. Cross, N. J. Brown, and M. W. Reed, "The angiogenic switch occurs at the adenoma stage of the adenoma–carcinoma sequence in colorectal cancer", *Gut*, vol. 56, no. 10, pp. 1426–1432, 2007.

[96] M. Raica, A. M. Cimpean, and D. Ribatti, "Angiogenesis in pre-malignant conditions", *European Journal of Cancer*, vol. 45, no. 11, pp. 1924–1934, 2009.

[97] V. Hanrahan, M. J. Currie, S. P. Gunningham, H. R. Morrin, P. A. Scott, B. A. Robinson, and S. B. Fox, "The angiogenic switch for vascular endothelial growth factor (VEGF)-A, VEGF-B, VEGF-C, and VEGF-D in the adenoma–carcinoma sequence during colorectal cancer progression", *The Journal of pathology*, vol. 200, no. 2, pp. 183–194, 2003.

[98] M. L. George, M. G. Tutton, F. Janssen, A. Arnaoutz, A. M. Abulafi, S. A. Eccles, and R. I. Swift, "VEGF-A, VEGF-C, and VEGF-D in colorectal cancer progression", *Neoplasia*, vol. 3, no. 5, p. 420, 2001.

[99] B. J. Giantonio, P. J. Catalano, N. J. Meropol, P. J. O'Dwyer, E. P. Mitchell, S. R. Alberts, M. A. Schwartz, and A. B. Benson, "Bevacizumab in combination with oxaliplatin, fluorouracil, and leucovorin (FOLFOX4) for previously treated metastatic colorectal cancer: results from the Eastern Cooperative Oncology Group Study E3200", *Journal of Clinical Oncology*, vol. 25, no. 12, pp. 1539–1544, 2007.

Chapter 5

Conclusion and outlook

5.1 Conclusion

The three major objectives of this work were the construction of an intra-operative imaging system for the use in surgery and endoscopy, the development of appropriate image processing algorithms for the representation, analysis and enhancement of fluorescence images and the translation of molecularly targeted near-infrared (NIR) fluorescence imaging into clinical studies.

The intra-operative imaging setup was presented in Chapter 2 and its sensitivity and optical resolution were characterized both for the lens-based setup and the adaptations to endoscopy and laparoscopy. High sensitivity in the NIR spectral range was attained by using a cooled EMCCD sensor, enabling the detection of very low dye amounts, which were expected in the translational microdosing studies. The detection sensitivity decreased slightly in the endoscopic setup as a result of the inefficient laser coupling into the scope's light port and due to attenuation of the fibers, as measured in Section 2.2.1.

Handling of the system turned out to be very easy during clinical interventions. Since the cameras are mounted on a surgical arm, which also carries the necessary hardware components, the system can quickly be moved in and out of the sterile field during surgery, without impeding the physician's work. Most parameter control and processing functions were automated in the custom developed software, thus image acquisition could be performed in a minimal amount of time, increasing the surgery duration by only a few minutes. Importantly, real-time processing on the graphics processing unit (GPU) offered immediate feedback at

video frame rates, a significant factor for surgical guidance applications. Experiences during endoscopic use of the system turned out to be equally positive, with more relaxed workflow and sterility requirements easing setup and preparation, while utilized flexible scopes provided enough maneuvering possibilities for the physician, despite the mechanical coupling to the setup.

A powerful framework for intra-operative image processing has been created by the custom developed software. Profiling of the current processing pipeline indicated, that more computationally expensive steps can be realized using the GPU as a co-processor as described in Section 3.1. An important development that might utilize further processing power is quantitative fluorescence imaging, which requires the correction of various degrading effects on a fluorescence image to retrieve the true fluorophore concentration at a tissue location.

One of the major challenges for quantitative imaging, the interaction of light with the tissue sample through which it propagates, was discussed in Section 3.2. Therein, crucial improvements upon previous approaches to the correction of the influence of optical properties on the signal were introduced. Previously, algorithms that operate on a pixel-by-pixel basis have been proposed, predominantly for the correction of inhomogeneous absorption in tissue [1, 2]. However, the influence of light scattering has been hardly addressed in planar fluorescence imaging, and indeed is of a more complex nature. The key aspect is the two-dimensional nature of scattering, namely the fact that a scatterer at a certain location not only influences the measured intensity at that very point but in its entire vicinity. A novel approach based on space-variant deconvolution was proposed, wherein scattering was modeled by a gaussian-shaped fluorescence point spread function (FPSF) and corrected by iterative deconvolution. The results showed that diffusion effects could be corrected in phantoms and mouse data by estimating the FPSF from multispectral reflection measurements. However, some remaining issues prevented the implementation in the intra-operative setup for application in patient measurements. Firstly, the proposed iterative deconvolution scheme is computationally expensive and not easily parallelized on the GPU, consequently making video-rate performance unattainable at the moment. Secondly, the FPSF estimation from reflectance measurements is suboptimal and only observation-based. Ideally, the reduced scattering coefficient would be used, however light propagation models indicate that it cannot be determined from planar reflectance images [3, 4]. Instead, spatial frequency domain imaging (SFDI) was shown capable of resolving absorption and scattering coefficients [5], and consequently could be integrated in a next-generation intra-operative system to determine the scattering coefficient as an input

for the proposed correction method.
Another possible system upgrade results from the wavelength optimization presented in Section 3.3. Based on a theoretical diffuse reflectance model [3], an optimization of the three spectral measurement points was conducted to yield the wavelengths that are most suitable to reconstruct the wavelenght-independent optical properties of tissue, which comprise physiologically important parameters like the blood oxygenation. Such optimized wavelengths could replace the current color acquisition, wherein three broad spectra are used to closely reproduce human color perception, in favor of obtaining quantitative measurements of tissue parameters. The optimization was verified on liquid phantom data, showing that the computed wavelengths indeed yielded highly accurate results in retrieving the optical properties. Future work should validate the calculation on in vivo animal data in order to ensure the validity of the made assumptions and confirm the possibility to translate wavelength-optimized reflection imaging to clinical applications.
Chapter 4 presented the experimental results, where initially two pre-clinical studies were conducted in Section 4.1 to validate the developed materials and methods under relevant imaging conditions. In Section 4.1.1 the laparoscopic system adaptation developed in Section 2.2.2 was used to image induced colorectal cancer (CRC) in mice using a commercial pre-clinical molecular agent. The results confirmed the system's adequacy and expected sensitivity, indicating that molecular targeting of CRC could help to increase clinical detection rates. On the other hand, handling the laparoscope turned out to be difficlt, as both the scope and the camera head are rigid and consequently make panning shots and even small adjustments difficult. A possible solution would be the integration of a coherent imaging fiber bundle connecting the laparoscope to the camera system, however this would come at the expense of decreased image quality and sensitivity.
The molecular agent bevacizumab-800CW, a compound of a monoclonal antibody and a NIR fluorescent dye, was evaluated for CRC detection in Section 4.1.2. Two designs suitable for clinical endoscopy were developed in Section 2.2.4, namely a fiberscope and a miniature fiber probe. Both were evaluated on mouse models of human CRC, showcasing that intra-operative fluorescence imaging can visualize molecular targets, in this case vascular endothelial growth factor (VEGF), during endoscopic screening. The results showed a clear delineation of cancerous tissue, encouraging clinical translation of both the agent and the imaging setup.
The clinical work was presented in Section 4.2, where first a feasibility study in endoscopic gastrointestinal imaging was performed in Section 4.2.1. Two patients with malignancies in

the bile duct and pancreatic duct, respectively, were injected with indocyanine green (ICG) and imaged using a fiber cholangioscope connected to the intra-operative system. The fluorescent dye's distribution could be monitored in real time, enabling enhanced diagnosis through its accumulation in areas of increased vascular permeability. While the results showed that fluorescence imaging holds promise to improve endoscopic diagnosis, further patients were not measured in order to concentrate on targeted contrast agents.

Using the drug-based agent bevacizumab-800CW in microdosing concentrations, clinical translation of intra-operative molecular imaging for breast cancer surgery was undertaken in Section 4.2.2. Intra-operative images were acquired before and after the tumor resection to assess leftover margins. Furthermore, ex vivo tissue imaging as well as histopathological validation was conducted to verify the findings. Considering that the study is still ongoing, only preliminary results are available, which currently appear mixed. On the bright side, validation confirms the selective agent uptake in tumor tissue, thus demonstrating, for the first time, a successful clinical application of a drug-based agent in microdoses. Ex vivo imaging of both tissue slices and paraffin-embedded samples exhibit a high correlation with histology and VEGF staining. Surgical imaging, however, turned out to be challenging. Due to the fact that the tumor is typically covered by several centimeters of tissue, especially when a complete mastectomy is performed, the images are heavily affected by diffusion and the limitations of light penetration. The available data suggests, that imaging tumors located deep inside the breast with extremely low contrast agent doses is not suitable for surgical guidance. The identification of positive margins, which would be on the surface after resection, remains as a possible application, however no such margins were encountered and thus it remains unclear whether their signal intensity would surpass the autofluorescence and crosstalk level.

Finally, fluorescence colonoscopy was realized in Section 4.2.3 by injecting CRC patients with bevacizumab-800CW and imaging through a clinical fiberscope connected to the system. At the time of writing three patients were imaged before and after they received radiochemotherapy. While the results regarding treatment monitoring remain inconclusive due to the limited number of patients and current lack of histological validation, some notable observations were made nonetheless. Given that the cancer lesions are typically located on the colon wall surface, the images were significantly less affected by diffusion and light absorption that in the breast cancer scenario, resulting in a clearer delineation and higher signal-to-background ratio. It appears that a red-flag detection strategy, that identifies cancerous alterations in wide-field endoscopy is feasible even with microdosing agent concentrations. However, ex

vivo biopsy analysis still needs to confirm the correspondence of fluorescence intensity to tissue malignancy.

5.2 Outlook

In this work the clinical translation of intra-operative NIR fluorescence imaging with molecular specificity was realized, however several more steps are necessary to shift the paradigm in surgical imaging.

The technological development of intra-operative imaging systems is ongoing [6]. Possible improvements are the incorporation of image correction schemes such as the one presented in Section 3.2 or simpler ratiometric methods [2, 7] to facilitate quantitative fluorescence measurements which are unaffected by variances in the tissue optical properties. The autofluorescence contribution can be unmixed from multispectral images [8] or mitigated using a contiguous waveband measurement [9]. Apart from multiple spectral images in reflection geometry, the usage of additional hardware represents a more promising path to a new generation of imaging systems. Tissue properties can be measured by SFDI using structured illumination [10] or by fiber optic spectroscopy [11]. Other developments might improve the system handling, e.g. the use of wearable goggles [12] to display the images directly to the surgeon or pulsed excitation that can measure under standard operation room light conditions [13]. On the other hand, a downside of different systems with different technological capabilities is the lack of standardization and comparability. Consequently, standard measurements for parameters like resolution and sensitivity need to be introduced, comparing the performance under realistic conditions that include autofluorescence, depth dependence and optical property variations.

The translational concept of microdosing was successfully applied herein to demonstrate feasibility, safety and efficacy of drug-based agents while bypassing regulatory hurdles. Higher doses should be explored in future studies in order to significantly improve the attained tumor-to-background ratio. Importantly, the novel imaging methods should be assessed quantitatively on larger patient populations in phase II and III trials to demonstrate the improved cancer visualization capability that is promised by the current results. Finally, targeted drug molecules other than bevacizumab should be investigated, potentially leading to a more diverse portfolio of contrast agents that are optimally suited for different types of cancer, or even selected individually for each patient as part of a personalized treatment approach.

Molecular optical imaging will significantly impact current clinical practice and improve diagnosis and treatment that was previously based on anatomical imaging, often performed with the bare eye. Herein the possible benefits in two medical fields have been outlined, namely cancer resection surgery and surveillance endoscopy. Obviously many more applications are thinkable, the principle of supplementing optical imaging with molecular information is a universal one. With more fluorescent agents being explored, either over the course of microdosing studies or along the traditional translation path, clinical demand from both patients and physicians is expected to grow.

Bibliography

[1] G. Themelis, J. Yoo, K. Soh, R. Schulz, and V. Ntziachristos, "Real-time intraoperative fluorescence imaging system using light-absorption correction", *Journal of Biomedical Optics*, vol. 14, no. 6, p. 064 012, 2009.

[2] P. A. Valdés, F. Leblond, A. Kim, B. T. Harris, B. C. Wilson, X. Fan, T. D. Tosteson, A. Hartov, S. Ji, K. Erkmen, *et al.*, "Quantitative fluorescence in intracranial tumor: implications for ala-induced ppix as an intraoperative biomarker", *Journal of Neurosurgery*, vol. 115, no. 1, p. 11, 2011.

[3] T. J. Farrell, M. S. Patterson, and B. Wilson, "A diffusion theory model of spatially resolved, steady-state diffuse reflectance for the noninvasive determination of tissue optical properties invivo", *Medical Physics*, vol. 19, no. 4, pp. 879–888, 1992.

[4] P. Symvoulidis, K. M. Jentoft, P. B. Garcia-Allende, J. Glatz, J. Ripoll, and V. Ntziachristos, "Steady-state total diffuse reflectance with an exponential decaying source", *Optics Letters*, vol. 39, no. 13, pp. 3919–3922, 2014.

[5] D. J. Cuccia, F. Bevilacqua, A. J. Durkin, F. R. Ayers, and B. J. Tromberg, "Quantitation and mapping of tissue optical properties using modulated imaging", *Journal of Biomedical Optics*, vol. 14, no. 2, p. 024 012, 2009.

[6] Q. T. Nguyen and R. Y. Tsien, "Fluorescence-guided surgery with live molecular navigation - a new cutting edge", *Nature Reviews Cancer*, 2013.

[7] R. S. Bradley and M. S. Thorniley, "A review of attenuation correction techniques for tissue fluorescence", *Journal of the Royal Society Interface*, vol. 3, no. 6, pp. 1–13, 2006.

[8] J. R. Mansfield, K. W. Gossage, C. C. Hoyt, and R. M. Levenson, "Autofluorescence removal, multiplexing, and automated analysis methods for in-vivo fluorescence imaging", *Journal of Biomedical Optics*, vol. 10, no. 4, p. 041 207, 2005.

[9] C. Yang, V. W. Hou, E. J. Girard, L. Y. Nelson, and E. J. Seibel, "Target-to-background enhancement in multispectral endoscopy with background autofluorescence mitigation for quantitative molecular imaging", *Journal of Biomedical Optics*, vol. 19, no. 7, p. 076 014, 2014.

[10] J. T. Nguyen, S. J. Lin, A. M. Tobias, S. Gioux, A. Mazhar, D. J. Cuccia, Y. Ashitate, A. Stockdale, R. Oketokoun, N. J. Durr, *et al.*, "A novel pilot study using spatial frequency domain imaging to assess oxygenation of perforator flaps during reconstructive breast surgery", *Annals of Plastic Surgery*, vol. 71, no. 3, pp. 308–315, 2013.

[11] U. A. Gamm, "Quantification of tissue scattering properties by use of fiber optic spectroscopy", PhD Thesis, Erasmus MC: University Medical Center Rotterdam, 2013.

[12] Y. Liu, A. Q. Bauer, W. J. Akers, G. Sudlow, K. Liang, D. Shen, M. Y. Berezin, J. P. Culver, and S. Achilefu, "Hands-free, wireless goggles for near-infrared fluorescence and real-time image-guided surgery", *Surgery*, vol. 149, no. 5, pp. 689–698, 2011.

[13] K. Sexton, S. C. Davis, D. McClatchy, P. A. Valdes, S. C. Kanick, K. D. Paulsen, D. W. Roberts, and B. W. Pogue, "Pulsed-light imaging for fluorescence guided surgery under normal room lighting", *Optics Letters*, vol. 38, no. 17, pp. 3249–3252, 2013.

List of tables

List of figures

List of abbreviations

5–ALA 5-aminolevulinic acid

AFI autofluorescence imaging

AOM Azoxymethane

API application programming interface

CCD charge-coupled device

CFA color filter array

CPU central processing unit

CRC colorectal cancer

CT computed tomography

CTF contrast transfer function

CUDA compute unified device architecture

CW continuous wave

DMA direct memory access

DRAM dynamic random access memory

DSS Dextran Sulfate Sodium

ECC error-correcting code

EMCCD electron multiplying charge-coupled device

ERCP endoscopic retrograde cholangiopancreatography

FDA United States food and drug administration

FITC fluorescein isothiocyanate

FLOPS floating point operations per second

FOV field of view

fps frames per second

FPSF fluorescence point spread function

FWHM full width at half maximum

GFP green fluorescent protein

GPGPU general purpose computation on graphics processing unit

GPU graphics processing unit

GUI graphical user interface

H&E hematoxylin and eosin

HER2 human epidermal growth factor receptor 2

I/O input/output

ICG indocyanine green

IHC immunohistochemistry

IPMN intraductal papillary mucinous neoplasm

MFP mean free path

MRI magnetic resonance imaging

NA numerical aperture

NBI narrow band imaging

NIR near-infrared

NPP Nvidia performance primitives

OR operating room

PBS phosphate buffered saline

PCA principal component analysis

PCI peripheral component interconnect

PET positron emission tomography

PPIX protoporphyrin IX

PSF point spread function

RMSN root-mean-square noise

ROI region of interest

SFDI spatial frequency domain imaging

SNR signal-to-noise ratio

SPECT single-photon emission computed tomography

SSD solid-state-drive

TBR tumor-to-background ratio

TiO_2 titanium oxide

VEGF vascular endothelial growth factor

VEGF-A vascular endothelial growth factor A

List of publications

2014 P. Symvoulidis, K. M. Jentoft, P. B. Garcia-Allende, **J. Glatz**, J. Ripoll and V. Ntziachristos, "Steady-state total diffuse reflectance with an exponential decaying source", *Optics Letters*, vol. 39, no. 13, pp. 3919–3922, 2014. doi: 10.1364/OL.39.003919

J. Glatz, P. Symvoulidis, P. B. Garcia-Allende and V. Ntziachristos, "Robust overlay schemes for the fusion of fluorescence and color channels in biological imaging", *Journal of Biomedical Optics Letters*, vol. 19, no. 4, p. 040501, 2014. doi: 10.1117/1.JBO.19.4.040501

M. Koch, **J. Glatz**, V. Ermolayev, E. G. de Vries, G. M. van Dam, K.-H. Englmeier and V. Ntziachristos, "Video-rate optical flow corrected intraoperative functional fluorescence imaging", *Journal of Biomedical Optics*, vol. 19, no. 4, p. 046012, 2014. doi: 10.1117/1.JBO.19.4.046012

P. B. Garcia-Allende, **J. Glatz**, M. Koch, J. J. Tjalma, E. Hartmans, A. G. Terwisscha van Scheltinga, P. Symvoulidis, G. M. van Dam, W. B. Nagengast, and V. Ntziachristos, "Towards clinically translatable NIR fluorescence molecular guidance for colonoscopy", *Biomedical Optics Express*, vol. 5, no. 1, pp. 78–92, 2014. doi: 10.1364/BOE.5.000078

J. Glatz, P. B. Garcia-Allende, V. Becker, M. Koch, A. Meining, and V. Ntziachristos, "Near-infrared fluorescence cholangiopancreatoscopy: initial clinical feasibility results", *Gastrointestinal Endoscopy*, vol. 79, no. 4, pp. 664–668, 2014. doi: 10.1016/j.gie.2013.10.008.

2013 P. B. Garcia-Allende, **J. Glatz**, M. Koch, and V. Ntziachristos, "Enriching the interventional vision of cancer with fluorescence and optoacoustic imaging", *Journal of Nuclear Medicine*, vol. 54, no. 5, pp. 664–667, 2013. doi: 10.2967/jnumed.111.099796

J. Glatz and V. Ntziachristos, "Intraoperative Molekulare Fluoreszenzbildgebung", *Ärzteblatt Sachsen*, vol. 24, no. 5, pp. 201–202, 2013.

J. Glatz, J. Varga, P. B. Garcia-Allende, M. Koch, F. R. Greten, and V. Ntziachristos, "Concurrent video-rate color and near-infrared fluorescence laparoscopy", *Journal of Biomedical Optics*, vol. 18, no. 10, p. 101302, 2013. doi: 10.1117/1.JBO.18.10.101302

2012 V. Ntziachristos and **J. Glatz**, "Shifting the paradigm in surgical vision with fluorescence molecular imaging", *SPIE Newsroom*, 2012. doi: 10.1117/2.120121.004003

2011 **J. Glatz**, N. C. Deliolanis, A. Buehler, D. Razansky, and V. Ntziachristos, "Blind source unmixing in multi-spectral optoacoustic tomography", *Optics Express*, vol. 19, no. 4, pp. 3175–3184, 2011. doi: 10.1364/OE.19.003175

Acknowledgements

The work presented in this thesis was only possible due to the support that I received from several people, whom I would like to thank herein.
First and foremost, I want to thank Prof. Vasilis Ntziachristos who gave me the chance to join his lab and supervised this work. I am very grateful for all the knowledge he shared with me, the guidance he provided and the time he took to discuss any questions that I had.
I am also much obliged to my colleagues at the molecular fluorescence imaging lab. Maximilian Koch, Beatriz Garcia-Allende and Panagiotis Symvoulidis not only helped me with countless discussions about various projects, but more importantly they made the institute a great place to work at. You guys prove the saying about people being the greatest asset.
Many thanks go to Nikolaos Deliolanis, who supervised my master's thesis, taught me many things about science and made it so much fun that I decided to stay for a PhD. I also owe a lot to George Themelis and Athanasios Sarantopoulos, who helped me along the first steps in optical imaging and did a lot of the previous work that this thesis builds on.
I also want to thank the other researchers at IBMI, notably Karin Radrich, Vladimir Ermolayev and Karin Jentoft, with whom I had the pleasure of working, as well as the technical and administrative staff that kept things ticking over.
Many of my projects would not have been possible without the help of external collaborators. I wish to thank Valentin Becker and Alexander Meining from Klinikum rechts der Isar in Munich for their help with the cholangiopancreatoscopy study. Furthermore, I want to thank the colleagues from Universitair Medisch Centrum Groningen (UMCG) who helped to realize the studies conducted there. Specifically, these are Esther de Boer, Titia Lamberts and Gooitzen van Dam, who supervised the medical proceedings of the breast cancer study, while Jolien Tjalma, Elmire Hartmans and Wouter Nagengast, managed the colonoscopy study.
Finally, I want to thank my family and friends, who might come last in this section but first in life.